Chapter 5

Experimental Results - Dynamics

5.1 Overview

The dynamics of the mean flow fields described in Chapter 4 will be presented in this chapter using mainly two tools: the power spectral density of velocity fluctuations and the time history of velocity fluctuations. For some cases extended measurements are performed to illustrate the evolution of large scale periodic structures. These measurements involve acoustic measurements, that can be used to assess some of the global characteristics of instability that cannot be identified using local one point measurements. Time histories of velocities are used to help in the determination of the dynamics because the power spectral density representation sometimes doesn't capture significant dynamic flow features.

Both the frequency and power density axes of the presented PSD's are normalized. The power spectral density values are normalized by the local RMS velocity unless otherwise remarked. The power spectral density is also scaled by the inverse of the scaling for the x-axis so that the spectral density is with respect to the non-dimensional frequency scale. The frequency axis is normalized by the ratio of the characteristic scale and the area mean velocity in the nozzle. The frequency axis thus should be read as the Strouhal number. Since the original unit for the frequency axis was Hz, the Strouhal number is a non-dimensional cyclic frequency and not a non-dimensional circular frequency. As will be seen in Chapter 6, the natural Strouhal number used in linear stability analysis is a non-dimensional circular frequency and care must be taken in comparing the results.

Power spectra will be plotted on log-log scales to facilitate the appreciation of the entire spectrum. In some cases, certain features are better explored using a linear scale. For log-log plots, the -5/3 slope expected in the center of turbulent time scales will be indicated on the graph. The range of time scales associated with the -5/3 slope is called the inertial subrange. The inertial subrange is a range of time–scales or length–scales of turbulence that is not associated with turbulence production. Instead, this range represents the channel of energy transfer from the energy containing large scales to the dissipative small scales. The degree to which a linear range can

be identified in the log-log plotted spectra is an important marker for the state of the turbulence at the point under consideration. The inertial subrange is not always resolved at the higher flow rate of 100 SCFM because the sampling frequencies of the LDV didn't allow collection at high enough frequencies.

Section 5.2 summarizes the dynamics of the main test matrix cases described in Chapter 4. Section 5.3 presents additional measurements for selected, especially dynamically interesting experimental conditions. Finally, Section 5.4 presents acoustic measurements which will discuss the relationship between the measured pressure and the dynamic state of the flow field.

5.2 Overview of flow dynamics

5.2.1 Free vortex geometry

5.2.1.1 Nozzle flow dynamics

The time history for all data points presented in Chapter 4 is available in the raw LDV data files. Hence it would be possible to show a power spectrum for each data point. Such a presentation would be extremely repetitive. Power spectra were indeed calculated at every data point. The subset shown here summarizes overall behavior and highlights interesting aspects of the spectra.

Figure 5.1 shows the spectra of axial and swirl velocity at r/D_n=0.07, near the core of the flow for all three swirl conditions at x/D_n=-0.35, 50 SCFM. Both axial and swirl velocity profiles exhibit a significant linear region with a slope approximately equal to -5/3. Consequently the smaller scales of turbulence are still isotropic even though, as seen in Chapter 4, the turbulence in general is not isotropic, especially in the center of the flow. Figure 5.1 does show significant differences between the axial and swirl velocity spectrum. The swirl velocity spectrum has a broader linear range than the axial velocity when swirl is non-zero.

The integral time scale of the flow field is proportional to the apparent zero intercept of the y-axis (Pope, 2001). Figure 5.1 shows that the integral time scales for

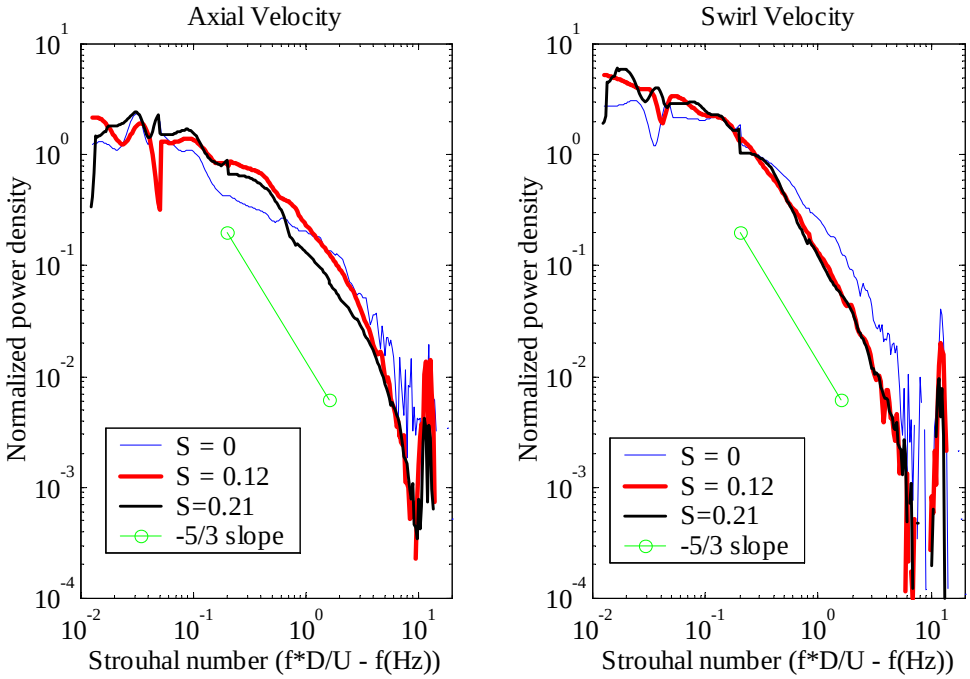

Figure 5.1: Power spectra of axial and swirl velocity for r/D_n=0.07, x/D_n=-0.35, Q=50 SCFM

the swirl velocity fluctuations are noticeably larger than the integral time scales associated with axial velocity fluctuations for non-zero swirl. At zero swirl, the integral time scales and entire spectrum shape are the same for both axial and swirl velocity fluctuations. This is expected as the underlying turbulent state is nearly isotropic in its entirety. The extension of the apparent inertial subrange for swirl indicates an increase in the efficiency of transport down the energy cascade. In other words, the presence of swirl in this part of the flow field is associated with a more efficient transport of energy from the energy containing scales to the dissipative scales.

Both velocity spectra also show a concentration of energy around a Strouhal number of 11. The magnitude of the frequency leads to the suspicion that the fluctuations measured are acoustic in nature. The dimensional frequency corresponding to a Strouhal number of 11 is about 900 Hz, which is close to the cut-on frequency of the first azimuthal mode of the downstream test section. The cut-on frequency can be calculated analytically to be 909 Hz (Kinsler et al., 1999). The reason an

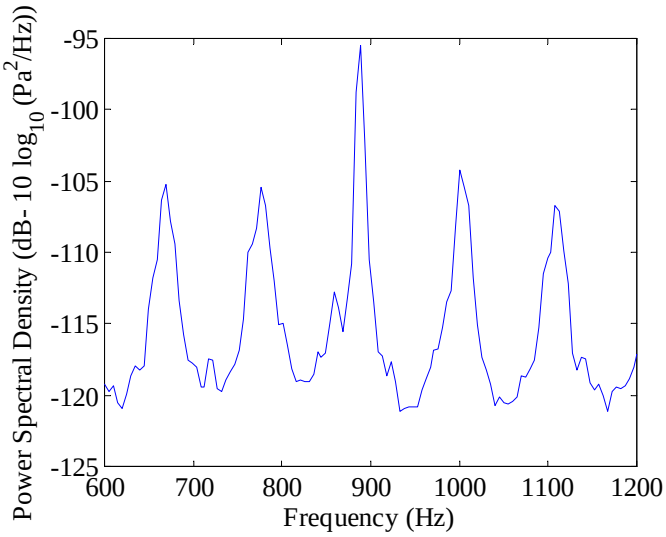

Figure 5.2: Power spectrum of pressure fluctuations near expansion

azimuthal mode is suspected stems from the fact that both swirl and axial velocity spectra contain the peak. A longitudinal acoustic mode would only exhibit axial velocity fluctuations. A power spectrum of pressure fluctuations in the nozzle is shown in Figure 5.2. Indeed, a relatively significant peak in pressure can be detected at the frequency of interest. The surrounding peaks, related to higher order axial modes, are one order of magnitude lower.

It must be underlined that the similarity of power spectra shown in Figure 5.1 is achieved in spite of the very significant differences in the original energy contained in the fluctuations. Figure 5.3 shows the time histories of axial and swirl velocity at the same conditions as Figure 5.1. The time histories are taken from the beginning of the middle data block collected. The time histories clearly reflect the large differences in energy between the different flow conditions. The histories also confirm the relationship between the integral time scales originally deduced from the power spectrum. The undulations in swirl velocity appear much slower than the undulations in axial velocity. The time histories do not show any significant periodicity. The 900 Hz peak seen in the power spectra has too little power to be able to be identified in the time

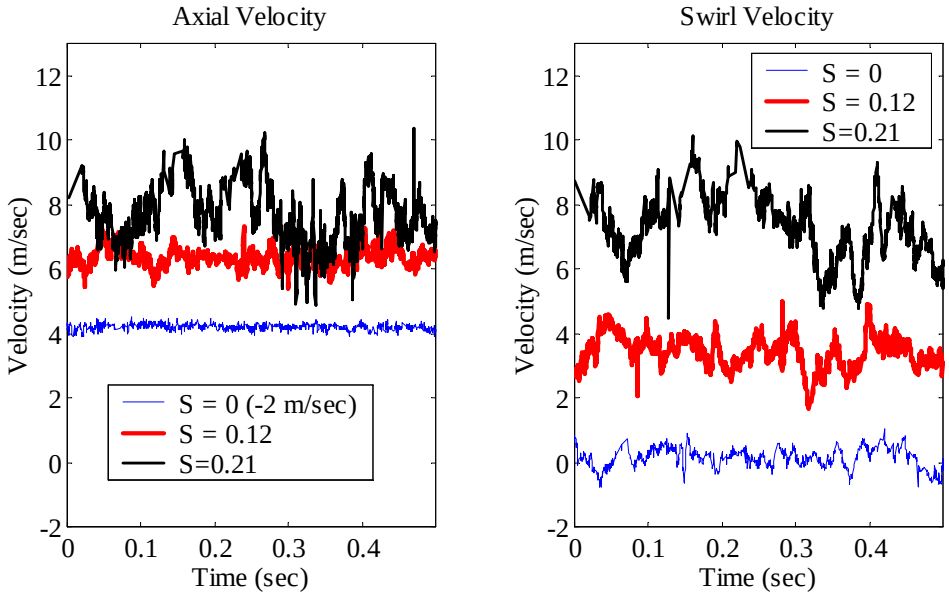

Figure 5.3: Time histories of velocity for all swirl conditions inside nozzle at r/D_n=0.07, x/D_n=-0.35, Q=50 SCFM

data.

Figure 5.4 shows three spectra along the radius for S=0.21 and Q=50 SCFM at x/D_n=-0.35. The profiles indicate that as distance from the core increases, integral time scales become lower and the distribution of energy wider. An inertial subrange can still be identified in all plots, but the frequencies for the range have increased significantly, especially for the swirl velocity fluctuations. Some of the power spectra exhibit small notches. These notches are due to the fact that the power spectra were calculated using different block lengths for different frequency ranges. The notches arise from the fact that the underlying sample time distributions are not entirely Poisson distributed causing additional offset in the Gaster estimate. The offset increases with a decreasing number of averages. The lower frequency ranges are thus especially susceptible to the offset and hence sometimes exhibit small notches instead of the expected smooth spectrum.

A small energy concentration can be found at very low Strouhal numbers of around 0.04. At this point it is not clear whether these peaks are physical, or caused

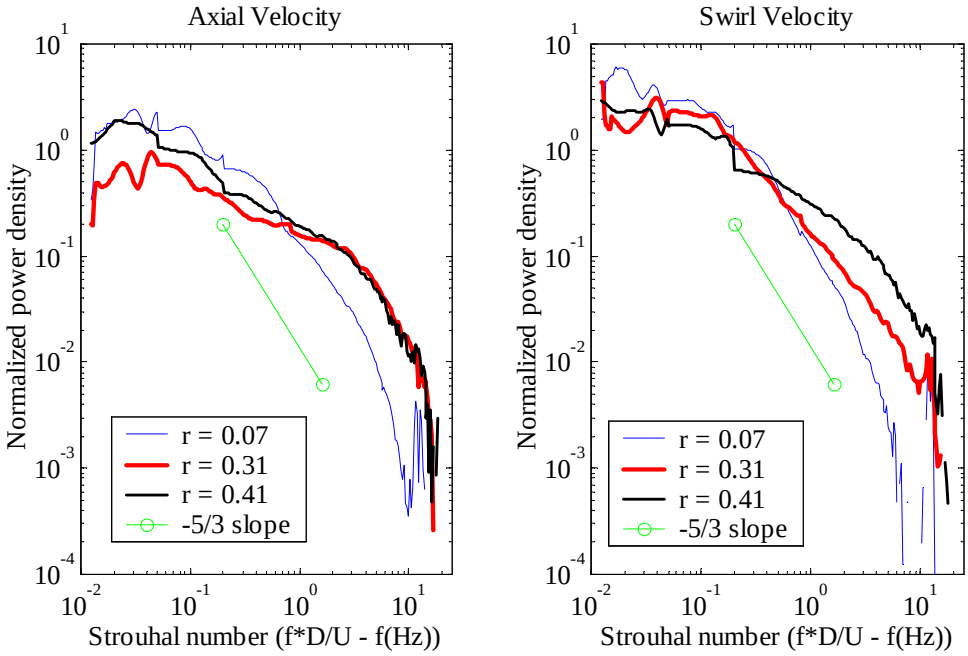

Figure 5.4: Radial comparison of spectra for S=0.21, x/D_n=-0.35, Q=50 SCFM

by variance in the power estimate at low frequency. The peaks are seen in both the swirl and axial velocities near the core and only in the swirl velocity towards the outer parts of the flow. The 900 Hz peak also can still be identified in the data although this becomes more difficult as the inertial subrange extends to higher frequencies. The fact that the 900 Hz peak is invariant with both flow condition and physical location in the flow lends further strength to the conclusion that the energy seen at 900 Hz stems from acoustic oscillations that are superposed on the turbulent velocity fluctuations.

Figure 5.5 shows the power spectra calculated for two different flow rates at r/D_n=0.07, x/D_n=-0.35 and S=0.12. The flow profile comparisons showed that the normalized results are not a strong function of flow rate. The results of Figure 5.5 show that this is still the case for the swirl velocity spectrum. The only significant difference seen here is the fact that as expected, the higher Reynolds number flow has a smaller integral time scale. Due to the limit in LDV sampling frequency, not the entire inertial subrange of swirl velocity fluctuations could be resolved for the higher

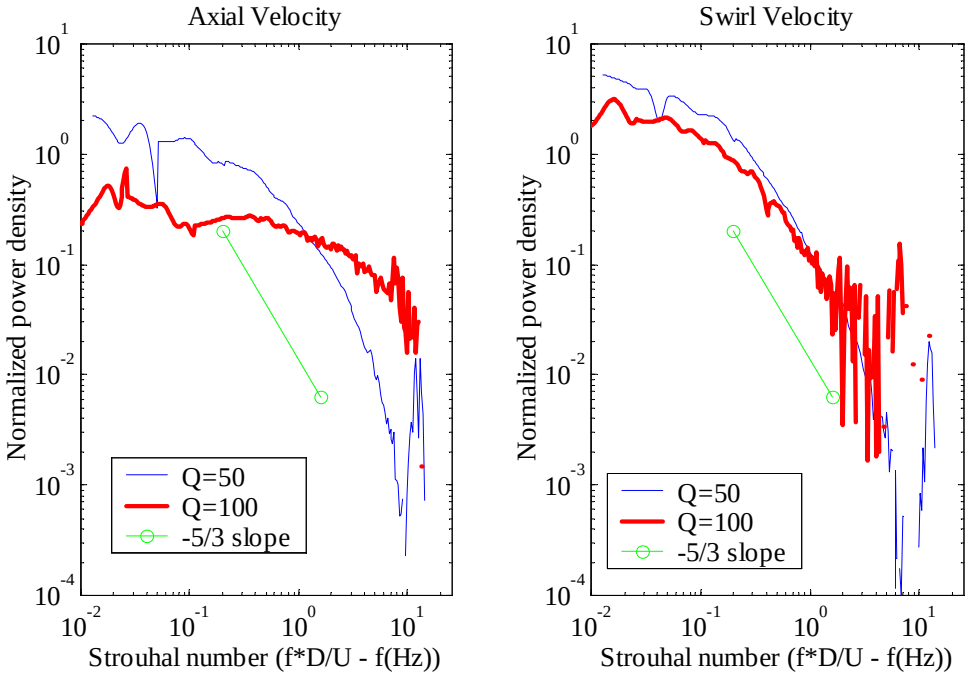

Figure 5.5: Comparison of spectra for two flow rates at S=0.12, x/D_n=-0.35

flow-rate. The integral time scale of the axial velocity fluctuations at the higher flow rate is significantly lower compared to the lower flow rate. Additionally, even though the frequency scale has been normalized, the extent of energy containing time scales is significantly extended. At the highest resolved frequency range, the power spectrum of axial velocity fluctuations at 100 SCFM barely begins to show a linear slope. The difference in time scales between the axial and swirl velocity fluctuations was noted earlier but seems to be magnified for the 100 SCFM flow rate. It is clear that although the time mean statistics at the two flow rates are very similar, the underlying dynamic state can exhibit significant differences.

Figure 5.6 shows the radial variation of axial and swirl velocity power spectra for x/D_n=-0.35, S=0.12 and Q=100 SCFM. As was noted for the case of S=0.21, Q=50 SCFM, the power spectrum of velocity fluctuations extends to higher frequencies outside the vortex core. Correspondingly, the integral time scales of the motions also decrease. The large disparity observed between the frequency extent of axial and swirl velocity fluctuations is absent outside the vortex core as well. Axial and swirl

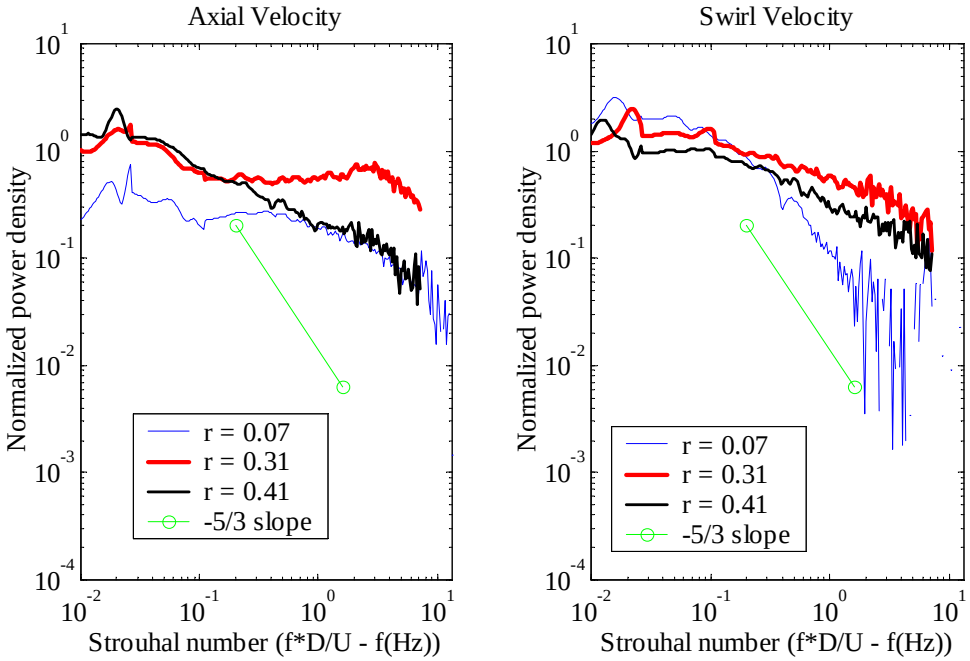

Figure 5.6: Radial comparison of spectra for S=0.12, x/D_n=-0.35, Q=100 SCFM

velocity fluctuations appear to contain energy over nearly the same frequency range. For the large swirl condition, the disparity was seen to persist outside the vortex core.

Figure 5.6 shows a wide local maximum in the axial velocity power spectrum around St=3. The energy excess shown around that frequency band is only seen near the radial location r/D_n=0.31. It is not observed in the swirl velocity spectrum and is absent in the core of the flow as well as near the wall. Figure 5.7 shows the radial variation of power spectra under the same conditions except for Q=50 SCFM. The excess can also be observed here, near the same Strouhal number as for the higher flow-rate. Similar to the 100 SCFM case, the frequency extent of energy containing fluctuations does not differ between axial and swirl velocity fluctuations outside of the vortex core.

Figure 5.8 shows axial variation of the velocity power spectra at r/D_n=0.31, S=0.12, Q=100 SCFM. Note that the y-axes have been re-scaled to zoom in on the feature in question. The energy excess observed in the previous two figures is also seen here as the flow develops. The relative magnitude of the local maximum seems to

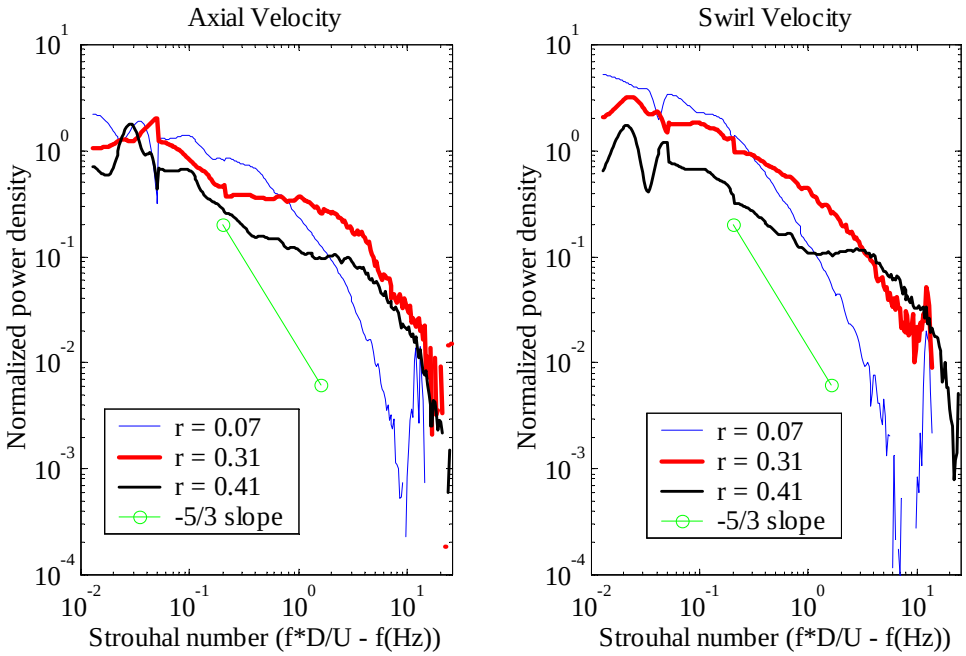

Figure 5.7: Radial comparison of spectra for S=0.12, x/D_n=-0.35, Q=50 SCFM

be increasing slightly. More easily identified is the decrease in the integral time scale of fluctuations as the flow develops downstream. The increase in time scale appears to be unrelated to the local maximum in axial velocity fluctuations, because the swirl velocity spectrum exhibits the same trend. The decrease in the integral time scale as the flow evolves downstream in the nozzle can be understood as the influence of the growing shear layers at the center and boundary of the flow. As the shear layer grows the scales of the associated turbulence can also be expected to grow. As the spatial scales increase, the associated time scales also increase as the predominant velocity scale remains constant. The question of the origin of the local maximum in the axial velocity spectrum remains and will be addressed again when the combustor velocity dynamics are studied.

The power spectra calculated for the nozzle flow field exhibit an interesting range of behavior in terms of the distribution of the time scales of turbulence. Longer time scales are observed in the vortex core where the overall fluctuation energy is greatest. A significant difference between the time scales of axial and swirl velocity fluctuations

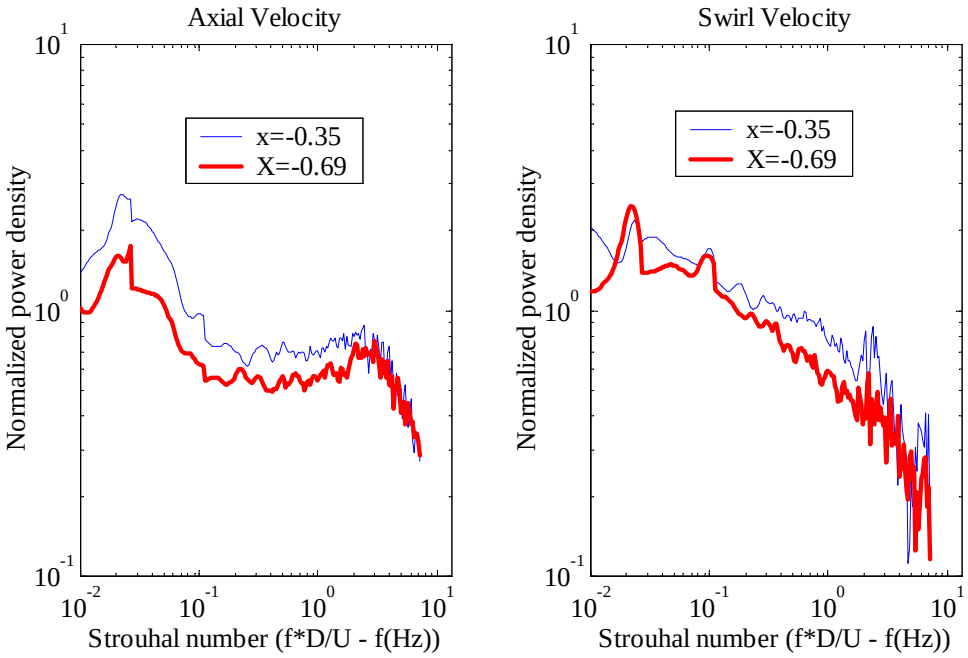

Figure 5.8: Axial comparison of spectra for S=0.12, r/D_n=0.31, Q=100 SCFM

is found at the core. The difference decreases with increasing radius and decreasing swirl. The higher integral time scales at the centerline are consistent with the narrower bandwidth of fluctuations. It is also important to remember that the core exhibits large shear stresses under swirling conditions. These shear stresses are effective in redistributing mean momentum.

Using the spectral characteristics it is now possible to postulate how the flow is able to maintain stability while producing a large amount of turbulent energy. It is clear from the RMS velocity distributions that the energy produced accumulates more in the swirl velocity component than in the axial velocity component. Based on the spectra shown here, the reason for this is that swirl fluctuations are more easily dissipated. The range of time scales which provide a pipeline to dissipation is much wider for the swirl velocity. The radial and azimuthal motion of the vortex core allows the center of the flow to lose energy efficiently to the surrounding fluid via the shear caused in the azimuthal direction by such motion.

The breakdown of the vortex core can then be associated with the inability

of small motions of the core to lose enough turbulent energy. Larger and larger deflections occur and eventually do not allow the core to recover. This picture explains why at 100 SCFM, the vortex core breaks down sooner. The increased production of turbulence at the higher flow rate is confined to the same area. The core movement can only provide a finite amount of energy dissipation and this level of movement is reached sooner at the higher flow–rate.

This picture is also consistent with the significant amount of low frequency energy contained in velocity fluctuations near the vortex core. The low frequency energy increases with increasing swirl, consistent with the idea that the motion of the core increases with increasing swirl to provide more effective dissipation of the increased turbulence production. The idea that a certain limit of turbulent energy can be contained at the vortex core before the flow becomes unstable and breaks down will be examined in detail in Chapter 6.

5.2.1.2 Combustor flow dynamics

The dynamics of the flow field downstream of the sudden expansion are expected to yield an especially rich dynamic picture since the flow field is rapidly evolving and a lot of turbulent energy is created, transported and dissipated. Similar to the nozzle flow, it is expected that fluctuation spectra will allow further insight into the processes responsible for the evolution of the flow field described in Chapter 4.

Figures 5.9 and 5.10 show the radial variation of axial and swirl velocity power spectra for the condition of zero swirl at x/D_n=0.44 and Q=50 SCFM. Figure 5.9 shows inner radial locations whereas Figure 5.10 shows mostly radial locations outside the outer shear layer. The time scales associated with fluctuations in the inner flow appear to be relatively constant. In the outer shear layer however, at r/D_n=0.66 significantly larger integral time scales are found. Figure 5.10 shows that the entire outer region of the flow beyond the outer shear layer is dominated by energy distributions exhibiting a large amount of low frequency energy and large integral time scales relative to the inner portion of the flow.

The long continuous downward slope of the spectra indicate an efficient transfer

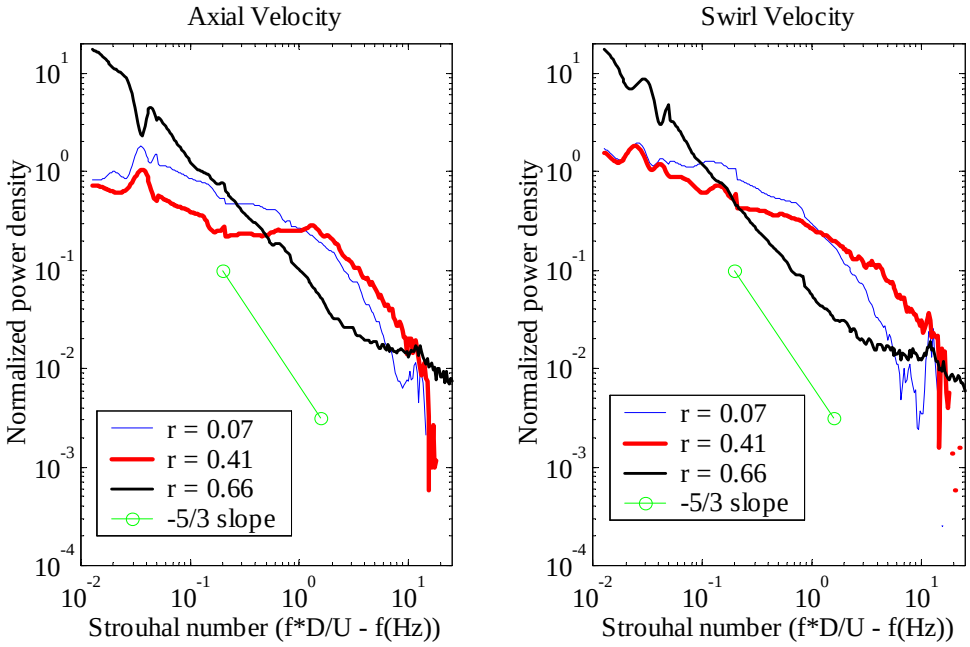

Figure 5.9: Radial comparison of power spectra for x/D_n=0.44, S=0, Q=50 SCFM (inner flow)

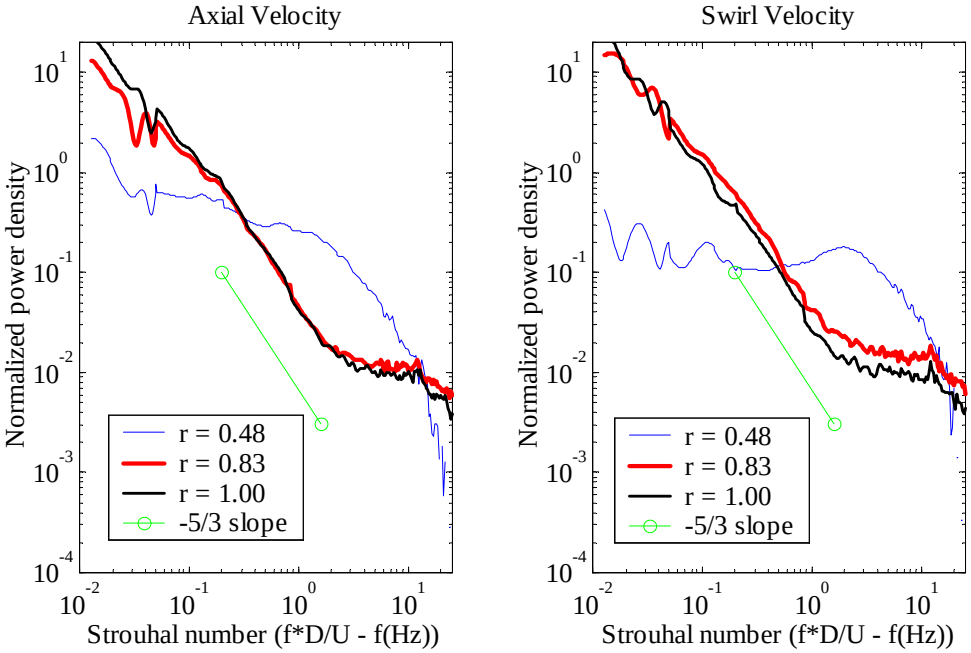

Figure 5.10: Radial comparison of power spectra for x/D_n=0.44, S=0, Q=50 SCFM (outer flow)

of energy from the largest to the smallest dissipative scales. The shear layer is still very thin at x/D_n=0.44 and the energy increase in the spectrum is expected to be broadly distributed in the spectrum. Figure 5.10 shows the power spectra of a radial point located right at the center of the shear layer. No spectral concentration of fluctuations can be observed in the axial velocity spectrum, but the swirl velocity spectrum has a significant local maximum around a Strouhal number of 3. It is interesting to note that the integral time scale of swirl velocity fluctuations is lower than the integral time scale of axial velocity fluctuations. The lack of energy in the swirl fluctuations allows the broadband energy at St=3 to be more visible. The existence of low frequency energy masks the same increased at energy at St=3 for axial fluctuations.

Figure 5.11 and Figure 5.12 mirror Figures 5.9 and 5.10. Consistent with the observations made for the nozzle flow, the addition of swirl causes an increase in the integral time scales in the inner parts of the flow. Figure 5.12 shows that inside the shear layer, the swirl induced lower integral time scales combine with the broadband energy production around St=3. However, for both axial and swirl velocity fluctuations, the local maximum is masked by the increased low frequency energy.

The concentration of energy around St=3, can be related to the shear layer induced production of turbulence. At x/D_n=0.44, the shear layer is relatively thin and, as will be seen in Chapter 6 amplifies energy over a very wide range of frequencies. The resultant spectral distribution at a given axial location is a function of the integrated effect of broadband amplification of energy and the initial spectral energy distribution. Swirl appears to have little effect on the amplification properties of the flow, even though it clearly has a strong influence on the overall energy distribution in the flow field.

Figure 5.12 in comparison to Figure 5.10 shows that the addition of swirl has little influence on the energy distribution in the outer parts of the flow field, beyond the outer shear layer. The similarity in the spectra is not surprising considering that the RMS velocity distributions in this part of the flow field are nearly identical for all swirl conditions.

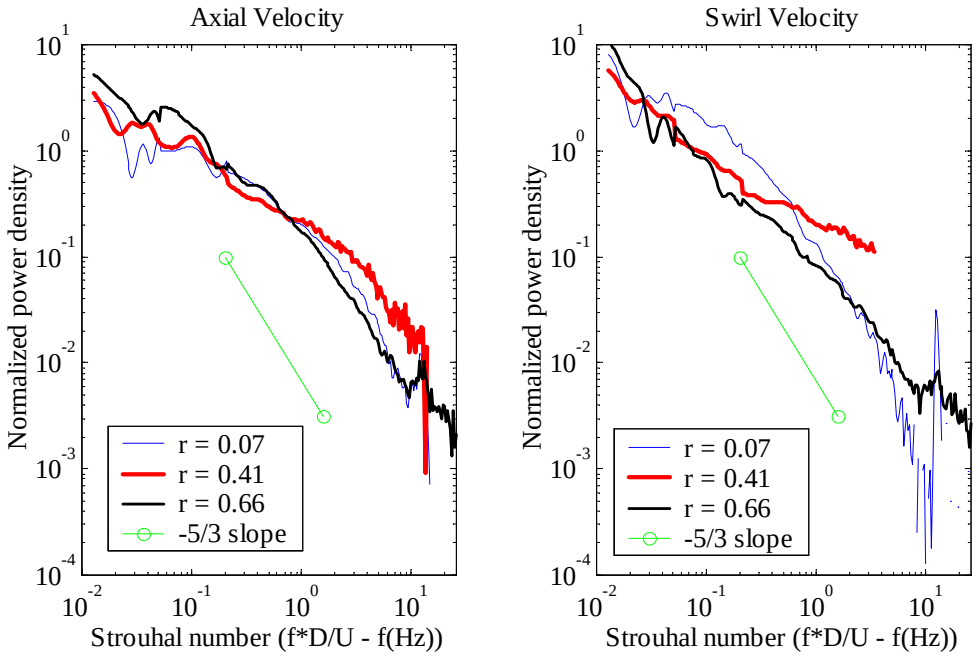

Figure 5.11: Radial comparison of power spectra for x/D_n=0.44, S=0.12, Q=50 SCFM (inner flow)

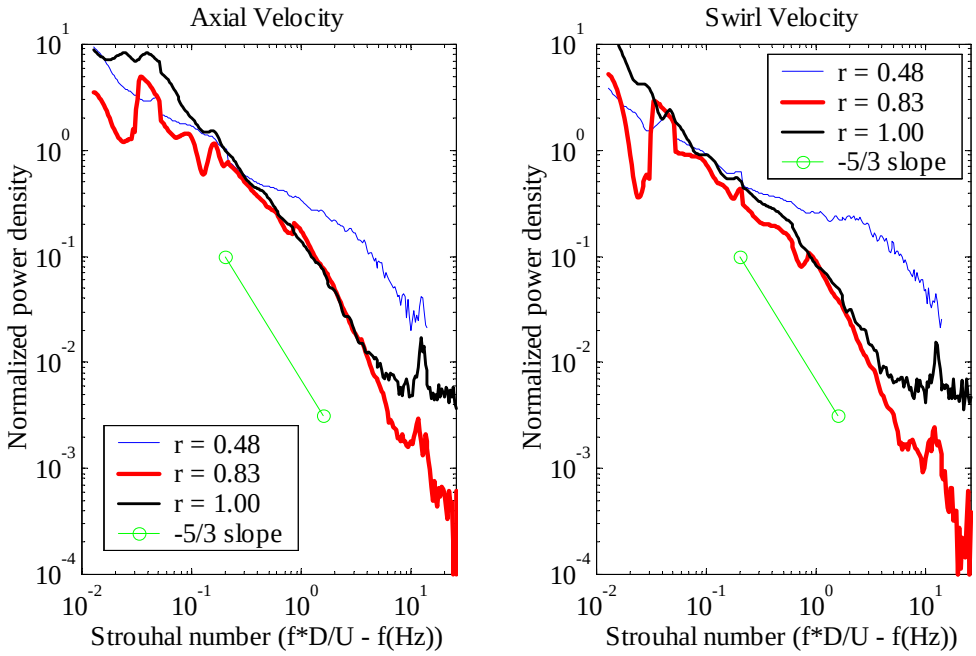

Figure 5.12: Radial comparison of power spectra for x/D_n=0.44, S=0.12, Q=50 SCFM (outer flow)

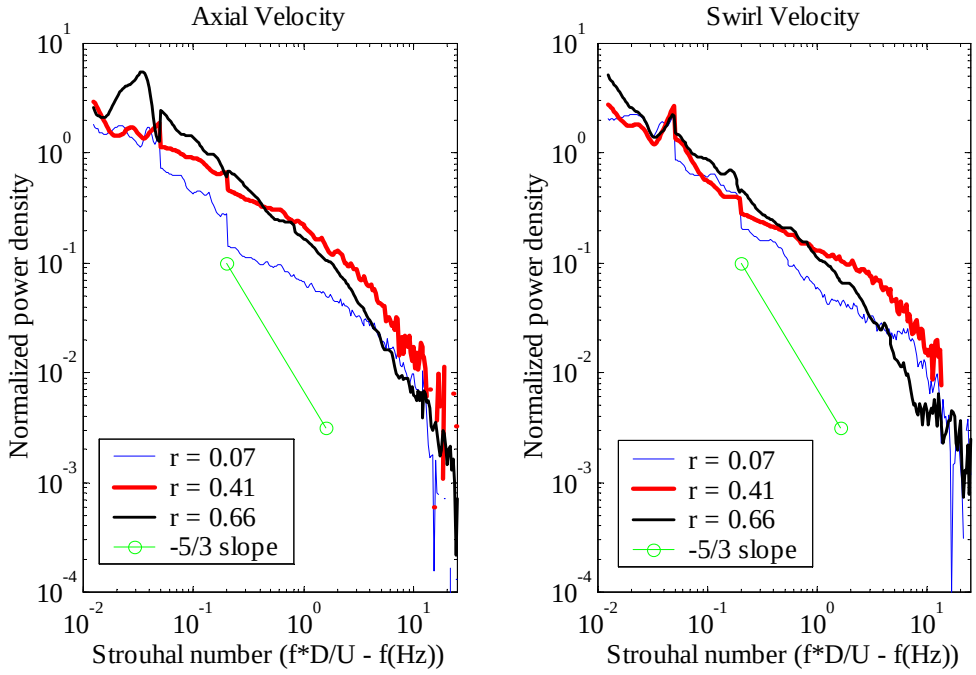

Figure 5.13: Radial comparison of power spectra for x/D_n=0.44, S=0.21, Q=50 SCFM (inner flow)

Figure 5.13 shows a comparison of the normalized power spectra of velocity fluctuations at three radial locations in the main part of the flow for x/D_n=0.44, S=0.21 and Q=50 SCFM. Figure 5.14 overlaps Figure 5.13 in radial location and shows the spectra for points located outside the outer shear layer of the incoming flow. In both the inner and outer flow, the time scales of swirl and axial velocity fluctuations have become nearly the same. The significant radial variation of the frequency extent of the energy containing swirl velocity fluctuations is not observed at x/D_n=0.44. The spectra of the flow field outside the shear layer resemble those of the swirl velocity at the centerline of the nozzle. The difference is that here in the recirculation region of the incoming jet, both swirl and axial velocity fluctuations exhibit the increase in integral time scale and have an inertial subrange that extends to lower frequencies, as remarked above.

Figures 5.13 and 5.14 also show several sharper spectral features in the very low range of Strouhal numbers, below St=0.1. Previous figures exhibit similar features

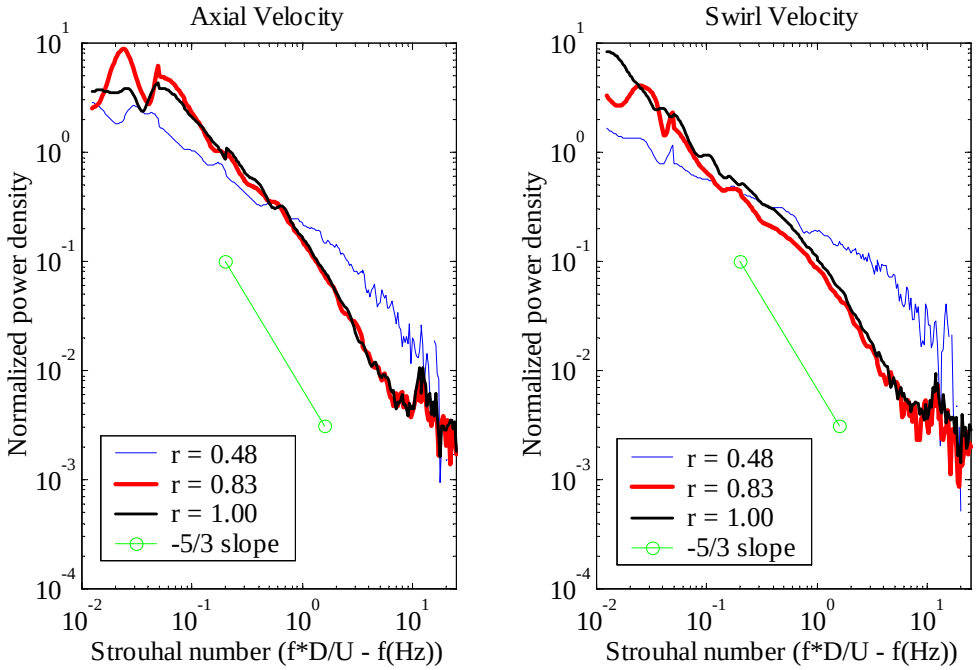

Figure 5.14: Radial comparison of power spectra for x/D_n=0.44, S=0.21, Q=50 SCFM (outer flow)

and the discussion that follows also applies to those cases. The time histories of velocity for several data points are used to examine whether or not these peaks correspond to large scale coherent motion or are merely due to a larger variance in the spectral estimate at low frequency. Figure 5.15 shows the time history of velocities at r/D_n=0.41, x/D_n=0.44, S=0.21, Q=50 SCFM. While the axial velocity fluctuations do not exhibit significant coherent oscillations, the swirl velocity clearly shows sinusoidal motion with a frequency of around 4 Hz which corresponds well with the small spectral peak observed in the spectrum in Figure 5.13 near St=0.05. The oscillations observed modulate the higher frequency turbulent fluctuations. Towards the end of the time record, however, the coherence appears to decrease as the oscillations become blurred. The superimposed turbulence fluctuations remain constant throughout the record.

A peak at nearly the same frequency is observed in Figure 5.14 in the axial velocity spectrum. A corresponding time record is shown in Figure 5.16. No coherent

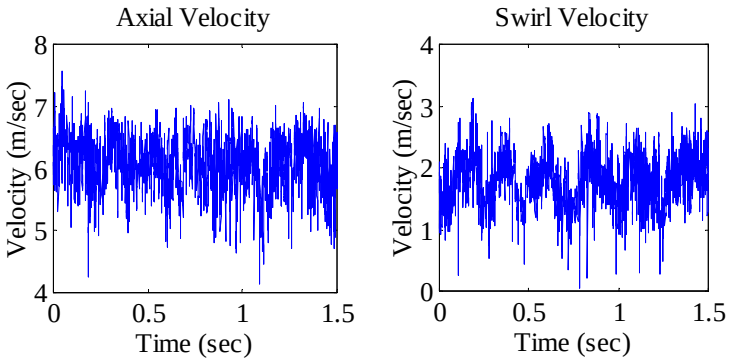

Figure 5.15: Time history of axial and swirl velocity for r/D_n=0.41, x/D_n=0.44, S=0.21, Q=50 SCFM

fluctuations can be distinguished in the time record. This does not imply that coherent fluctuations are never present at this point in the flow field. The snap shot presented in Figure 5.16 just doesn't show them. Figure 5.15 showed how the fluctuations can lose their coherence gradually. The appearance and disappearance of coherent fluctuations is not surprising considering the very large amount of energy in the flow. In the initial times of Figure 5.15, the turbulence seems superimposed on the wave. This is the picture of instability and turbulence interaction assumed when a linear stability analysis is performed in turbulent flow. The turbulence and instability related velocity fluctuations appear independent. However in the latter parts of the time record the wave becomes smeared and hard to distinguish from the rest of the turbulence. The smearing and mixing observed can be postulated to be due to the fact that the turbulence in the flow has significant energy at frequencies surrounding the oscillation frequency. This energy then overwhelms the energy in the oscillation and makes it lose coherence. The spectrum at such points will be similar to the spectra observed here, a small peak at the frequency of instability and a lot of energy surrounding it. However, short-term coherence may also be due to the fact that randomly, for short periods of time (on the order of the wavelength of oscillation) a significant amount of energy accumulates at a certain frequency in the spectrum. The concentration is not due to instability and therefore eventually

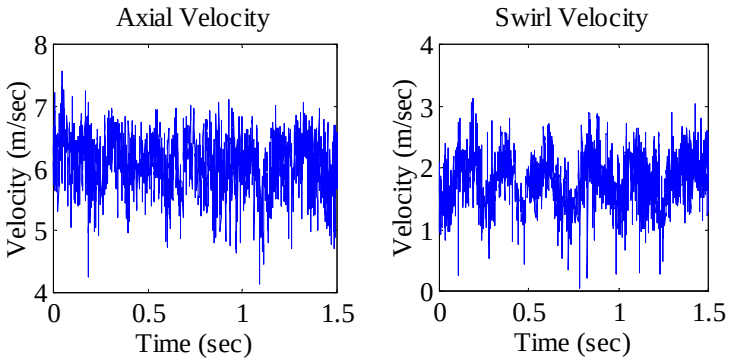

Figure 5.16: Time history of axial and swirl velocity for r/D_n=0.83, x/D_n=0.44, S=0.21, Q=50 SCFM

decays as the energy is again redistributed randomly. The latter explanation is more plausible because the low frequency peaks are not always observed at same frequency.

Figures 5.17 and 5.18 compare the inner and outer spectral distributions for S=0.12 at 100 SCFM. As noted for the nozzle, the extent of the energy containing scales is wider for the higher flow rate. The broadband amplification seen for St=3 at 50 SCFM can still be identified at the same Strouhal number for 100 SCFM. The underlying spectrum again contains relatively large integral time scales. The power spectra outside the outer shear layer are very similar to the spectra obtained at 50 SCFM.

Figure 5.19 shows the radial variation of velocity spectra for x/D_n=0.97, S=0.12, Q=50 SCFM. The variation shows the influence of the in-tact vortex core as the integral time scale for the location near the centerline is higher than the integral time scales for the other locations shown. Away from the centerline the spectra of axial and swirl velocity are very similar exhibiting a long downward, approximately linear slope.

The power spectral density of the point r/D_n=0.07 in Figure 5.19 once again contains a small concentration of spectral energy near a Strouhal number of 0.05. The experimental conditions are different here though with S=0.12 instead of 0.21. Figure 5.20 shows a time snapshot of the velocity field at this location. Similar to

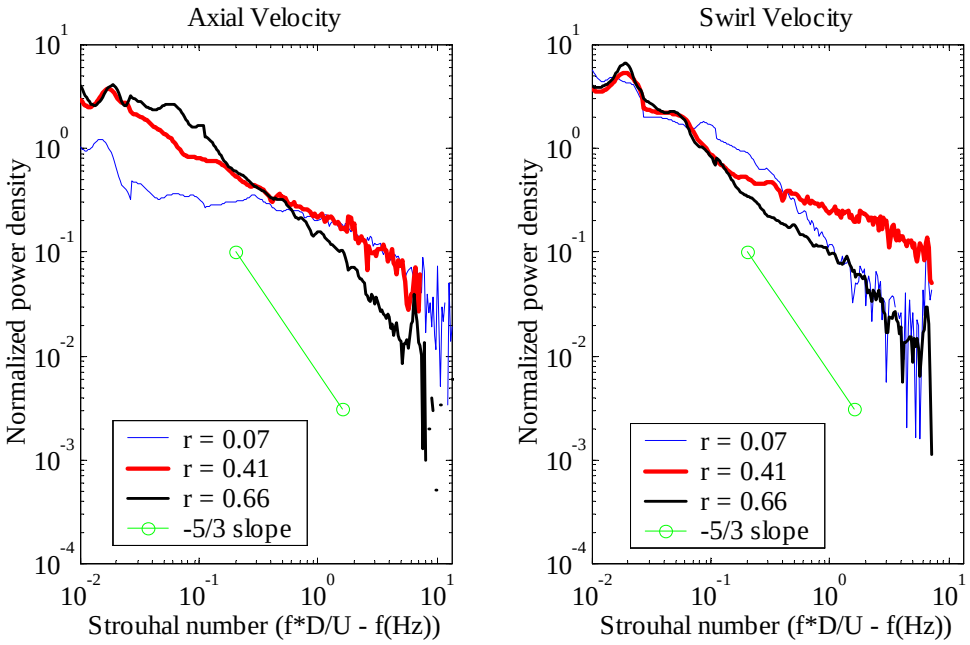

Figure 5.17: Radial comparison of power spectra for x/D_n=0.44, S=0.12, Q=100 SCFM (inner flow)

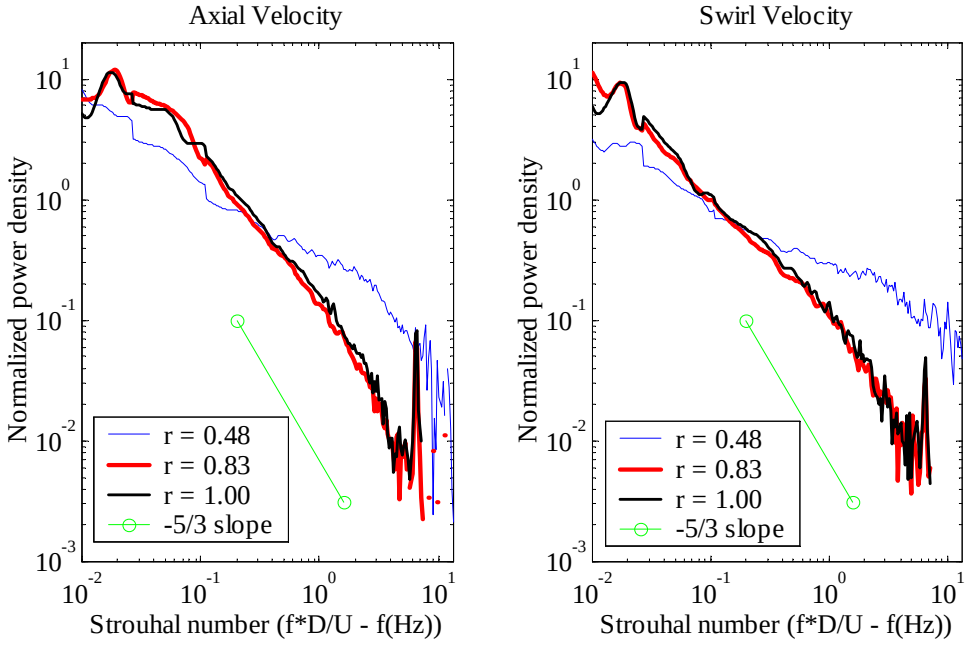

Figure 5.18: Radial comparison of power spectra for x/D_n=0.44, S=0.12, Q=100 SCFM (outer flow)

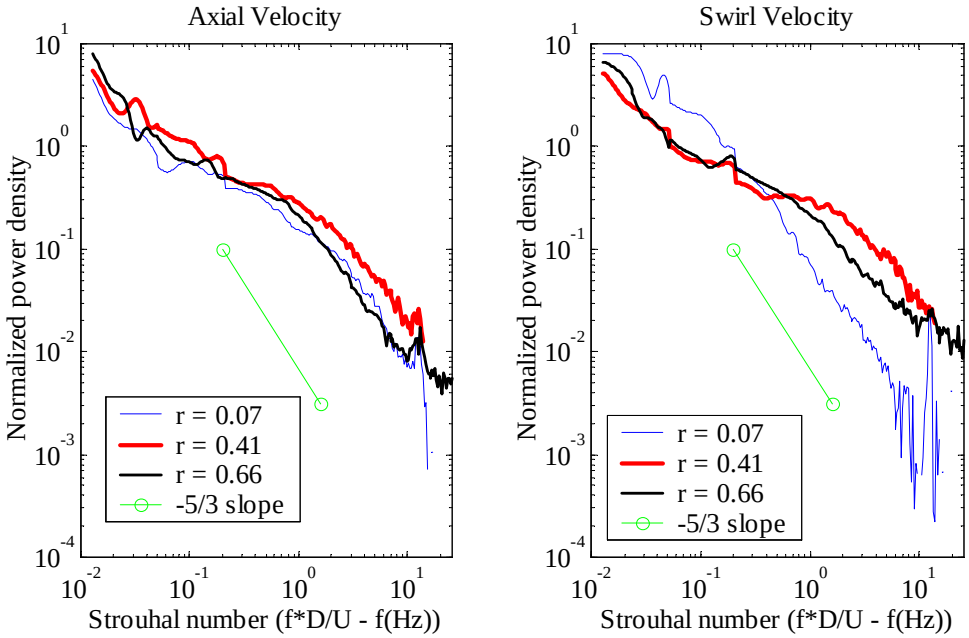

Figure 5.19: Radial comparison of spectra for x/D_n=0.97, S=0.12, Q=50 SCFM

Figure 5.15, the axial velocity does not exhibit coherent fluctuations. However, large coherent fluctuations are observed in the swirl velocity. Still, the periodicity of the fluctuations in Figure 5.20 appears to be somewhat blurred by the superimposed turbulence, as was seen in Figure 5.15.

Whether or not these low frequency coherent motions actually correspond to true flow instabilities must be put in question with their apparently near random occurrence. However, the behavior clearly shows that in strongly turbulent flows, shear layer instabilities will be difficult to excite because of an abundance of energy surrounding the excitation frequency. In order for excitation to produce highly coherent structures, the excitation must match or exceed the energy of the turbulent fluctuations which is difficult to accomplish in the present setup. Once such high excitation is achieved, the results may not at all correspond to linear behavior. These issues may also have influenced the success of Panda and McLaughlin (1994) in their attempt to excite swirling flow. In this view sharp spectral peaks cannot be expected. Broad peaks can develop when a certain band of frequencies is consistently amplified as a flow evolves downstream. However, this situation is clearly limited to cases where the

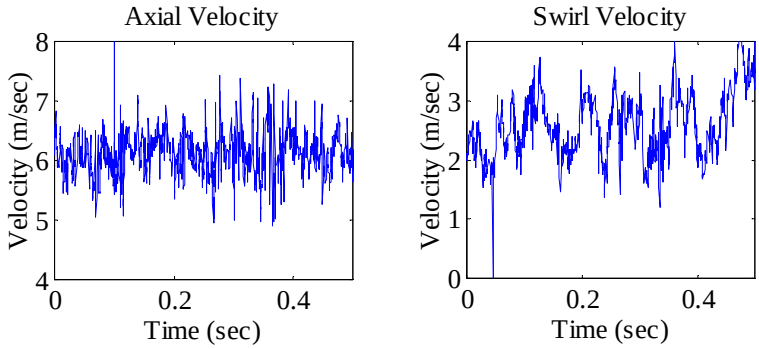

Figure 5.20: Time history of axial and swirl velocity for r/D_n=0.07, x/D_n=0.97, S=0.12, Q=50 SCFM

flow is developing relatively slowly so that the range of amplified frequencies exhibits significant overlap along the development path of the flow.

Figure 5.21 shows the radial variation of power spectra for S=0.21, 50 SCFM at x/D_n=0.97. The radial variation of the integral time scale is lost at this station. All radial locations have nearly the same integral time scale and spectral shape. The outer radial locations appear to have a slightly more linear distribution of energy in the spectrum indicating more efficient transfer to small scales. The location closest to the centerline exhibits decreasing energy for low Strouhal numbers (less than 0.4) and for Strouhal numbers above 5. In the intermediate range the slope in the spectrum is flatter possibly indicating turbulence generation. The flatter intermediate distribution is seen in both the axial and swirl velocity spectra. The range of Strouhal numbers in question is often associated with fluid dynamic instabilities, further supporting the claim that turbulence generation is interrupting the constant flow of energy to smaller scales.

Figure 5.22 shows the radial variation of velocity spectra for the S=0, Q=50 SCFM case at x/D_n=3.14. The jet is at this point near the end of its initial development stage, with the potential core still visible. The axial velocity fluctuations exhibit a wide and significant concentration of spectral energy around a Strouhal number of 0.4. The swirl velocity spectrum also shows traces of added energy around St=0.4. This type of broadband peak can be expected in a slowly developing jet type flow,

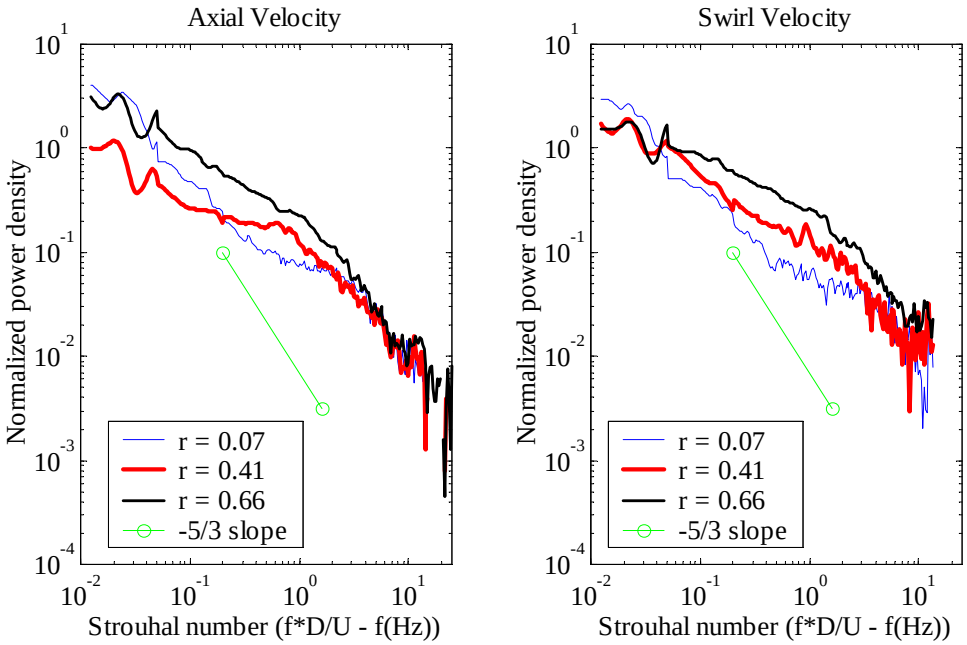

Figure 5.21: Radial comparison of spectra for x/D_n=0.97, S=0.21, Q=50 SCFM

that has significant inlet turbulence. The peak Strouhal number of 0.4 is in the range of frequencies commonly encountered for free jet shear flows (e.g. Wygnanski and Petersen, 1987). The instability found at this axial station is seen to develop starting from x/D_n=0.97. The instability development will be studied in detail in Section 5.3.

Figure 5.23 compares spectra for various radial locations in the flow for the S=0.12, Q=50 SCFM case at x/D_n=3.14. The spectra are all extremely similar. In Chapter 4 it was noted how quickly the free vortex cases with swirl develop downstream relative to the zero swirl case. The flow at this axial station has very high RMS velocity. The RMS velocity is distributed relatively evenly compared to the earlier stages of development of the flow. The radial variation in velocity spectra bears this out. All the spectra exhibit a nearly linear (on the log-log plot) decline over the entire range of Strouhal numbers able to be measured. The linear decline covers more than three decades of energy content. The slope of the line is near -5/3 but slightly shallower in some ranges of Strouhal number consistent with some continued broadband turbulence production. Overall, the long linear cascade of energy

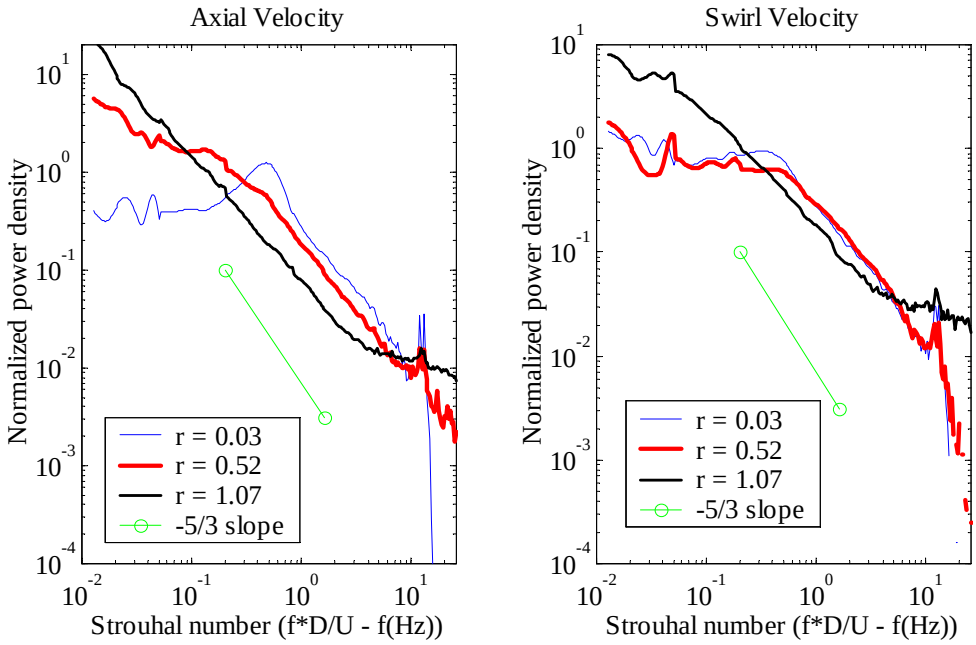

Figure 5.22: Radial comparison of spectra for x/D_n=3.14, S=0, Q=50 SCFM

shows that the flow field is set up for turbulence dissipation. Additionally, the wide range of the linear cascade is characteristic of a lower Reynolds number flow where the dissipative range of time scales overlaps with the range of energy containing time scales.

Figure 5.24 shows the radial variation of velocity spectra for S=0.12, Q=100 SCFM at x/D_n=3.14. The spectra are again very similar radially. However, a noticeable difference exists between the integral time scales of swirl and axial velocity fluctuations. The swirl velocity fluctuations have a lower integral time scale than the axial velocity fluctuations. This is contrary to the behavior seen thus far. If a difference between integral time scales was identified, the swirl velocity integral time scale was found larger than the axial velocity integral time scale.

Figure 5.25 shows the radial variation of velocity spectra for S=0.21, Q=50 SCFM at x/D_n=3.14. The results here mirror those of the S=0.12, Q=100 SCFM case. The power spectra are all very similar with the exception again that the swirl velocity integral time scale is smaller than the axial velocity integral time scale. The difference

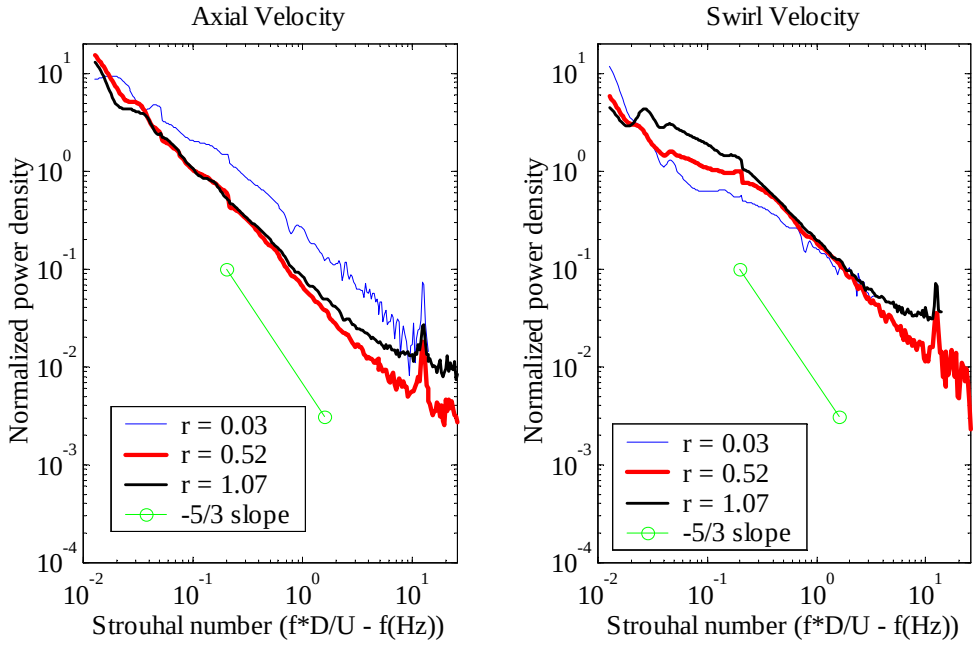

Figure 5.23: Radial comparison of spectra for x/D_n=3.14, S=0.12, Q=50 SCFM

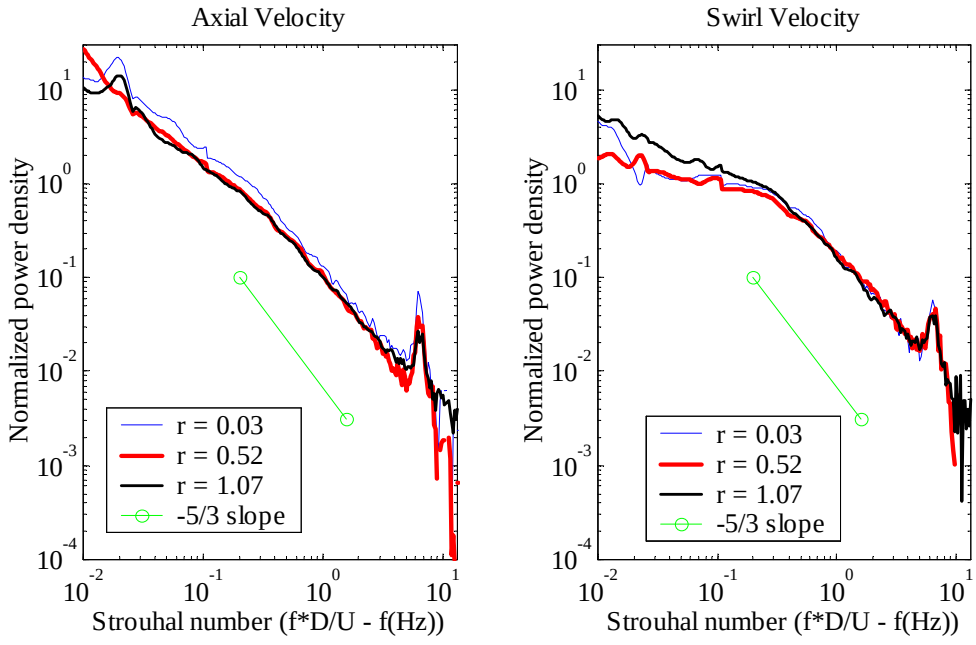

Figure 5.24: Radial comparison of spectra for x/D_n=3.14, S=0.12, Q=100 SCFM

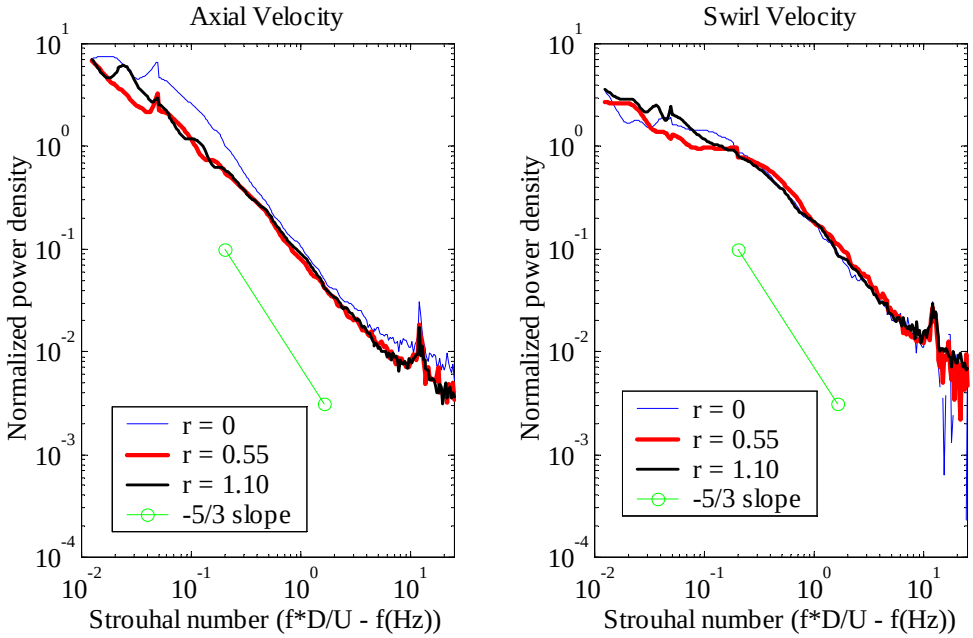

Figure 5.25: Radial comparison of spectra for x/D_n=3.14, S=0.21, Q=50 SCFM

between time scales seen here appears smaller than for the S=0.12, Q=100 SCFM case. The S=0.21 case develops the quickest of all the free vortex geometry flows studied. It is therefore possible that the integral time scales of swirl velocity fluctuations have decreased because the energy in the low Strouhal number range has begun to be dissipated. The dissipated energy is not replaced because no significant shear remains in the flow field to produce turbulent energy. The dissipation of axial velocity fluctuations is relatively slower because the axial velocity fluctuations, relative to the axial mean flow are weaker than the swirl velocity fluctuations relative to the swirl mean flow. Since dissipation scales with the cube of the strength of these oscillations, the view that dissipation is more rapid for swirl velocity oscillations is not untenable.

These observations rely on the idea that to some extent the velocity fluctuations and the energy contained in them can be considered independent for each component of velocity. This is of course not entirely true but some degree of separation exists and intuitively the results presented can for the most part be explained using the ideas relying on independence.

5.2.2 Annulus geometry

The results presented for the annulus geometry use the same normalization procedure as for the free vortex geometry. The reference length however, as in Chapter 4 is taken to be the hydraulic diameter of the annulus which is equal to 1.9 in. The reference velocities are the area mean values calculated inside the nozzle for each case. The values are given in Table 4.1.

5.2.2.1 Nozzle flow dynamics

Figure 5.26 shows velocity spectra for all swirl levels studied at x/D_h=-0.52, r/D_h=0.42. The radial location chosen is relatively close to the center–body. The spectra for S=0.60 exhibit large spectral peaks that are uncommonly narrow. These peaks are part of a larger instability in the downstream flow field. The instability will be discussed in detail below in Section 5.3. The integral time scale for the S=0.60 case is dominated by the instability time scale and thus much lower than that of the other two cases studied. Consistent with results seen in the free vortex geometry the integral time scale of the S=0.28 flow field is greater than that of the S=0 flow field. Similarly again, the axial velocity integral time scale is smaller than the swirl velocity integral time scale. For both the S=0.60, instability influenced spectra and the S=0 spectra, there are no noticeable differences in integral time scale between swirl and axial velocity. The -5/3 portions of the spectra line up very closely for all cases. Contrary to the free vortex geometry results, the swirl and axial velocity fluctuations exhibit the inertial subrange in the same range of Strouhal numbers.

Figure 5.27 shows the radial variation of spectra for the S=0, Q=50 SCFM case. Only small differences exist between the radial locations compared. A slight trend towards longer integral time scales with increasing radius may be extracted from the swirl velocity spectra. The axial velocity spectra do not exhibit the same trend. Note that the 900 Hz spectral peak found consistently in the nozzle and combustor is absent here. The absence of the peak may be due to the fact that it is masked by somewhat broader band turbulent fluctuations in the annulus geometry case. However, another

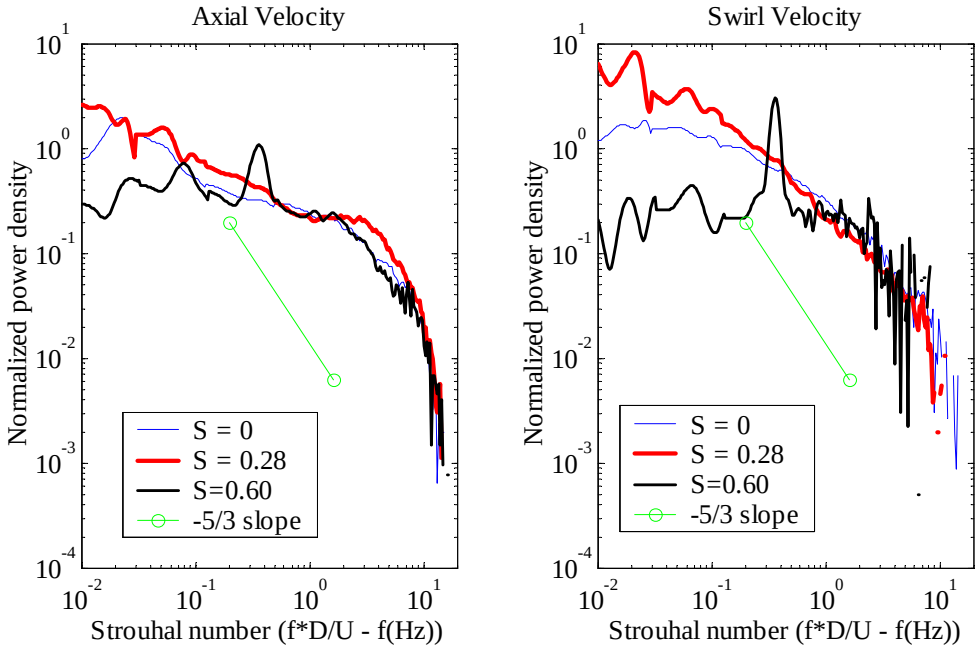

Figure 5.26: Comparison of power spectra for all swirl levels for r/D_h=0.42, x/D_h=-0.53, Q=50 SCFM

reason for the absence of the peak is that the first azimuthal mode of the downstream section cannot be admitted into the nozzle due to the presence of the center–body.

Figure 5.28 shows the radial variation of spectra for the S=0.28, Q=50 SCFM case. As already noted for Figure 5.26, the integral time scale of swirl velocity fluctuations increases with the addition of swirl. The integral time scale of axial velocity fluctuations is again found insensitive to the addition of swirl and no radial dependence of the axial velocity integral time scale can be detected. A bulge in the energy spectrum is detected around St=3, similar to the S=0.12 case for the free vortex geometry. Figure 5.28 shows that near the center–body, similar to the free vortex case, the swirl velocity fluctuations exhibit a narrower bandwidth. The outer two radial locations do not exhibit any differences in bandwidth compared to the axial velocity fluctuations.

Figure 5.29 presents the results for the radial variation of spectra at S=0.6, Q=50 SCFM, x/D_h=-0.53. The spectral peak identified in Figure 5.26 can be identified in all the spectra shown. Since these spectra are normalized by the local RMS ve-

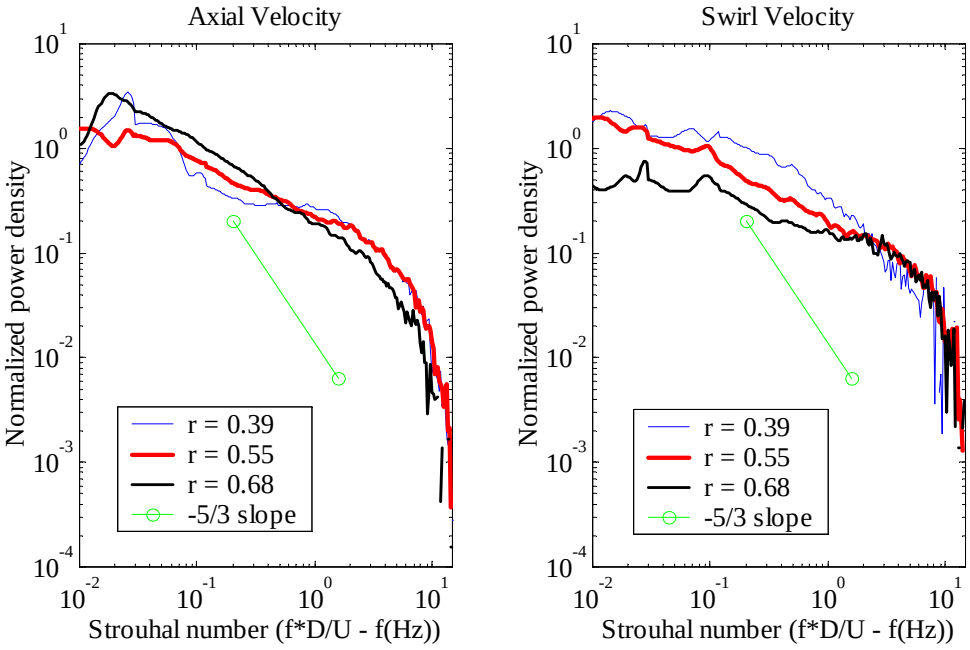

Figure 5.27: Radial comparison of spectra for x/D_h=-0.53, S=0, Q=50 SCFM

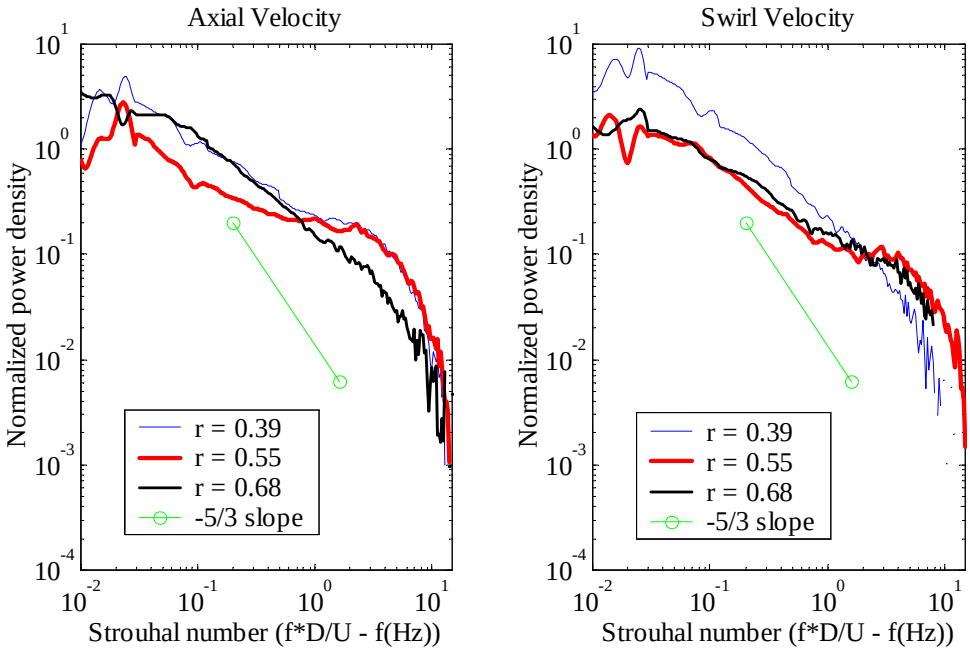

Figure 5.28: Radial comparison of spectra for x/D_h=-0.53, S=0.28, Q=50 SCFM

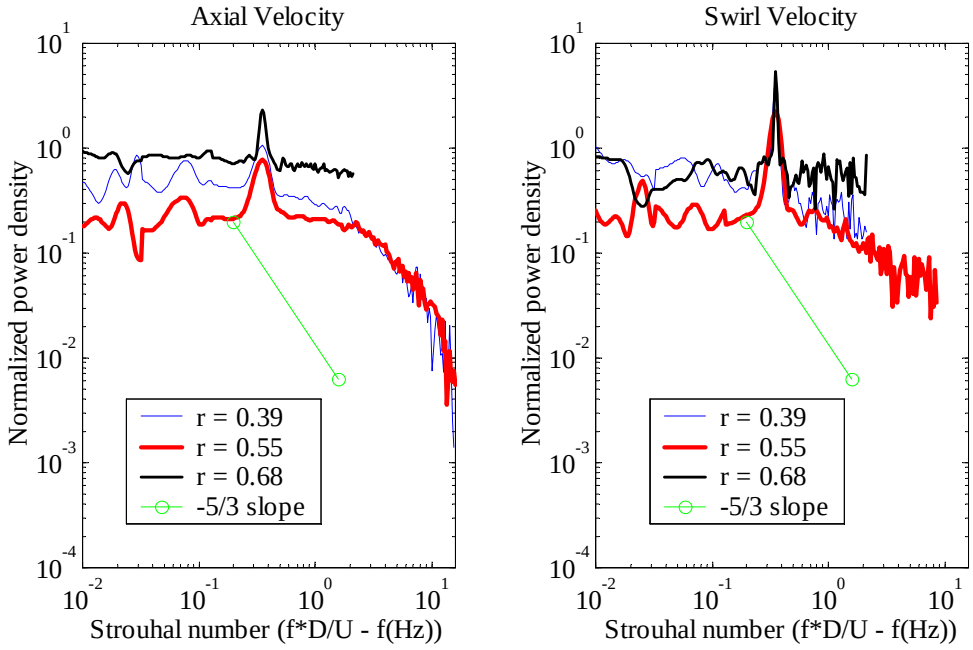

Figure 5.29: Radial comparison of spectra for x/D_h=-0.53, S=0.60, Q=50 SCFM

locity it is difficult to determine from the figure whether the oscillations are strongest in the inner or outer parts of the flow (see Section 5.3). Note that some of the spectra are cut off at relatively low Strouhal number. The reason for the cutoff is due to the difficulty of obtaining high data rates under these conditions.

Figure 5.30 compares velocity spectra at the two measured axial locations (x/D_h=-0.53,x/D_h=-1.06) for r/D_h=0.50 at S=0, Q=50 SCFM. Figure 5.31 is the analog of Figure 5.30, except for S=0.28. Both figures show clearly that little evolution takes place in the spectrum between the two axial locations at the presented radial location. Since the chosen radial location is in the middle of the annulus, no differences between the S=0 and S=0.28 integral time scales can be detected. The integral time scales of axial and swirl velocity fluctuations are also nearly the same.

Figure 5.32 shows the axial evolution of velocity spectra for the S=0.60, Q=50 SCFM case at r/D_h=0.50. The instability observed at x/D_h=-0.53, can still be observed in the upstream spectra although their strength appears to be reduced significantly. Apart from the lower instability intensity the remainder of the spectrum appears to

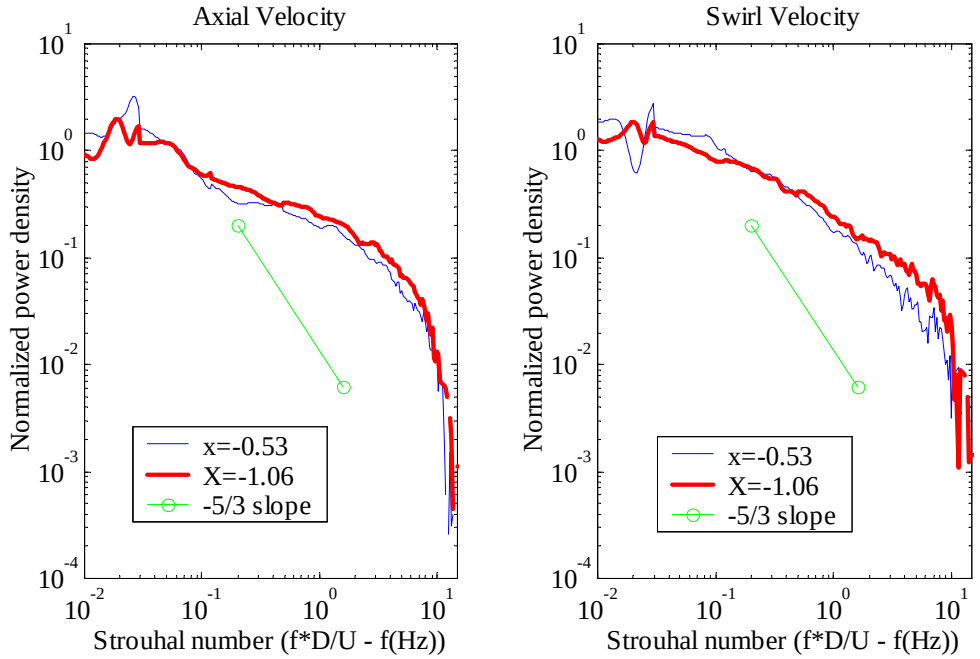

Figure 5.30: Axial comparison of power spectra for r/D_h=0.50, S=0, Q=50 SCFM

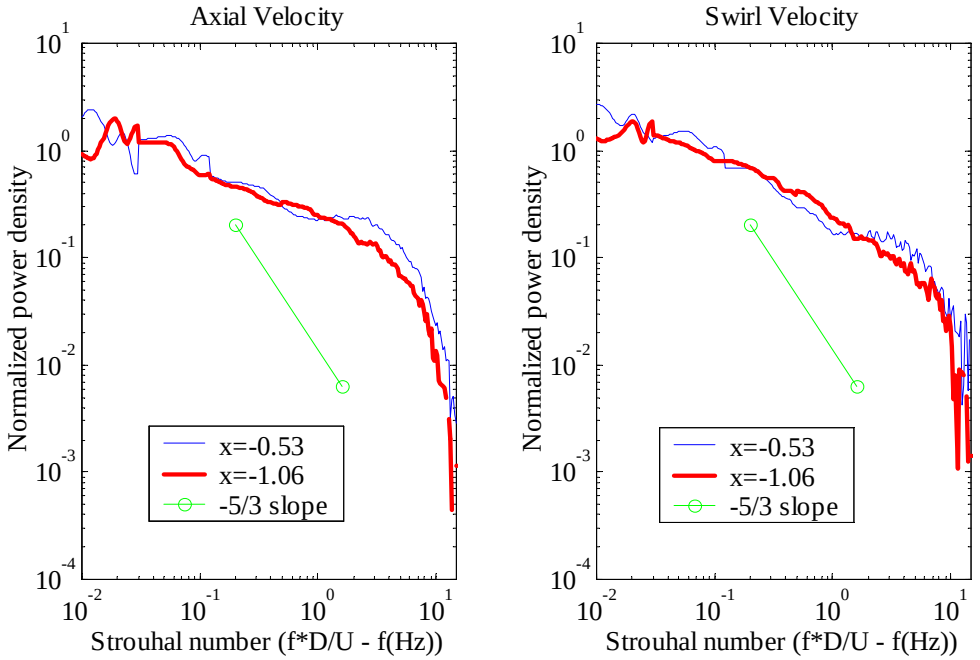

Figure 5.31: Axial comparison of spectra for r/D_h=0.50, S=0.28, Q=50 SCFM

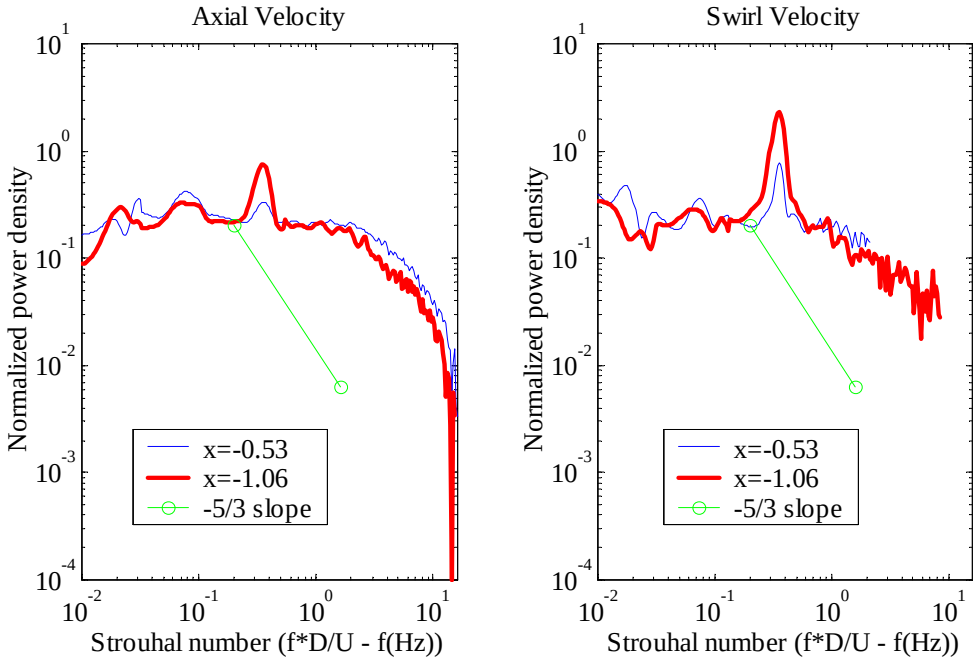

Figure 5.32: Axial comparison of power spectra for r/D_h=0.50, S=0, Q=50 SCFM

be maintain constant shape as the flow evolves downstream.

Figure 5.33 compares the spectra for both flow rates at r/D_h=0.50, x/D_h=-0.53 and S=0. The plot shows that the spectrum is a very weak function of flow rate. The similarity observed in Figure 5.33 is not surprising considering the strong similarity in mean and RMS velocity profiles observed in Chapter 4.

Figure 5.34 compares the spectra from both flow rates at r/D_h=0.50, x/D_h=-1.06 and S=0.28. Similar to Figure 5.33, no significant change in the shape of the spectra is observed when flow rate is increased. Figure 5.36 does exhibit an offset between the two curves that was not observed for the S=0 case. The offset would seem to indicate a relative decrease in the integral time scale of fluctuations. A linear decrease in the integral time scale is accounted for by the normalization of the power spectrum by the Strouhal number as discussed in Section 5.1. The decrease exhibited by Figure 5.34 thus suggests a steeper decrease in time scale. The difference observed here for the two flow rates is consistent with the differences observed in the RMS velocity profiles shown in Chapter 4, Figure 4.43. In the inner and middle parts of

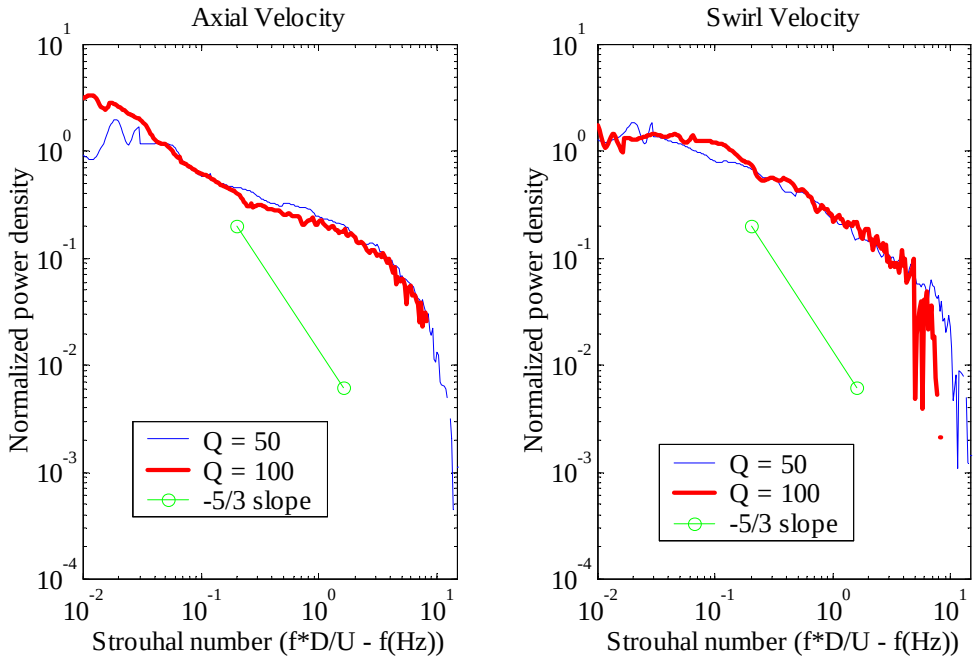

Figure 5.33: Comparison of power spectra from both flow rates at r/D_h=0.50, x/D_h=-0.53, S=0

the flow, the higher flow rate exhibits higher normalized RMS velocities. The higher RMS velocities will lead to a lower normalized integral time scale. In the outer parts of the annulus, the normalized RMS velocity profiles for the two flow rates overlap again and a plot of the velocity spectra here confirms this, Figure 5.35. Figure 5.35 also shows that the bulge in energy around St=3 observed for 50 SCFM can also be identified in the spectra of the higher flow rate case.

Figure 5.36 compared the spectra at both flow rates for r/D_h=0.50, x/D_h=-0.53 and S=0.60. The spectra show that the instability observed at 50 SCFM can also be identified at the same Strouhal number at 100 SCFM. An even larger percentage of the total energy seems to be contained in the instability related fluctuations at the higher flow rate. Overall the two spectra are remarkably similar as expected given the high degree of similarity also seen for the S=0.60 case in Chapter 4.

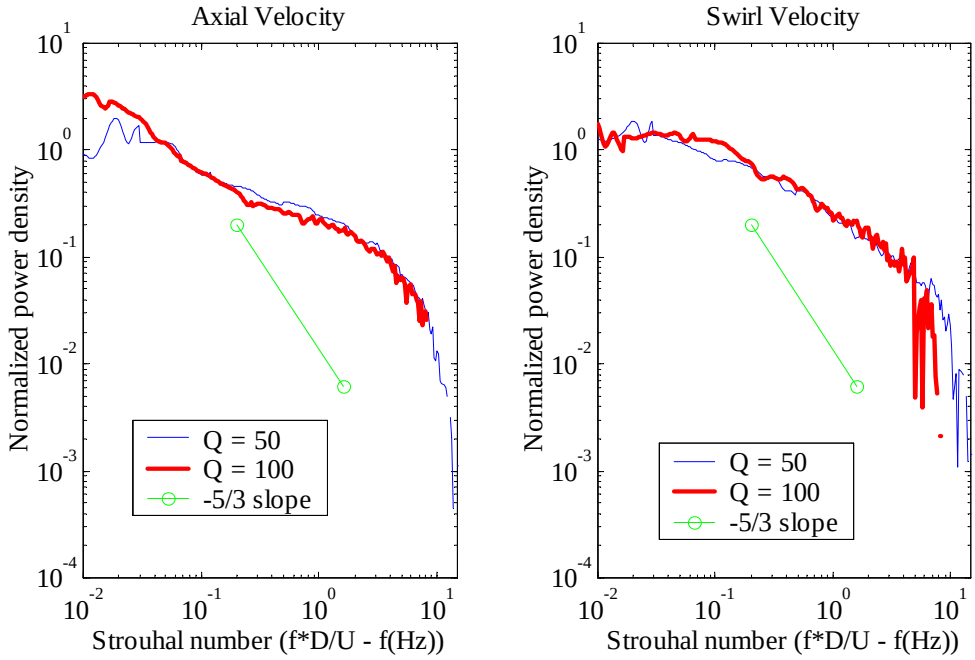

Figure 5.34: Comparison of power spectra from both flow rates at r/D_h=0.50, x/D_h=-0.53, S=0.28

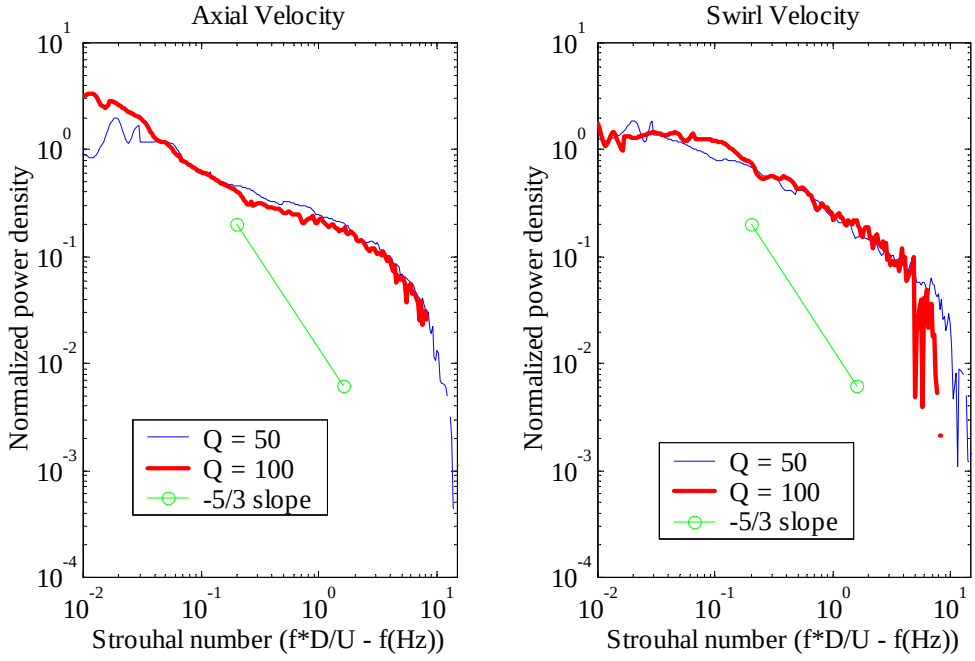

Figure 5.35: Comparison of power spectra from both flow rates at r/D_h=0.61, x/D_h=-0.53, S=0.28

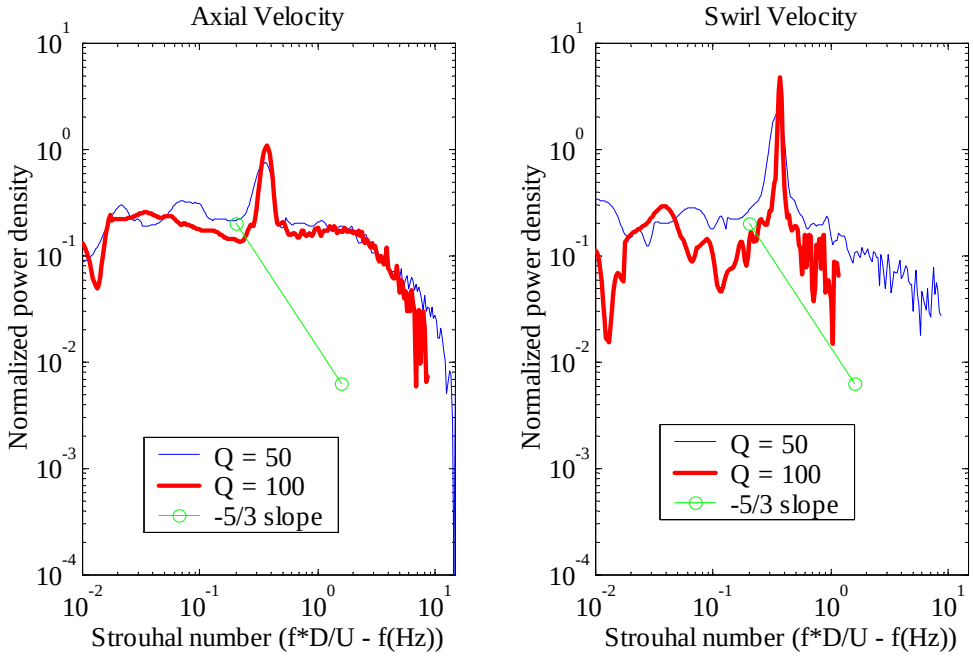

Figure 5.36: Comparison of power spectra from both flow rates at r/D_h=0.50, x/D_h=-0.53, S=0.60

5.2.2.2 Combustor flow dynamics

Figures 5.37 and 5.38 show the radial variation of the velocity spectra at x/D_h=0.68 for S=0, Q=50 SCFM in the inner and outer part of the flow field respectively. The spectra in the inner part of the flow field, including the spectra immediately behind the center–body are all very similar. In the outer shear layer (r/D_h=0.66, r/D_h=0.76), the swirl velocity spectrum exhibits a bulge of energy near St=3 as observed previously for several experimental conditions. The integral time scales do not differ for swirl or axial velocity fluctuations in any part of the flow field. However, both axial and swirl velocity fluctuations increase in integral time scale abruptly outside the outer shear layer (r/D_h=1.18, r/D_h=1.50). A linear slope is found throughout the range of Strouhal numbers captured. The long linear cascade of energy indicates a very dissipative flow where dissipation occurs over a wide range of scales. The energy source for this area of the flow is not the local flow but rather the outer shear layer. The outer recirculation zone represents the necessary means of transport for the energy.

Figures 5.38 also shows the return of the high frequency peak in the spectrum. The frequency appears shifted towards lower Strouhal numbers, which is consistent with the different normalization used for the annulus geometry. The underlying frequency has not changed. This shows that the downstream duct acoustics have not changed significantly with the addition of the center–body. The center of the flow field does not show the high frequency acoustic peak in most plots because the velocity fluctuation energy is high enough to mask the acoustic peak. In the nozzle the RMS velocities are much lower in most cases and the absence of the high frequency peak in these cases can be associated with the fact that the first azimuthal mode is not admitted into the nozzle with the center–body present (see Section 5.2.1.1).

Figures 5.39 and 5.40 show the radial variation of power spectra at x/D_h=0.68 for S=0.28, Q=50 SCFM. Except, behind the center–body the spectra for the entire radial extent of the flow field at x/D_h=0.68 are very similar. The large difference in time scales observed for the S=0 case across the outer shear layer is not observed

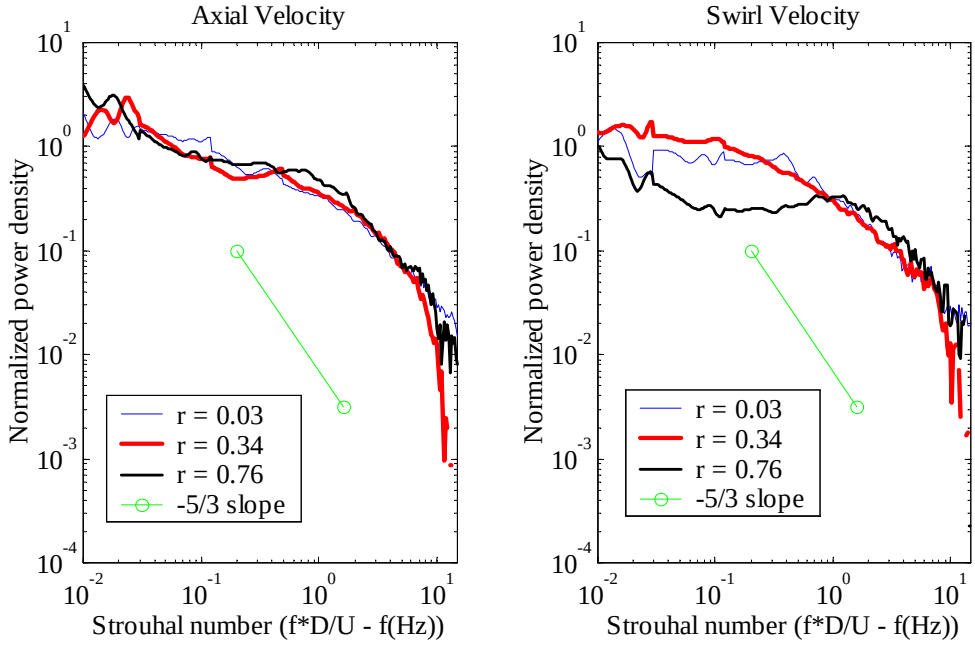

Figure 5.37: Radial comparison of power spectra at x/D_h=0.68 for S=0, Q=50 SCFM (inner flow field)

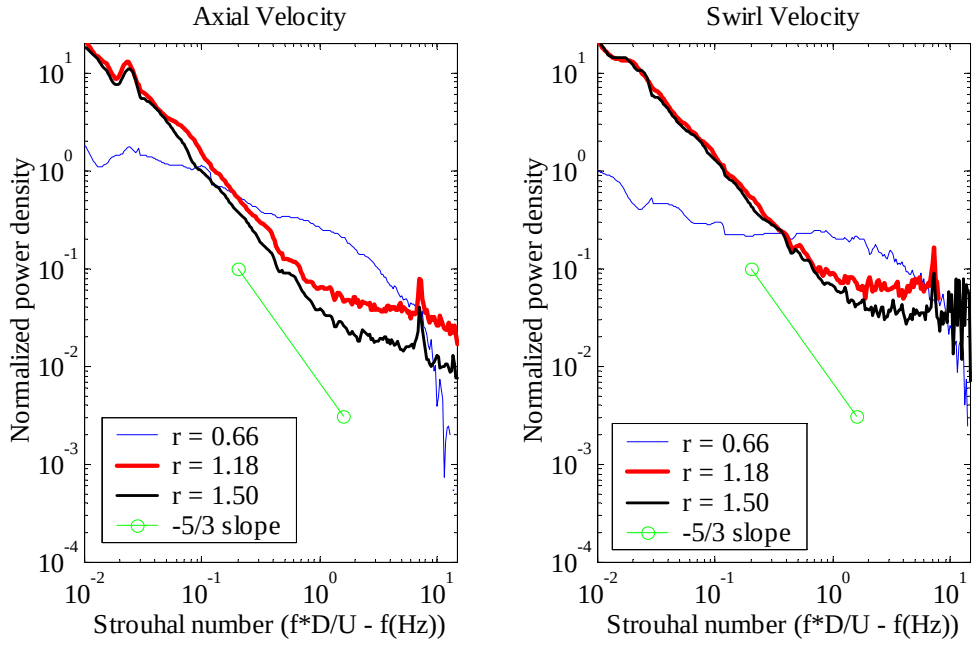

Figure 5.38: Radial comparison of power spectra at x/D_h=0.68 for S=0, Q=50 SCFM (outer flow field)

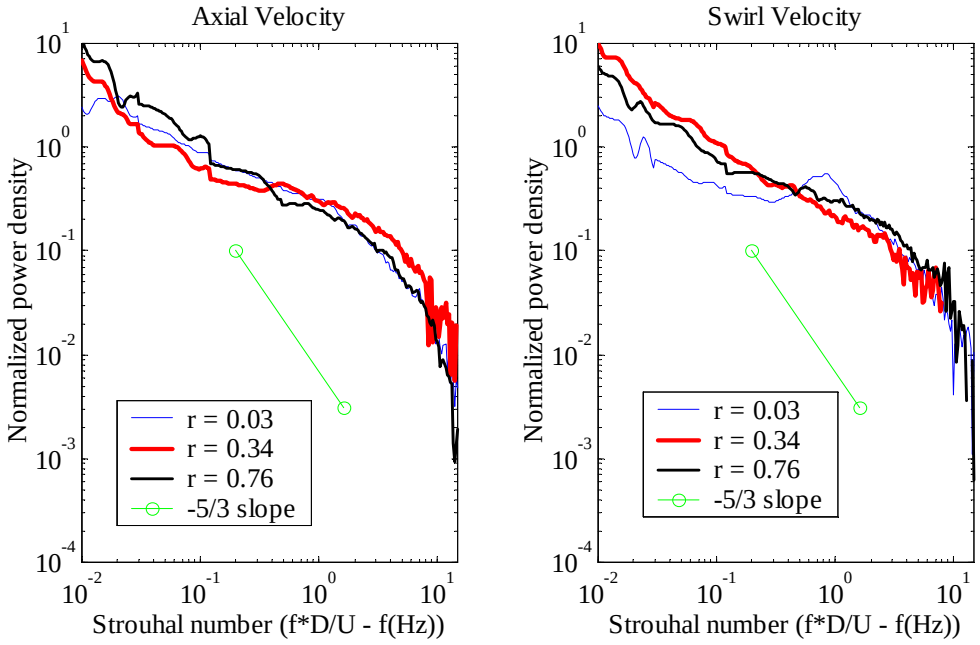

Figure 5.39: Radial comparison of power spectra at x/D_h=0.68 for S=0.28, Q=50 SCFM (inner flow field)

here. The fact that the spectra beyond the outer shear layer remain similar to the spectra of the inner flow can be related to the fact that although the axial velocity has decreased significantly in the outer shear layer, significant swirl velocity remains. The presence of swirl introduces shear into the flow which causes turbulence production in this area of the flow field. It should also be noted that the outer shear layer spectra contain a small bulge in energy as observed previously in several flow fields around St=3.

The spectrum of swirl velocities has a small local maximum around St=0.8. The peak is not observed for the axial velocity fluctuations but this is not surprising, considering that axial RMS velocity fluctuations have a local minimum in the center of the flow field. The Strouhal number of St=0.8 can be related to a Strouhal number of 0.42 based on the center–body diameter. This Strouhal number is in the range where vortex shedding is frequently observed. The development of the wake dynamics will be followed downstream (see Figure 5.43).

Figures 5.41 and 5.42 show the radial variation of velocity power spectra for

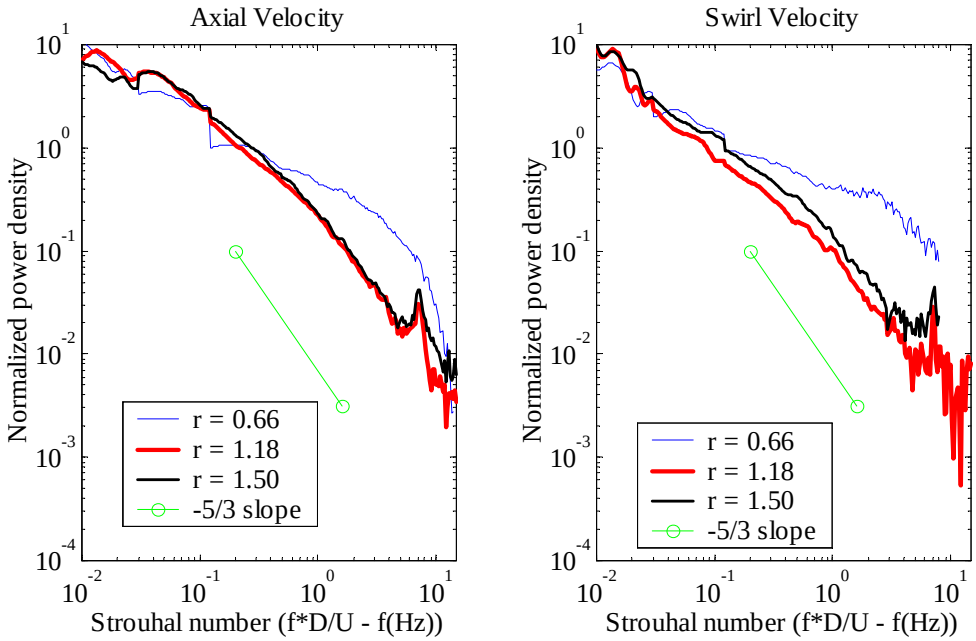

Figure 5.40: Radial comparison of power spectra at x/D_h=0.68 for S=0.28, Q=50 SCFM (outer flow field)

x/D_h=0.68, S=0.60 and Q=50 SCFM. The inner flow power spectra are dominated by the large instability observed also in the nozzle. The strength of the oscillations appears to be greater at this axial location than in the nozzle. Beyond the outer shear layer however, evidence of the instability disappears quickly from the spectra. It is interesting to note that the axial velocity spectrum immediately behind the nozzle shows almost no trace of the instability, while the instability oscillations in the swirl velocity are very strong. For S=0.29, similar behavior was observed. See Section 5.3 for a comprehensive analysis of the instability.

Figures 5.43 and 5.44 show radial variation of velocity spectra for x/D_h=1.47, S=0.28, Q=50 SCFM. The inner and outer parts of the flow are starting to look very similar. Both inner and outer flows exhibit a large amount of low frequency energy. In the center of flow, some leveling out of the spectra indicates continued turbulence production. Near St=0.4 some concentration of spectral energy can be observed for r less than 0.5. Figure 4.51 of Chapter 4 shows that the axial velocity peaks at r/D_h=0.5. The spectral peak is thus due to inner shear layer dynamics. The spectral

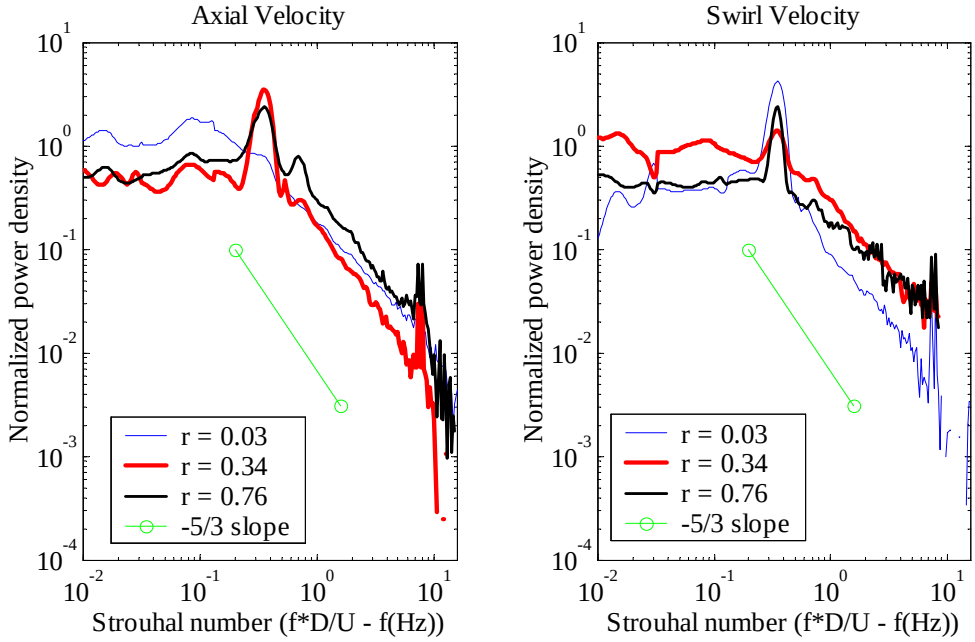

Figure 5.41: Radial comparison of power spectra at x/D_h=0.68 for S=0.6, Q=50 SCFM (inner flow field)

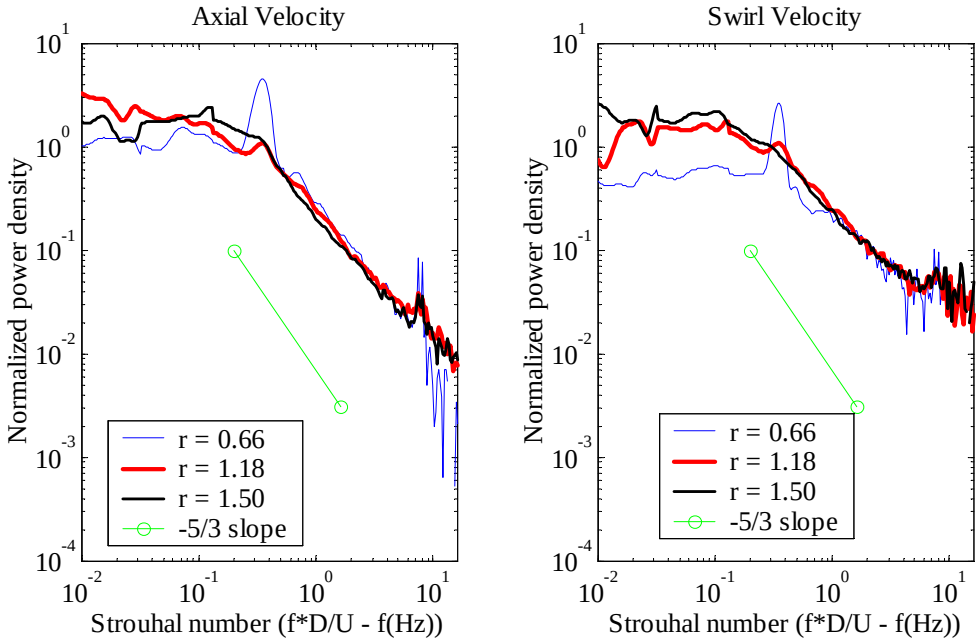

Figure 5.42: Radial comparison of power spectra at x/D_h=0.68 for S=0.6, Q=50 SCFM (outer flow field)

peak observed in the center of the flow field for x/D_h=0.68, was observed at St=0.8.

The approximate 2 to 1 relationship between the frequency peak at x/D_h=0.68 and x/D_h=1.47 can be seen as evidence for vortex merging, although the frequency peak is relatively weak. An alternative view has to do with the evolving linear stability characteristics of the flow field. At the base of the shear layer, a wide range of Strouhal numbers is amplified. As the flow evolves downstream, the shear layer grows and the band of amplified frequencies decreases and shifts downward in frequency. At each axial station, a spectral peak is seen at the frequency that has the highest integrated energy growth over the entire range of flow development to that point. As the shear layer thickens, the amplification rates decrease, the bandwidth of amplified Strouhal numbers decreases and the range of amplified Strouhal numbers shifts to lower Strouhal numbers. Chapter 6 will examine the stability of the wake flow behind the center–body. For very rapid shear layer development, the spectral energy amplification may be so smeared that it is difficult to distinguish from random, turbulence induced energy production. The dynamics observed here will be discussed in greater detail in Section 5.3.3.

Figures 5.45 and 5.46 show the radial variation of velocity spectra for x/D_h=1.47, S=0.29 and Q=100 SCFM. The spectra are in general very similar to the lower flow rate spectra. Several differences are however worth pointing out. The spectral peaks around St=0.4 are stronger here and the peak frequency seems to drift somewhat with radial location. Another feature is the extremely large amount of low frequency energy, especially at r/D_h=0.34. The y-scale of the plot had to be expanded significantly to capture the amount of energy. The y-intercept is proportional to the integral time scale. The cause for the very high low frequency energy is a type of intermittency that was found in this flow field at both the lower and higher flow rates. The associated structures and further details are described in Section 5.3.3.

Figures 5.47 and 5.48 show the radial variation of spectra for x/D_h=1.47, S=0.60 and Q=50 SCFM. The instability observed upstream is still visible here although in much weaker form. The instability is strongest in the axial velocity fluctuations and can barely be distinguished in the swirl velocity spectra. Evidence of the instability

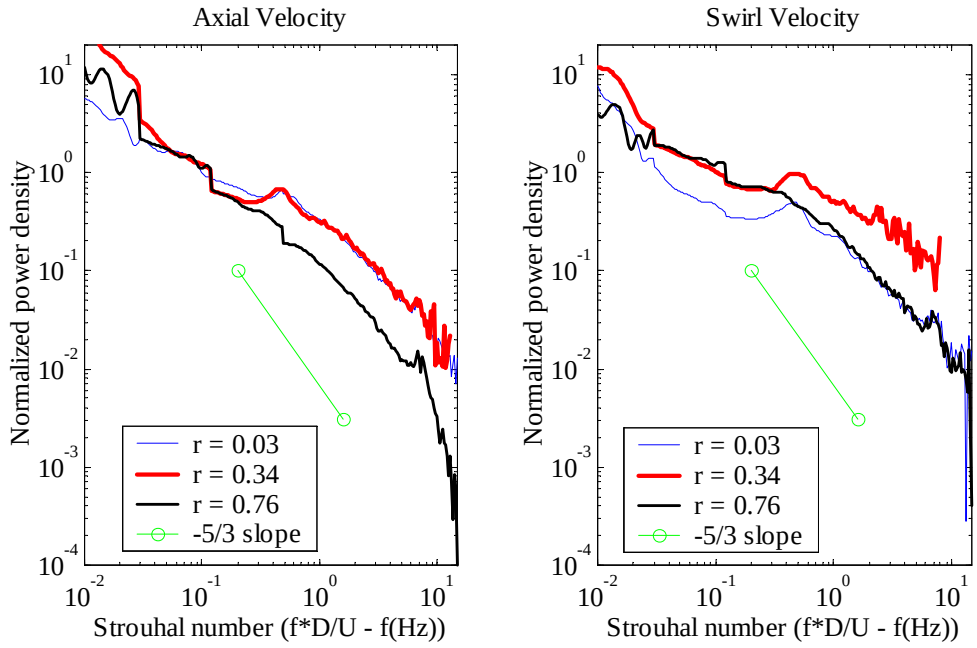

Figure 5.43: Radial comparison of power spectra at x/D_h=1.47 for S=0.28, Q=50 SCFM (inner flow field)

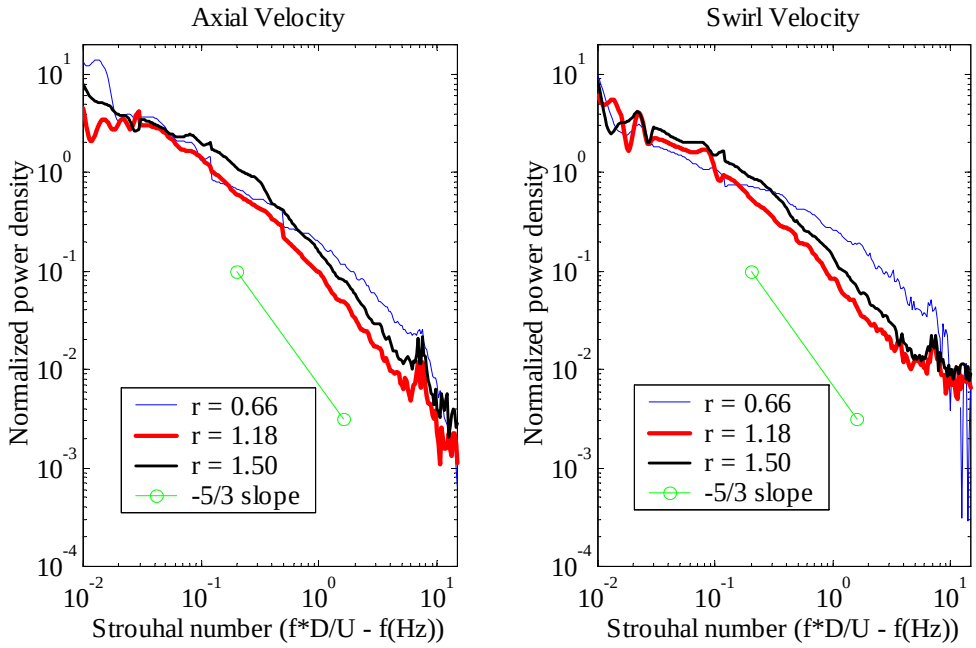

Figure 5.44: Radial comparison of power spectra at x/D_h=1.47 for S=0.28, Q=50 SCFM (outer flow field)

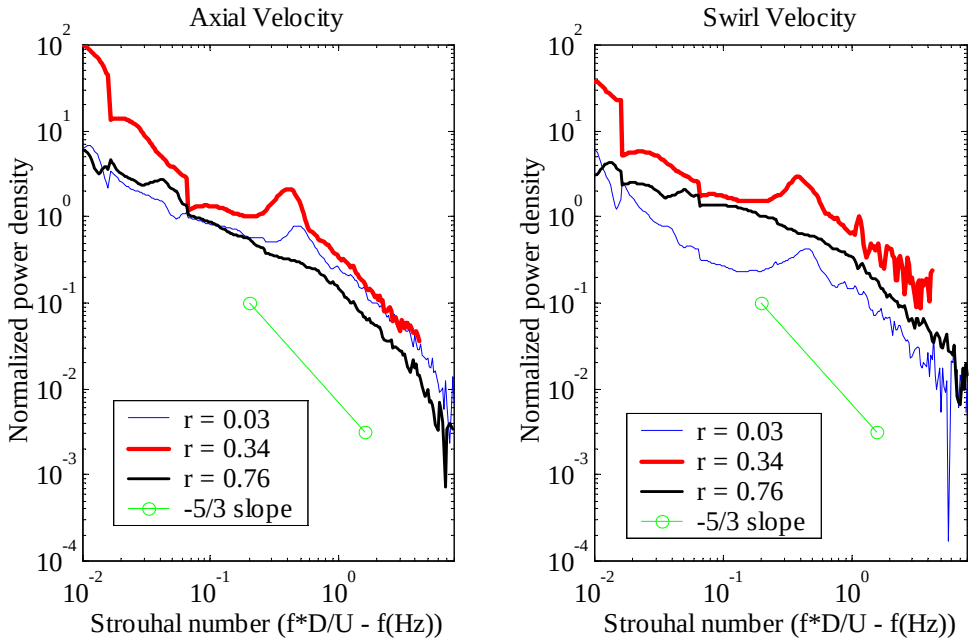

Figure 5.45: Radial comparison of power spectra at x/D_h=1.47 for S=0.29, Q=100 SCFM (inner flow field)

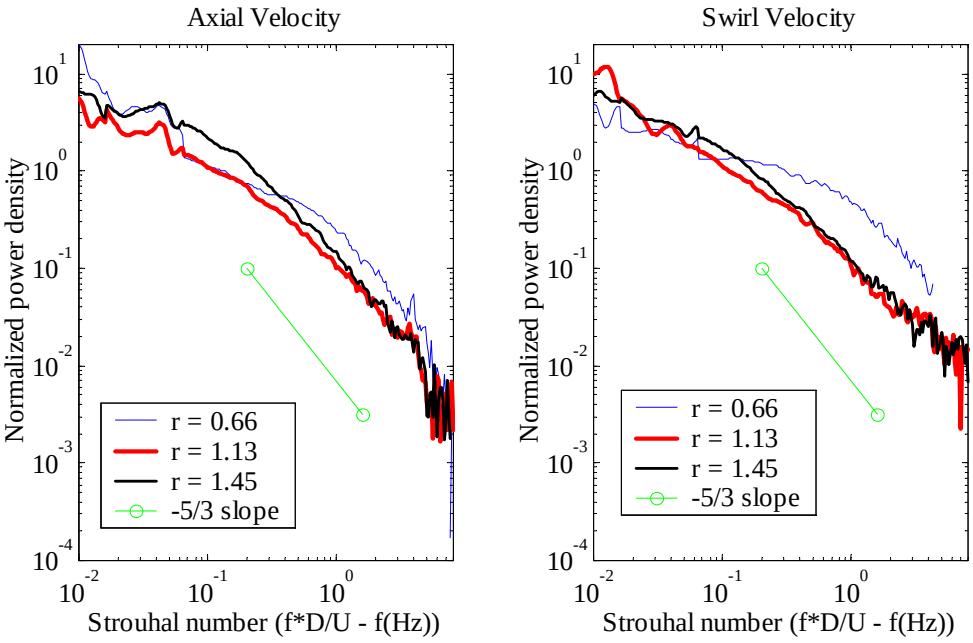

Figure 5.46: Radial comparison of power spectra at x/D_h=1.47 for S=0.29, Q=100 SCFM (outer flow field)

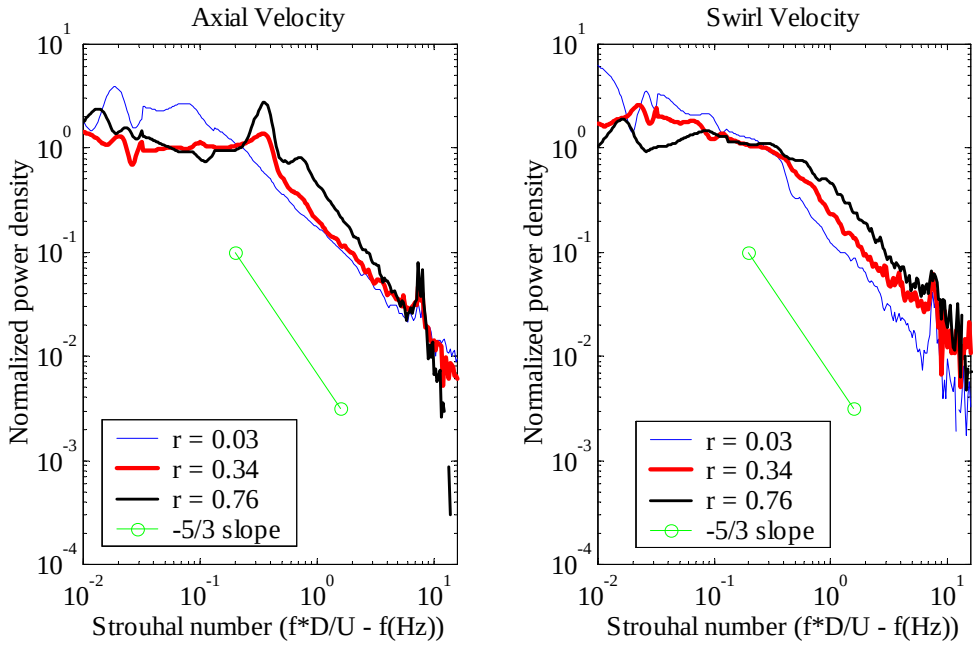

Figure 5.47: Radial comparison of power spectra at x/D_h=1.47 for S=0.60, Q=50 SCFM (inner flow field)

can no longer be seen at the center of the flow. Overall the spectra are very similar and especially compared with the S=0.28(0.29) case, a relatively small amount of low frequency energy is present in the flow.

Figures 5.49 and 5.50 show the results for the same swirl number and axial location as Figures 5.47 and 5.48 except at the higher flow rate of 100 SCFM. The traces of the instability are stronger at the higher flow rate, and can be easily distinguished in both the axial and swirl velocity spectra. Similar to the lower flow rate, evidence of the instability is weakest at the very center of the flow and in the outermost areas of the flow field. Swirl velocity fluctuation integral timescales are a decreasing function of radius in the inner portion of the flow field. The trend may also be related to the presence of the instability just outside the inner core of the flow field.

Figure 5.51 shows the power spectra of velocity at three radial locations for x/D_h=4.79, S=0 and Q=50 SCFM. Both axial and swirl velocity spectra exhibit a small local maximum in energy near St=0.3, likely due to the developing jet and associated shear layer. In the outer part of the flow field, large scales contain a

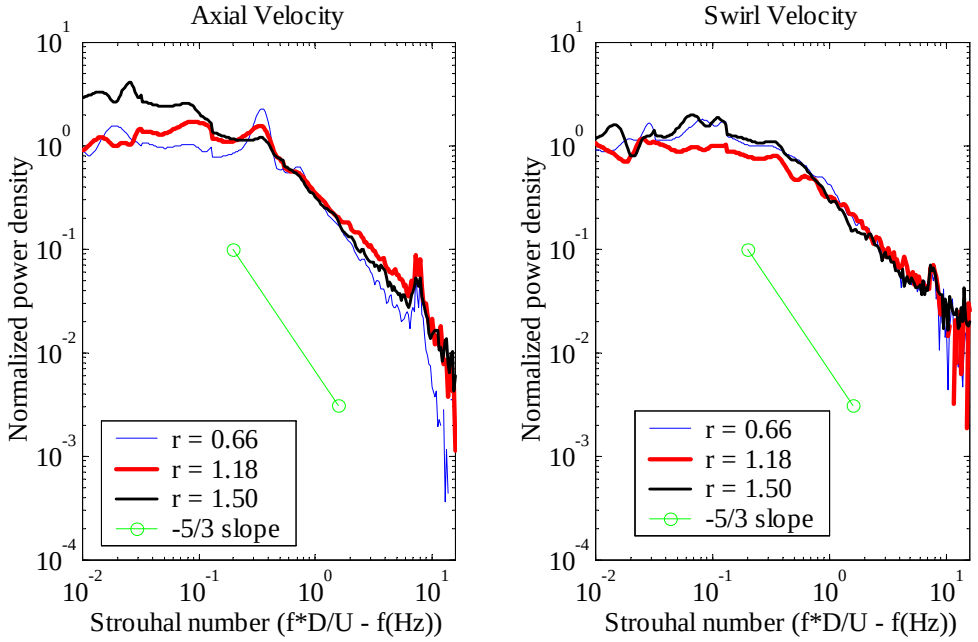

Figure 5.48: Radial comparison of power spectra at x/D_h=1.47 for S=0.60, Q=50 SCFM (outer flow field)

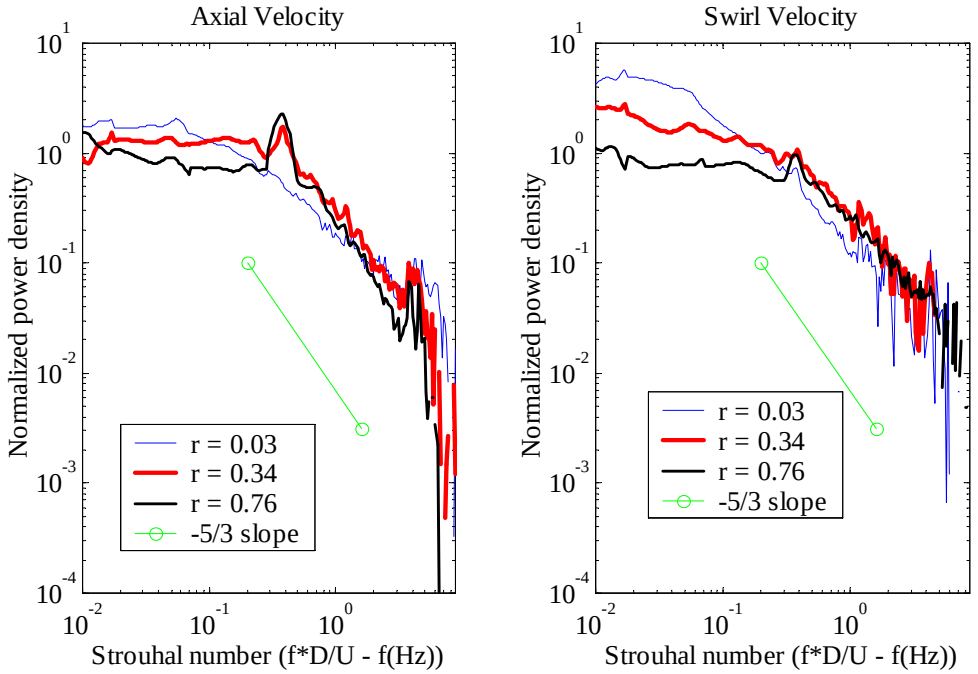

Figure 5.49: Radial comparison of power spectra at x/D_h=1.47 for S=0.60, Q=100 SCFM (inner flow field)

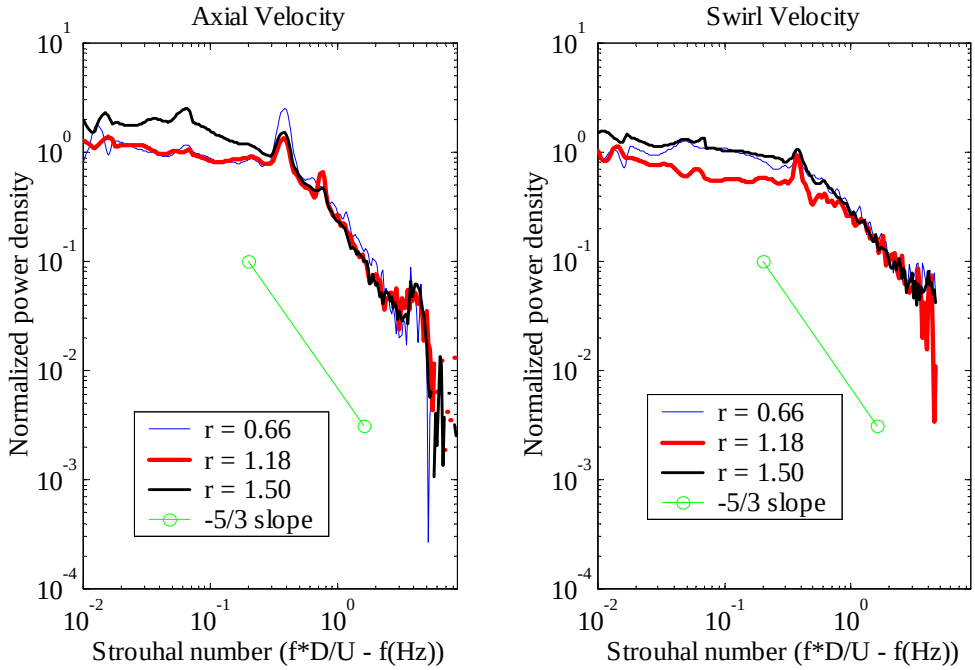

Figure 5.50: Radial comparison of power spectra at x/D_h=1.47 for S=0.60, Q=50 SCFM (outer flow field)

significant amount of energy. The spectrum of velocities here is similar to that all throughout the flow outside the outer shear layer for the S=0 case, for example Figure 5.38. The integral time scales are nearly equal in the center and outer parts of the flow. In between, the results suggest that the integral time scale of velocity fluctuations is greater than the integral time scale of swirl velocity fluctuations. This was observed above in Section 5.2.1.2 for S=0.12 at Q=50 SCFM.

Figure 5.52 shows the radial variation of velocity spectra for x/D_h=4.79, S=0.28 and Q=50 SCFM. The spectra reflect the advanced stage of development of the flow. The long linear cascade of energy is similar to that observed in the free vortex geometry for the non-zero swirl cases at the same physical measurement location (Section 5.2.1.2). The tail of energy at the very bottom of the spectrum is not physical and shows the influence of an inadequate sampling rate that is slower than for the other cases studied. At the last two axial stations a conscious effort was made (in non-zero swirl cases with high turbulence) to reduce the mean sampling frequency

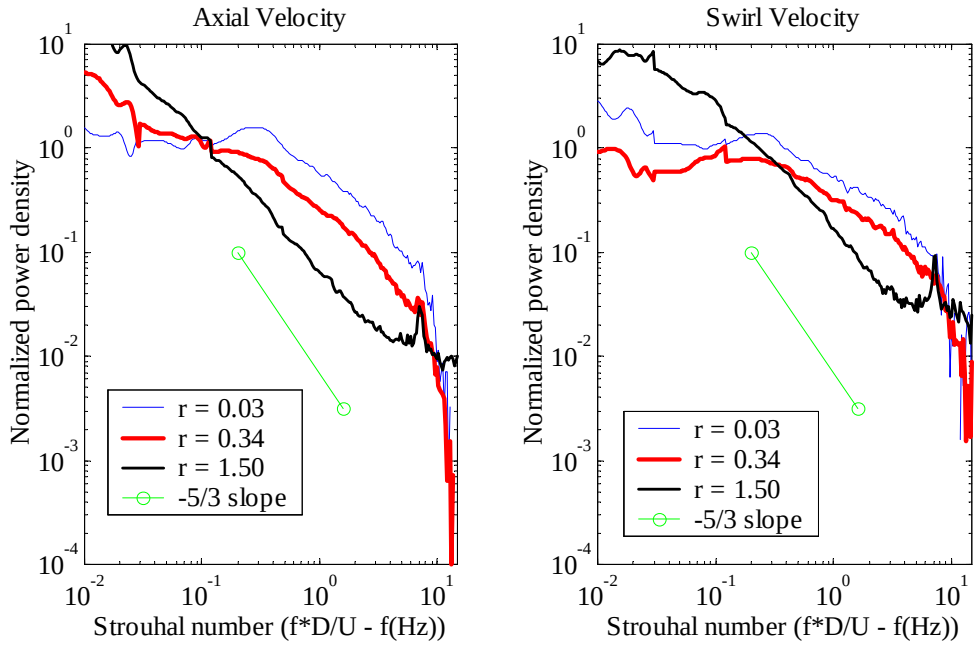

Figure 5.51: Radial comparison of spectra at x/D_h=4.79 for S=0, Q=50 SCFM

in order to increase the time over which statistics and spectra are calculated.

Figure 5.52 shows the radial variation of velocity spectra for x/D_h=4.79, S=0.60 and Q=50 SCFM. Similar to the S=0.28 case, the spectra exhibit a tail due to a lower average mean sampling frequency. In contrast to the S=0.28 case, much less low frequency energy is found in the flow and the spectra level off below St=0.1. The lack of low frequency energy can be associated with the instability. The presence of the instability converts mean flow momentum into energy concentrated at St=0.4, from there the dominant portion of energy is transferred to smaller scales. The instability energy is dissipated very efficiently by the flow field and at x/D_h=4.79 the S=0.60 case exhibits a relatively low RMS velocity (about half of the S=0.28) case (see Figure 4.57). The lower turbulent energy present in the flow results in shorter integral time scales of turbulence. Additionally, in the outer part of the flow, where a weak wall jet still exists, the time scales are further reduced from the values at the centerline.

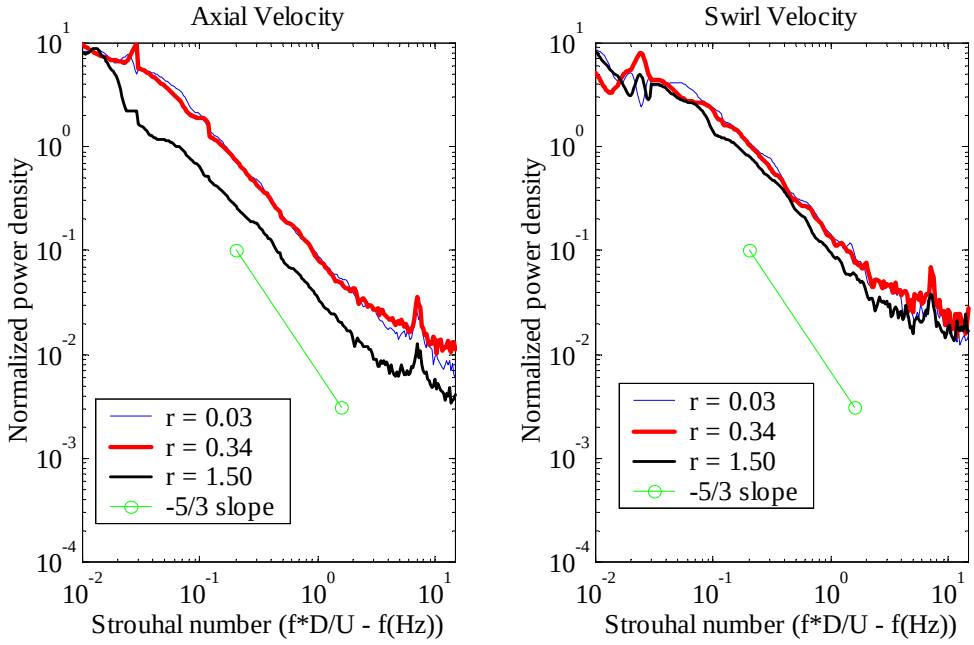

Figure 5.52: Radial comparison of spectra at x/D_h=4.79 for S=0.28, Q=50 SCFM

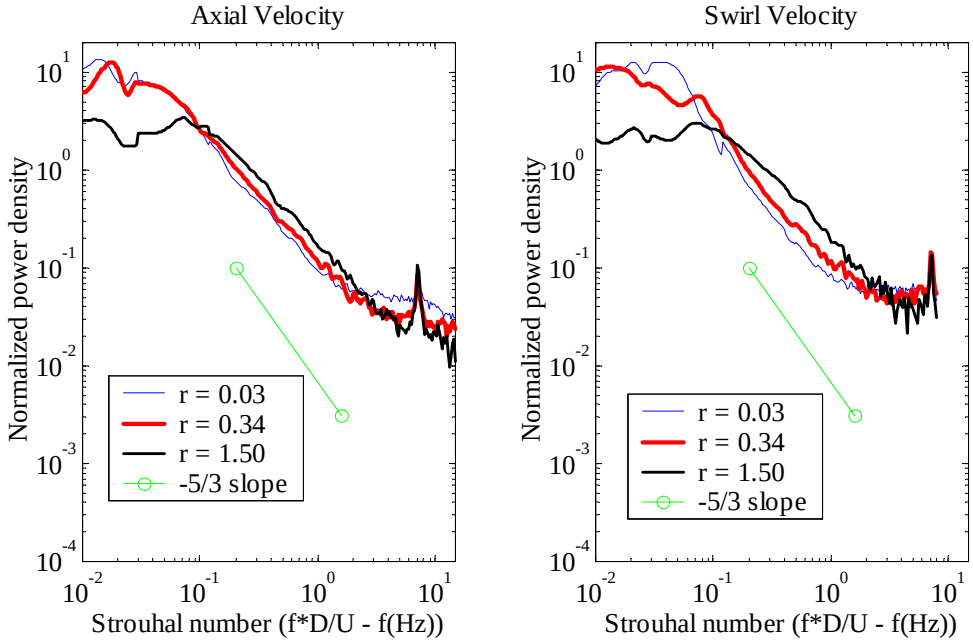

Figure 5.53: Radial comparison of spectra at x/D_h=4.79 for S=0.60, Q=50 SCFM

5.3 Details of selected flow dynamics

The dynamics observed above in Section 5.2 have many similarities but under some conditions, especially noteworthy dynamic pictures were discovered and deserve further study. The following paragraphs discuss these conditions in more detail and attempt to shed light on their origin.

5.3.1 Free vortex geometry flow without swirl

Perhaps the most familiar of the dynamic features to be highlighted in the present section is the apparent jet shear layer instability observed in the free vortex geometry without swirl. The axial development of the power spectrum near the centerline of the flow is shown in Figure 5.54. The power spectra in this case have not been normalized by the local variance of the velocity. The figure shows that the broadband peak around St=0.4 grows in magnitude downstream at the same time as the energy overall frequencies is increasing. The plot clearly shows that although some concentrated turbulence production is occurring around St=0.4, the production is by no means limited to this frequency range.

In Section 5.2.1.2, the peak near St=0.4 was seen to disappear in the outer shear layer. If the peak near St=0.4 truly is associated with a shear layer instability then the peak oscillation magnitude is expected inside the shear layer, not at the center of the flow where it appears most visible. Figure 5.55 shows the power spectra of three adjacent radial data points at x/D_n=1.48. The plot clearly shows how both the energy around St=0.4 and the surrounding energy grow as the measurement location is moved into the shear layer from the center of the flow. The visibility of the St=0.4 energy decreases dramatically however and almost no trace of it remains at r/D_n=0.40. Neither Figure 5.54 nor Figure 5.55 show a significant concentration of spectral energy around St=0.4 in the swirl velocity fluctuations. The lack of visibility is attributable to two main factors. The first is that the coherent oscillations in the azimuthal direction associated with a shear layer instability are relatively weaker (see Section 6.7). The second factor is that the background fluctuation energy in the swirl

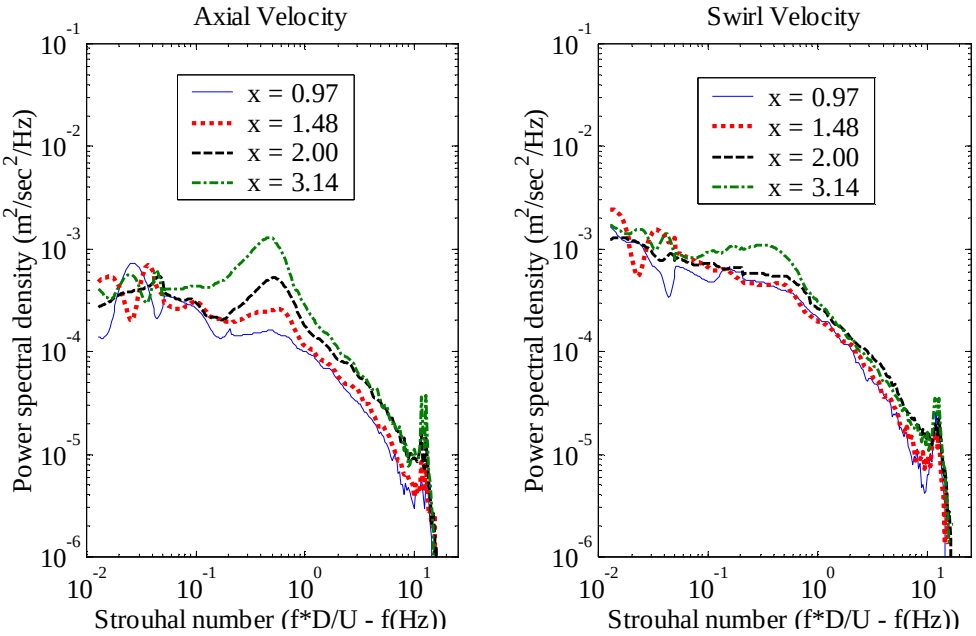

Figure 5.54: Axial development of St=0.4 instability at the center of the flow field r/D_n=0, Q=50 SCFM

velocity component is higher than that in the axial velocity component in the inner parts of the flow field thus masking a possible concentration of energy around St=0.4.

To obtain a measure of the radial distribution of the St=0.40 energy, a peak search in the combustor section spectra was performed. If a peak was found, an estimate of the amplitude was obtained by taking the peak and subtracting an estimate of the background energy. If no peak was found, the amplitude was set to zero. Figure 5.56 shows the radial distribution of the St=0.40 amplitudes at all axial locations measured. The figure shows that as the shear layer is approached, the peak loses visibility and the amplitudes are calculated to be zero. As long as the peak remains visible however, it shows a an increase towards the shear layer, as expected. The radial extent over which the peak is visible is largest upstream and decreases with increasing distance downstream. The visibility is decreasing due to the spreading of the turbulence energy from the center of the shear layer to the inner part of the flow field. Note that the St=0.4 peak is barely visible at all at the first axial location measured. This indicates that the energy at St=0.4 also requires some axial distance

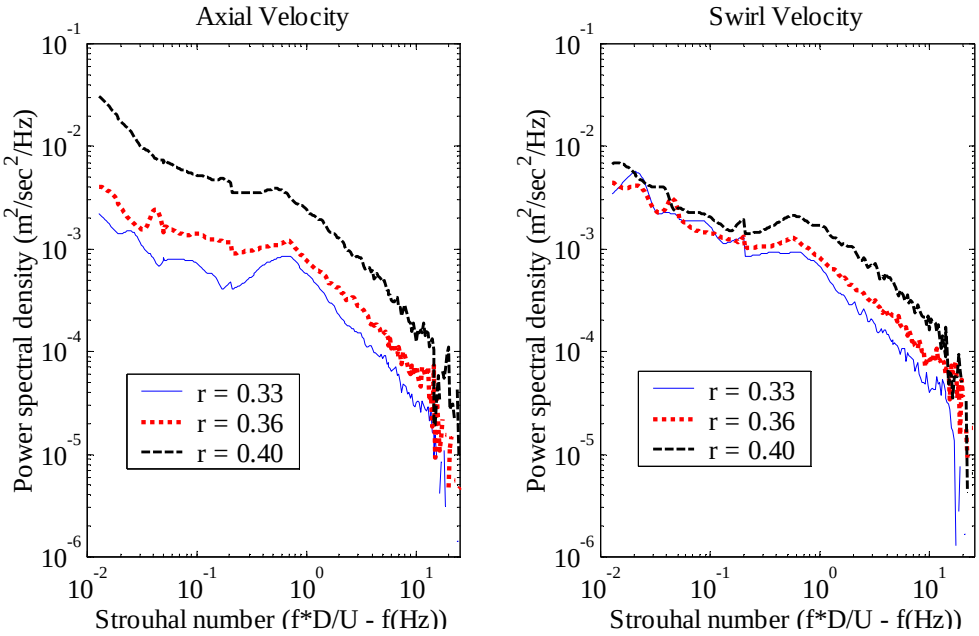

Figure 5.55: Radial "cut-off" of St=0.4 instability, x/D_n=1.48, Q=50 SCFM

to generate enough energy in the center of the flow to become visible against the background turbulence.

The main point to be made here regarding flow development is that although the flow is relatively efficient at producing broadband turbulence, the energy produced stays local to the shear layer for a relatively long period of time. The St=0.4 energy however appears relatively quickly at the center of the flow field and therefore is most visible here. From a mixing point of view, the apparent instability is a much more efficient mechanism of transport of momentum than the broadband localized shear layer turbulence production.

To further describe the axial growth of the energy around St=0.4, Figure 5.57 plots the amplitude of the St=0.4 peak as a function of the axial coordinate near the center of the flow. The plot shows that the rate of energy gain increases slightly and then remains linear. Linear growth in energy means that the linear amplitude of the associated wave is growing only as the square root of the axial coordinate. The lower than exponential growth is expected in this part of the flow field, as shown in Cohen and Wygnanski (1987b). Exponential growth only occurs in the initial part of flow

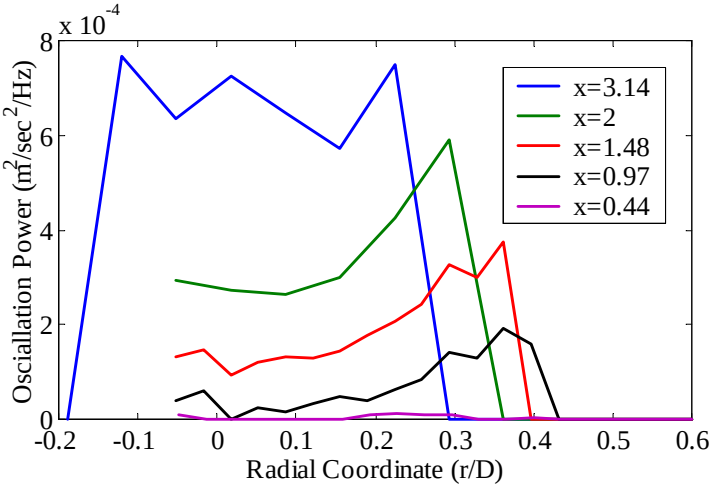

Figure 5.56: Radial profiles of instability energy for several axial locations, Q=50 SCFM, St=0.4

development up to about x/D = 0.5, an area of the flow field largely inaccessible in the present experimental setup. Beyond x/D = 0.5 growth slows considerably. The main reason for slower growth is the non-parallel character of the flow field which changes the local amplification rate (Wygnanski and Petersen, 1987).

Figures 5.58 and 5.59 show histograms and time histories of velocities respectively at the centerline of the flow field at the last axial station measured. A relatively significant amount of energy is contained in the broadband St=0.4 peak at this location. However, the histograms for both velocity components appear near gaussian. The

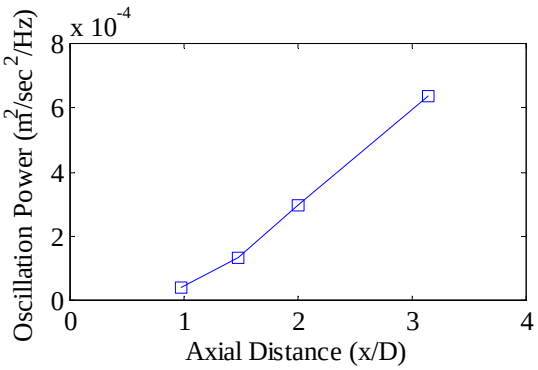

Figure 5.57: Axial development of instability energy, Q=50 SCFM, St=0.4

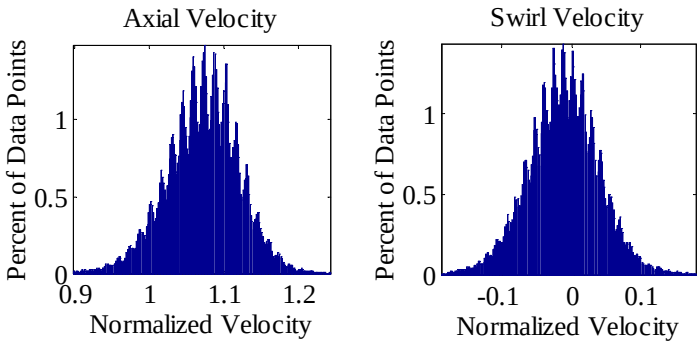

Figure 5.58: Histogram of velocities, r/D_n=0.02, x/D_n=3.14, Q=50 SCFM

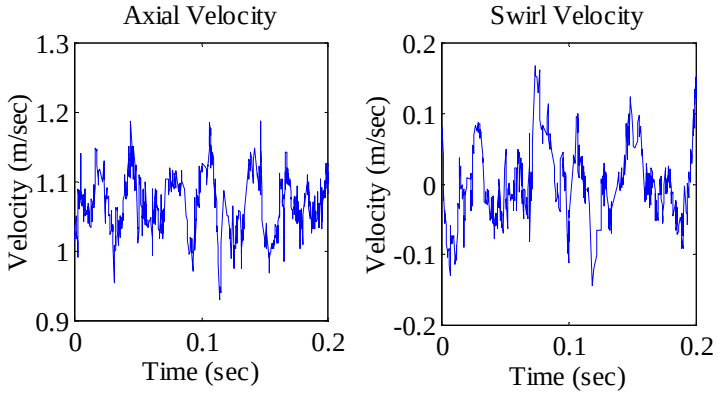

Figure 5.59: Time history of velocities, r/D_n=0.02, x/D_n=3.14, Q=50 SCFM

St=0.4 energy peak is too broadly distributed in frequency to generate the bi-modal distribution that would be observed for velocity data with significant periodic content. The sample time history of axial velocity fluctuations shown in Figure 5.59 shows more evidence of coherent fluctuations. The period of the relatively noisy oscillation, is near the expected frequency of approximately 40 Hz. It is clear from these plots though that the background turbulence modulates the main oscillation and interacts with it. The turbulence is not merely superimposed on the oscillation.

Although the dynamics observed around St=0.4 for the zero swirl case are not very spectacular, they do lend significant insight into how flows with significant input turbulence exhibit traces of convective instability. In the presence of significant inlet turbulence, the action of the instability may be masked by broadband turbulence pro-

duction in some areas of the flow but visible in other parts. Visibility of concentrated spectral energy does not imply that the origin of the concentrated spectral energy is near. The actual amplitude distribution of the energy must be determined in order to make an assessment on the origin. In the present flow, the instability is most visible in the center of the flow but clearly originates in the outer shear layer, where it is however masked by concurrent broad band turbulence production.

The introduction of swirl adds shear to the center of the flow field and hence turbulence production. It is likely that convective instabilities are still active when swirl is present but that their effect is masked by efficient swirl induced turbulence production in conjunction with broadband turbulence production in the outer shear layer.

5.3.2 Annulus geometry oscillations at higher swirl numbers

Compared to the dynamics of the jet flow just described, the dynamics observed at S=0.60 in the annulus geometry are of much larger scale. Large narrow band spectral peaks are observed in the initial development region of the flow field. The associated mean velocity field exhibits a ring jet with a large central recirculation zone. Although both axial and swirl velocity fluctuations show evidence of the apparent flow instability, the distribution of oscillation amplitudes shown in Figure 5.60 differs significantly between the two velocity components. The amplitude distribution very clearly shows the existence of nodes along the radial direction where the instability is essentially absent. The axial oscillation amplitude has nodes at the flow center, at around r/D_h=0.75 and just beyond r/D_h=1. The swirl oscillation amplitude distribution only has one clear node at r/D_h=0.25. The instability is not visible in the axial or swirl velocity fluctuations in the outer recirculation zone.

As the flow develops downstream, the axial velocity oscillation magnitude first increases and then decreases. The swirl oscillation magnitude decreases. The nodes of the distributions remain visible downstream and are stationary in radial location except for the off-centerline nodes of the axial velocity amplitude distribution. These nodes move outward. Figure 5.61 shows the axial development of velocity profiles for

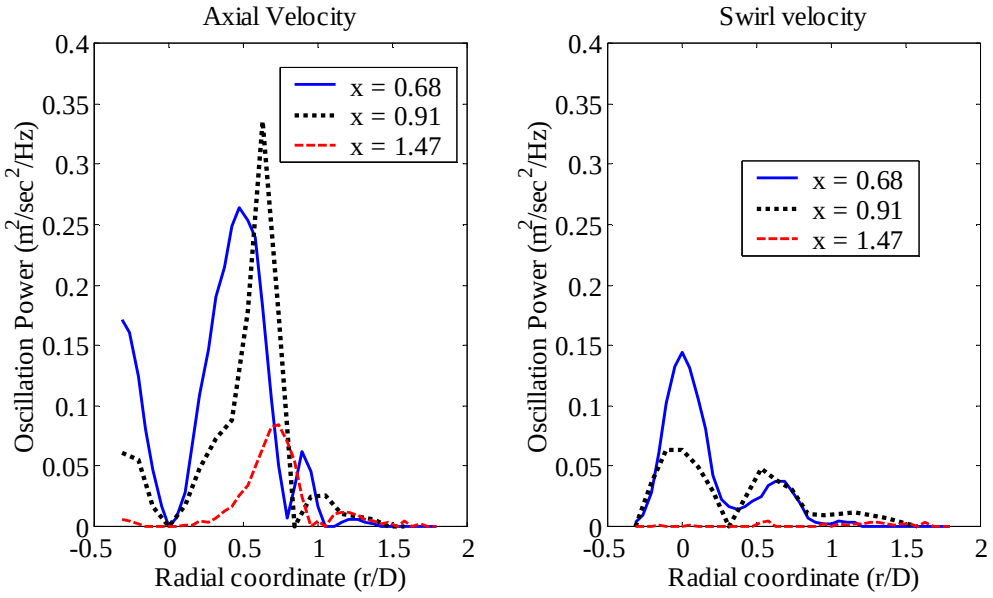

Figure 5.60: Radial distribution of oscillation magnitude for S=0.6 and Q=50 SCFM

the condition currently discussed. The figure reveals that the movement of the axial oscillation amplitude nodes matches the change in radial location of the inner and outer shear layer of the ring jet. Similarly, the swirl velocity does not exhibit a shift in shear layer location and the nodes are seen to remain stationary. Furthermore, note that the shear in the swirling flow field at x/D_h=1.48 is significantly lower than at the other two axial locations and the instability is barely able to be detected in the swirl velocity oscillations.

The instability is thus closely related to the shear in the axial and swirl velocity profiles. The striking part about this flow shear related instability is how narrow the spectral energy distribution is. As observed for the non-swirling jet above, the flow is expected to amplify disturbances over some relatively broad range of frequencies. The narrow–band behavior seen here can usually only be obtained by adding external excitation to the flow, either artificially using a speaker or naturally, using the feedback provided by an acoustic mode. To help show that the excitation in this case is internal, i.e. the flow is self excited, the experimental conditions were varied from the starting point of S=0.6 and Q=50 SCFM. In Section 5.2.2.2 it was already seen

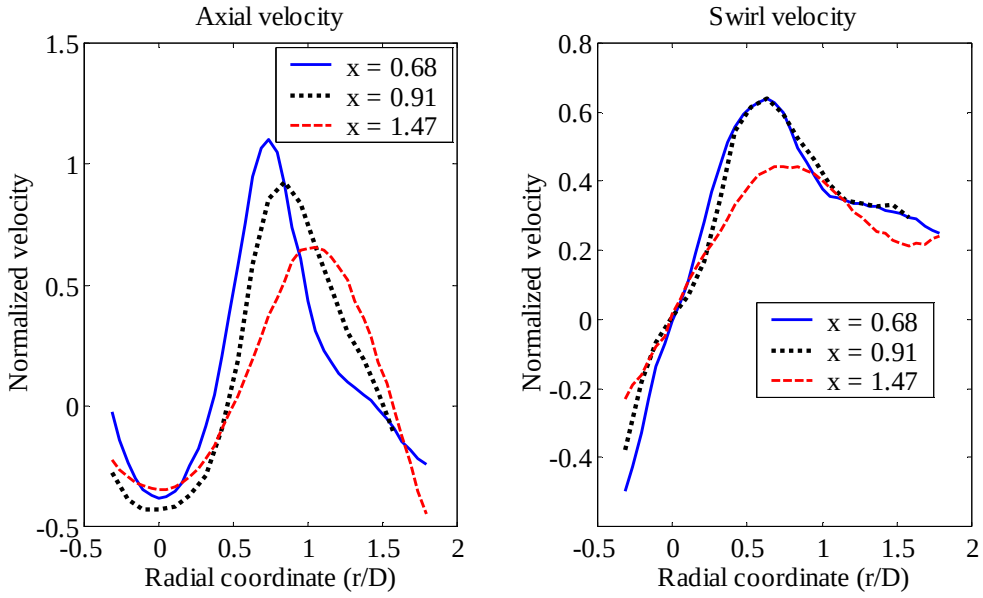

Figure 5.61: Velocity profiles for S=0.6 and Q=50 SCFM

that the frequency appears to scale linearly with flow rate.

Experiments using the custom microphone transducers were performed over a wide range of flow rate at the same swirl angle setting as for S=0.60. The resulting frequency dependence is shown in Figure 5.62. The frequencies vary linearly over the entire range of flow rates. The microphones used in the study were located immediately downstream of the sudden expansion. Microphones further downstream did not register the flow oscillation frequency. The fact that downstream microphones did not register the flow oscillation gives further support to the idea that the oscillation observed is a self excited flow oscillation, as would be expected from an absolutely unstable flow. Chapter 6, in particular Section 6.7 will investigate the absolute stability characteristics of the mean flow field underlying the self–excited velocity oscillations.

In order to connect the dynamics observed at S=0.60 to those observed at S=0.30, additional measurements were performed in a range of swirl numbers between 0.18 and 0.91, keeping the flow rate constant at a nominal 50 SCFM. The variation of the instability frequency with swirl number is shown in Figure 5.63. The variation

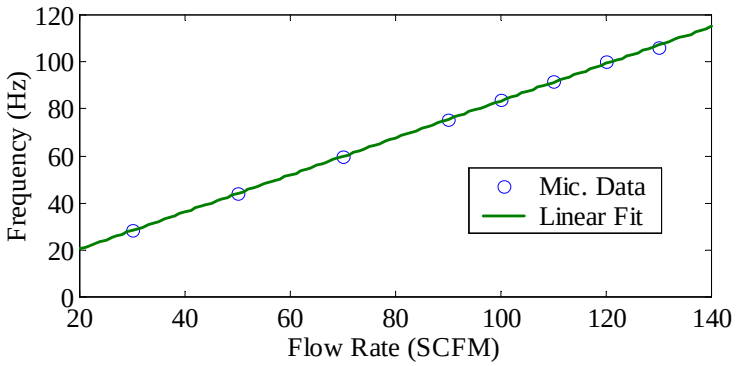

Figure 5.62: Instability frequency vs. flow rate for S=0.60

of frequency is close to linear. Below S=0.35 however, the instability is no longer visible.

Figure 5.64 shows the radial distribution of the oscillation magnitude for several swirl numbers. The figure shows that for all swirl numbers the shape of the distribution is relatively constant. The magnitude of the oscillation however rapidly decreases between S=0.42 and S=0.36 and is known to be absent for S = 0.30. A significant outward shift of the distribution is observed as the swirl number increases above 0.60.

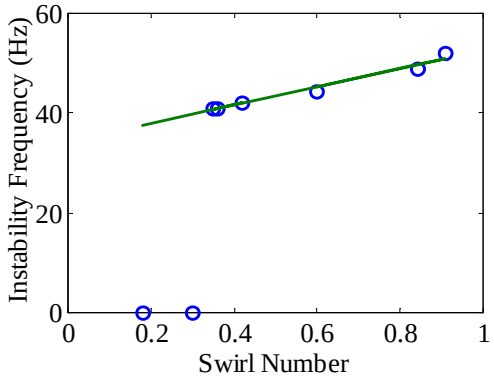

Figure 5.63: Instability frequency vs. swirl number for Q=50 SCFM

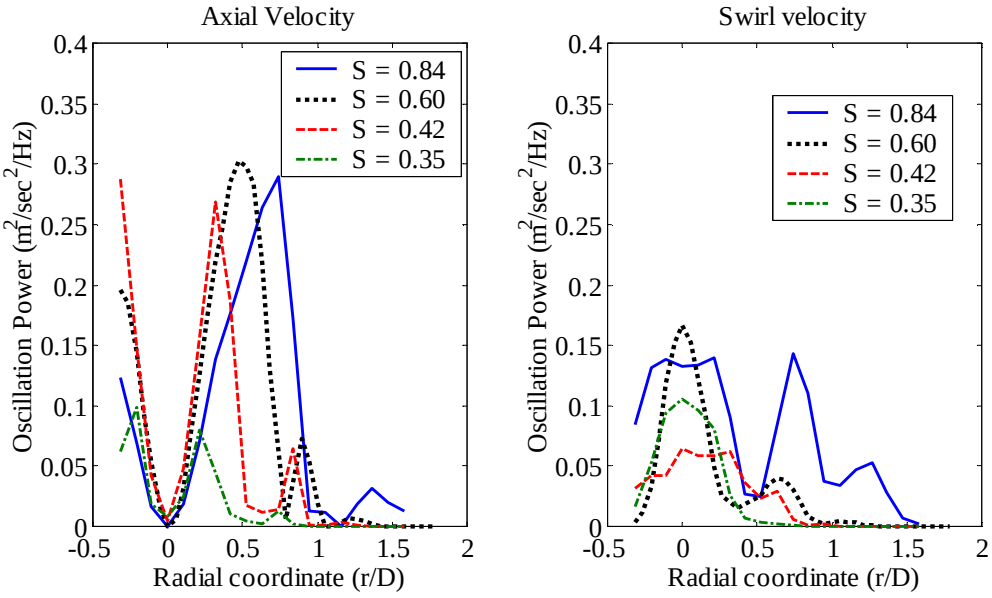

Figure 5.64: Radial distribution of oscillation magnitude for several swirl numbers at x/D_h=0.68, Q=50 SCFM

The S=0.84 case shows very clearly that there is a second interior instability node. At the other swirl levels, the node is either absent or very faint.

The velocity profiles corresponding to Figure 5.64 are shown in Figure 5.65. In comparing the two figures it is once again clear that the oscillation peaks correspond closely with the inner and outer shear layers. The strong outward shift of the swirl velocity profile at S=0.84 is very noticeable. The accompanying increased width of the central shear shear layer is reflected in a wider oscillation distribution peak at the center of the flow. The axial velocity profiles show that reverse flow is covering a significant part of the inlet at S=0.84. Indeed, even the nozzle velocity profile at x/D_h=-0.53 shows some signs of reverse flow reaching into the nozzle section. The result of flow detaching from the inner center–body is an accelerated consumption of azimuthal momentum in this zone, leading to the increased thickness in the central shear layer observed in the combustor section swirl velocity profile.

Figures 5.66 and 5.67 show velocity time histories and histograms respectively at r/D_h=0.5, x/D_h=0.68 for S=0.6, Q=50 SCFM. The sample time histories shown in

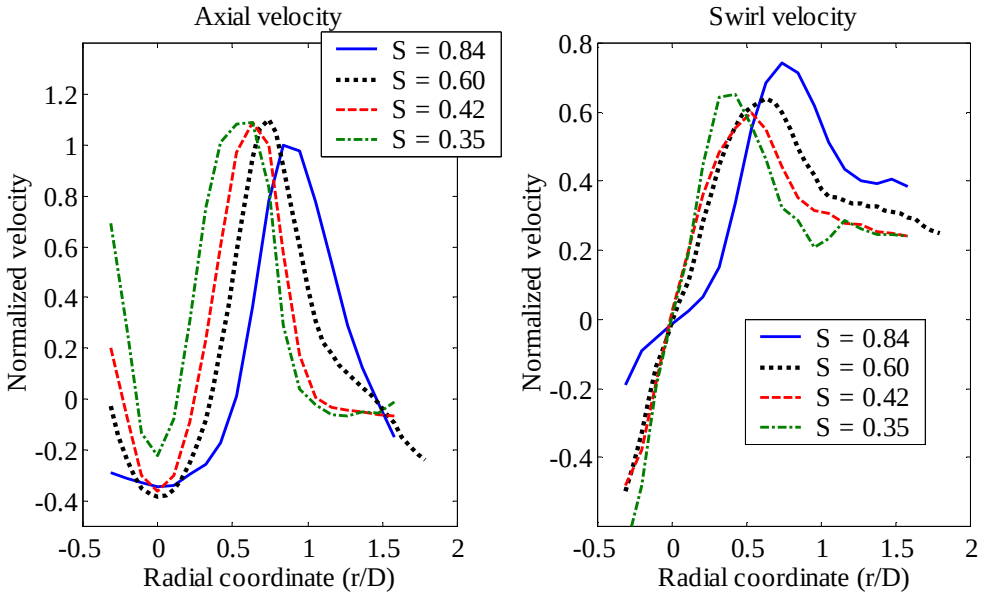

Figure 5.65: Velocity profiles for several swirl numbers at x/D_h=0.68, Q=50 SCFM

Figure 5.66 underline the difference between the distribution of swirl and axial velocity oscillation magnitudes. At r/D_h=0.5, the axial velocity oscillation magnitude is near its maximum whereas the swirl velocity oscillation magnitude is near its innermost node. The time history shows a vigorous oscillation with significant recirculation in the low part of the cycle. The swirl velocity on the other hand appears relatively quiet and exhibits no sign of coherent oscillation. The picture obtained from the time histories is reinforced by the histograms shown in Figure 5.67. The axial velocity histogram shows a very wide distribution with two smeared peaks. The bi-modal distribution is clear evidence of periodic motion. The swirl velocity histogram on the other hand is near gaussian.

The converse of the conditions in Figures 5.66 and 5.67 is shown in Figures 5.68 and 5.69, which shows time histories and histograms for the same conditions except at r/D_h=0.02, near the centerline of the flow. The point here is chosen near an axial velocity fluctuation node and a swirl velocity fluctuation maximum. The time history now appears more random for the axial velocity component and distinctively periodic for the swirl velocity component. The histograms are less easily distinguished. The

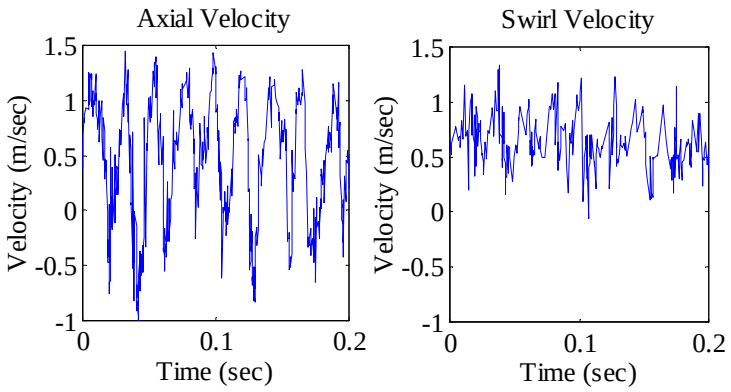

Figure 5.66: Time histories of axial and swirl velocity at r/D_h=0.50, x/D_h=0.68, S=0.6, Q=50 SCFM

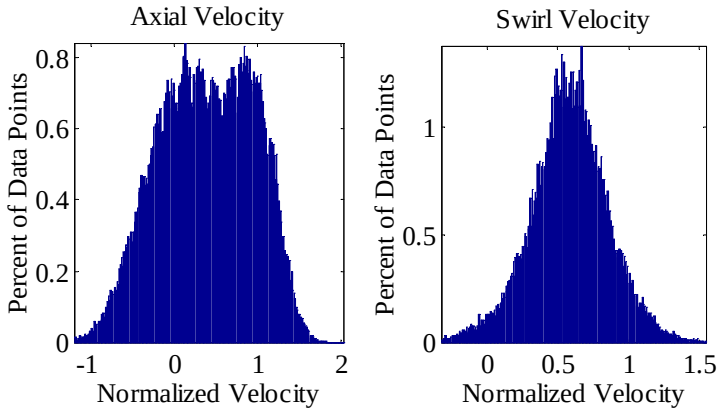

Figure 5.67: Histograms of axial and swirl velocity at r/D_h=0.50, x/D_h=0.68, S=0.6, Q=50 SCFM

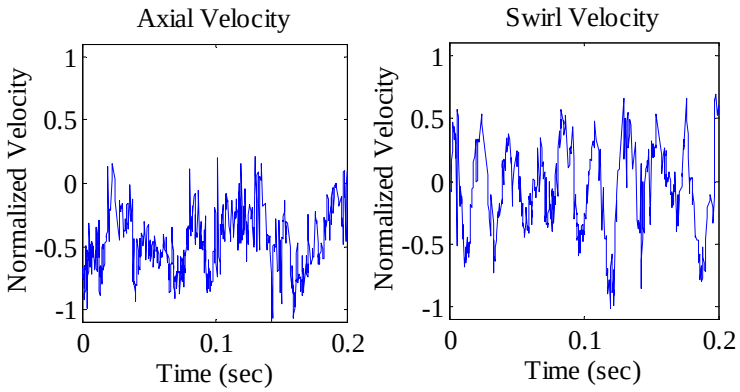

Figure 5.68: Time history of velocity at r/D_h=0.02, x/D_h=0.68, S=0.6, Q=50 SCFM

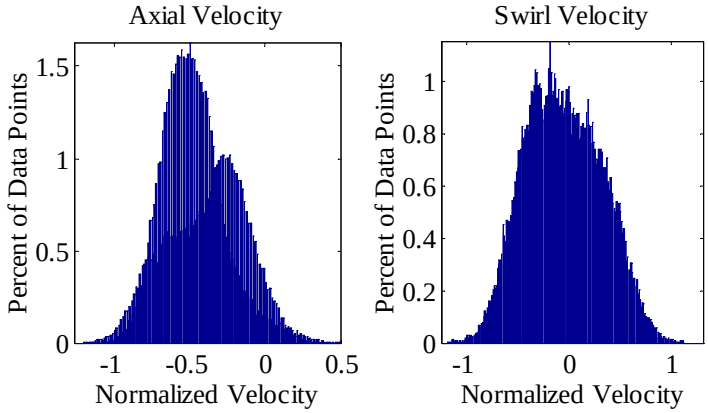

Figure 5.69: Histograms of axial and swirl velocity at r/D_h=0.02, x/D_h=0.68, S=0.6, Q=50 SCFM

swirl velocity histogram does not appear bi-modal although it does appear much wider than in Figure 5.67. The axial velocity distribution is narrower but still exhibits evidence of other than random dynamics with a secondary peak in the histogram.

The high degree of similarity seen in the instability structure under variation of swirl and the smooth linear variation of frequency with flow rate all support the diagnosis that the oscillations observed are due to a flow instability that is self-excited. The gain provided by acoustic feedback is too sensitive a function of frequency to allow the instability frequency to vary linearly with flow rate over the wide range

reported here. There is the possibility that the oscillations represent the response of a very narrow band lightly damped resonance to broad band turbulence input. Such resonances have indeed been found for separated flows. Cooper and Crighton (2000) showed that jet instabilities can be modeled as damped absolute resonances. The resonance then relies on the existence of a damped global mode. In determining absolute stability in Chapter 6, the existence of global modes will be determined.

5.3.3 Annulus geometry dynamics at lower swirl numbers

As swirl is decreased the neatly organized instability discussed in Section 5.3.2 is replaced by a very complex dynamic picture. The discussion will center around the S=0.30 case of the annulus geometry. The velocity profiles for this case at 50 SCFM are shown for the first three measured axial stations in Figure 5.70. The velocity profiles at 100 SCFM are very similar and will not be repeated here (see Section 4.3). The plot shows the relatively rapid consumption of azimuthal momentum in the swirl velocity profiles accompanied by a wake type axial velocity profile that recovers and widens downstream.

Figure 5.71 shows the un-normalized power spectra at several radial locations mostly in the inner shear layer (wake). The outermost radial location is just outside the wake portion of the axial velocity profile. The spectra clearly show how much more fluctuation energy is contained in the wake portion of the flow field. The broadband peak mentioned above in Section 5.2.2 is most visible in the swirl velocity fluctuations but also appears in the axial velocity fluctuations, at radial locations away from the center of the flow field.

Figure 5.72 and 5.73 show a radial comparison of power spectra at x/D_h=1.47 at S=0.30. Figure 5.72 shows the results for 50 SCFM and Figure 5.73 shows the results for 100 SCFM. The wake at this axial location has broadened but still exhibits the same mean axial velocity minimum as x/D_h=0.68. The radial locations at which the spectra are shown again correspond to locations in the inner shear layer. The outermost radial location is very near the outer edge of the wake. The results for the two flow rates are very similar. The downward shift in frequency of the spectral

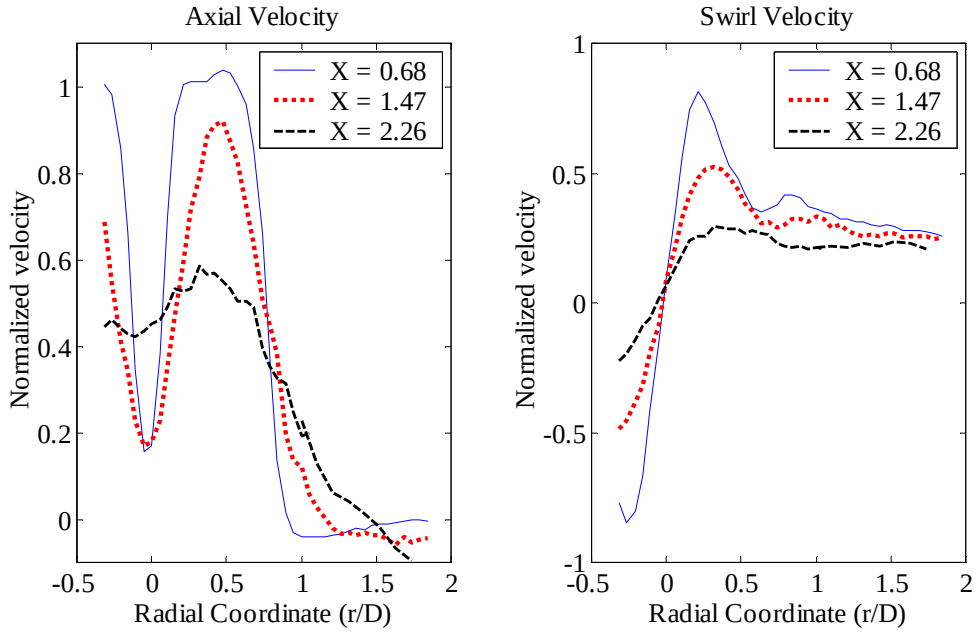

Figure 5.70: Mean velocity profiles in combustor for S=0.29, Q=50 SCFM

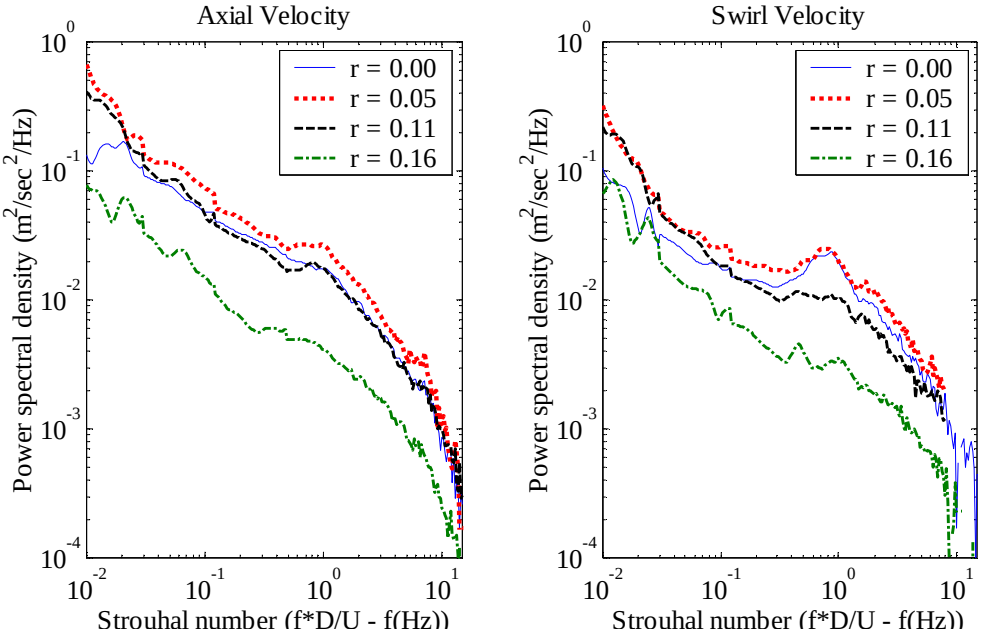

Figure 5.71: Radial comparison of power spectra inside inner shear layer at x/D_h=0.68, S=0.29, Q=50 SCFM

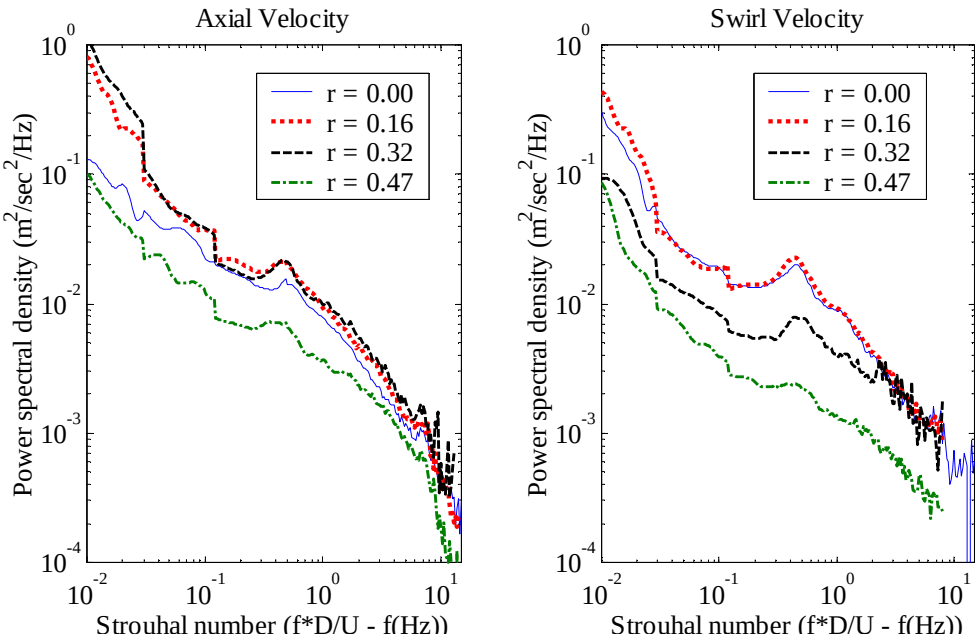

Figure 5.72: Radial comparison of power spectra inside inner shear layer at x/D_h=1.47, S=0.29, Q=50 SCFM

peak is observed for both flow rates and the peak is visible in both swirl and axial velocity fluctuations. The strength of the fluctuations decreases towards the edge of the wake where the spectral peak is barely visible. The visibility of the peak in the axial velocity fluctuations is better for the higher flow rate.

Figure 5.74 and 5.75 show a radial comparison of power spectra at x/D_h=2.26 at S=0.30. Figure 5.74 shows the results for 50 SCFM and Figure 5.75 shows the results for 100 SCFM. Both figures show that the broadband spectral peak has increased significantly in width and again shifted lower in frequency, although the shift here is less than the downward shift between x/D_h=0.68 and x/D_h=1.47. The development of the spectral energy is consistent with the view introduced above in Section 5.2.2, based on convective instability considerations. Relatively high frequency amplification occurs initially in the flow. Only the lower frequency portion of the energy is further amplified downstream. Amplification rates decrease in the downstream direction resulting in a relatively smeared spectral picture. In Section 5.3.1, the spectral peak was seen to attain its peak magnitude at the last axial station measured. The

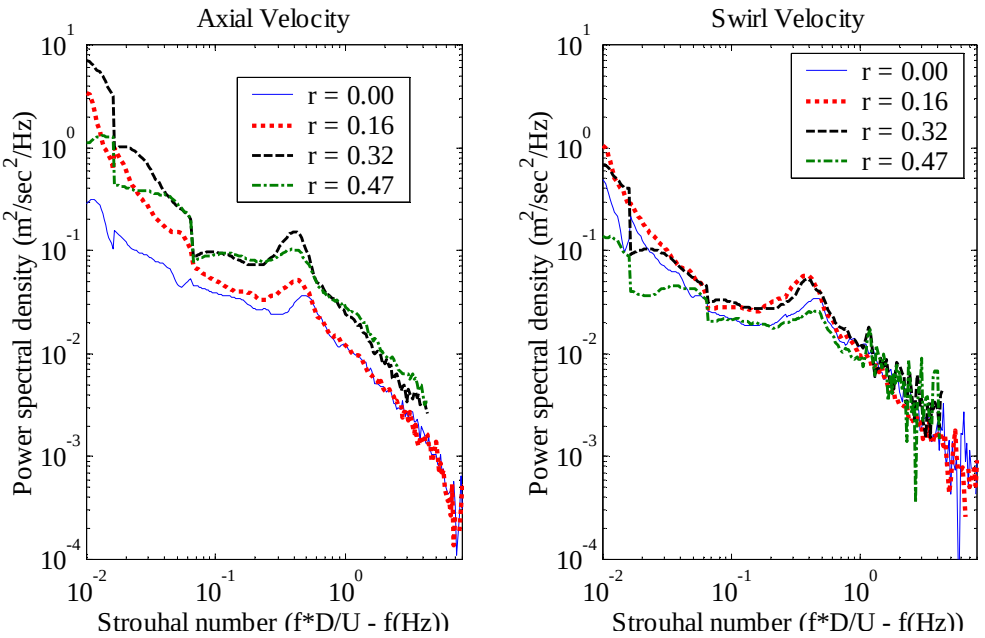

Figure 5.73: Radial comparison of power spectra inside inner shear layer at x/D_h=1.47, S=0.30, Q=100 SCFM

reason for this is the very slow development of the flow field. The speed of development here is above that of the jet and as a consequence the spectral peak reaches its highest visibility relatively early in the flow and becomes smeared downstream. Also consistent with this picture is the power spectrum observed for the S=0 case in the annulus geometry (Section 5.2.2). In this case, the flow develops extremely quickly and no spectral energy concentrations are visible at any axial location.

The other feature of the S=0.30 flow field worthy of more detailed discussion is the structure of the low frequency energy observed in the flow field. Figures 5.76 and 5.77 show time histories of the velocity near the outer edge of the inner shear layer. Neither the time scale nor the velocity scale have been normalized for these plots. The figures show that there is a repeatable pattern for both flow rates. The pattern period is about 0.75 sec for 100 SCFM and about 2 sec for 50 SCFM. The frequency thus does not exactly scale with flow rate. The periodicity is observed in both axial and swirl velocities. The pattern itself however differs greatly between axial and swirl velocity. At the start of the pattern, the axial velocity decreases

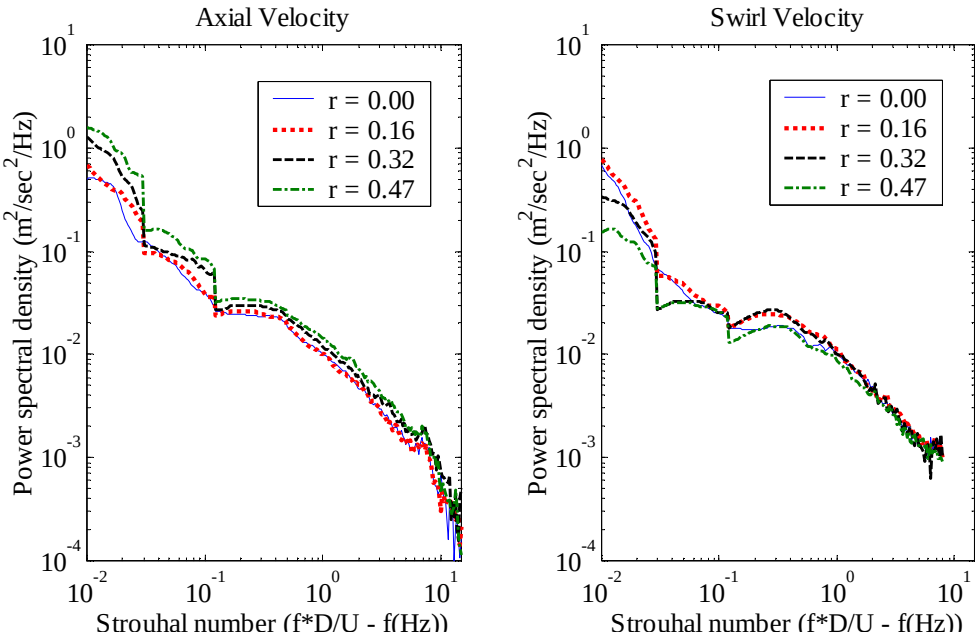

Figure 5.74: Radial comparison of power spectra inside inner shear layer at x/D_h=2.26, S=0.29, Q=50 SCFM

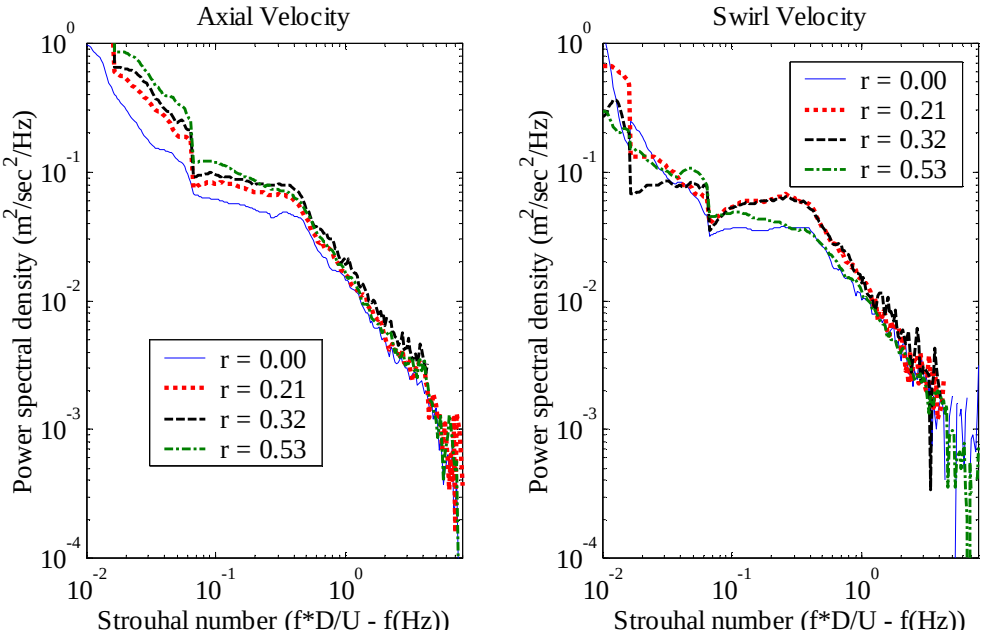

Figure 5.75: Radial comparison of power spectra inside inner shear layer at x/D_h=2.26, S=0.30, Q=100 SCFM

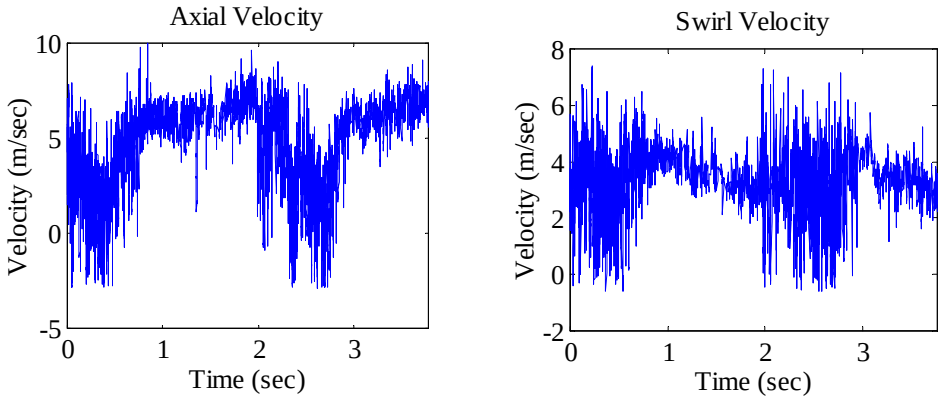

Figure 5.76: Intermittence at x/D_h=1.47, r/D_h=0.34, S=0.29, Q=50 SCFM

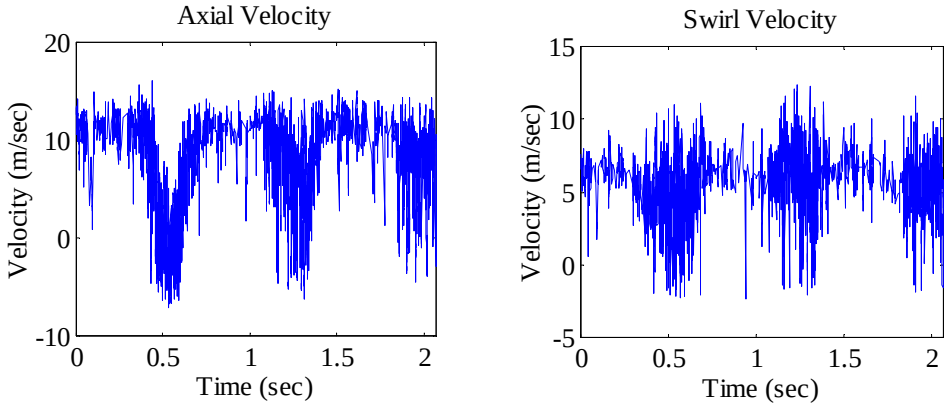

Figure 5.77: Intermittence at x/D_h=1.47, r/D_h=0.34, S=0.29, Q=100 SCFM

sharply to negative velocities, indicating reverse flow. At the same time, the swirl velocity begins to exhibit large oscillations about zero. After a time relatively short compared to the period of the intermittence, axial velocity increases again sharply and the swirl velocity ceases to exhibit large magnitude oscillations.

Figure 5.78 shows the structure of the intermittence in the middle of the low velocity portion of the intermittence for r/D_h=0.42 and x/D_h=1.47 (100 SCFM). Very large sinusoidal oscillations can be clearly identified, especially in the axial velocity. The frequency of these oscillations corresponds to the spectral peak observed in the power spectra at around St=0.4. In between the low velocity portions of the cycle, the

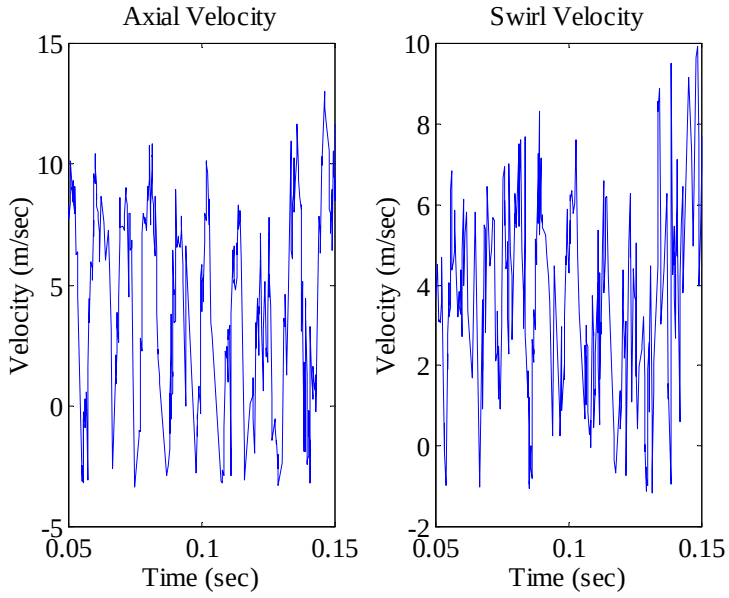

Figure 5.78: Intermittence at x/D_h=1.47, r/D_h=0.42, S=0.30, Q=100 SCFM

data rate of the LDV is slowed considerably, but these coherent oscillations cannot be distinguished in the high velocity portion of the intermittence. The high coherence of oscillations observed in Figure 5.78 is not typical. At other radial locations the sample time histories show only limited evidence of the coherent sinusoidal oscillations.

The form of the intermittence is a sensitive function of the radial location. Figure 5.79 shows sample time histories of velocity for the 50 SCFM flow rate at r/D_h=0.16, x/D_h=1.47. Figure 5.80 shows sample time histories of velocity for the 100 SCFM flow rate at r/D_h=0.68, x/D_h=1.47. The intermittence in these figures looks nearly sinusoidal with periods still matching those seen above. It is interesting to note that for Figure 5.80, the swirl velocity does not exhibit any signs of intermittence.

The various time histories of velocity shown above can be attributed to periodic radial movement of the flow exiting from the nozzle. The movement is such that the actual flow structure stays intact. The radial movement of the flow causes a point measurement of velocity to exhibit the intermittence observed above. For points near the edge of the wake (Figures 5.76 and 5.77), the velocity will appear near constant as

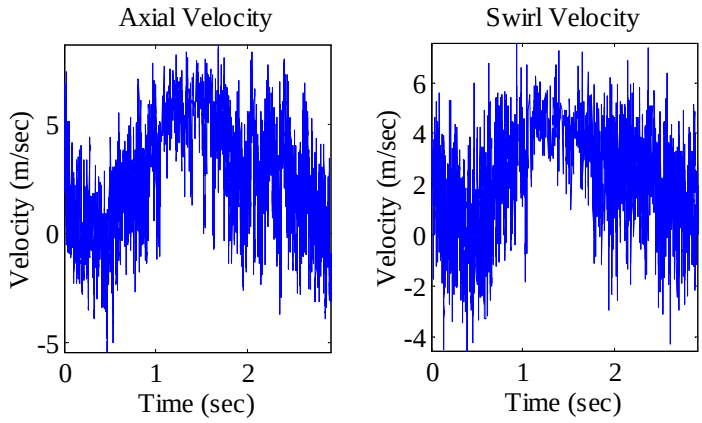

Figure 5.79: Intermittence at x/D_h=1.47, r/D_h=0.16, S=0.29, Q=50 SCFM

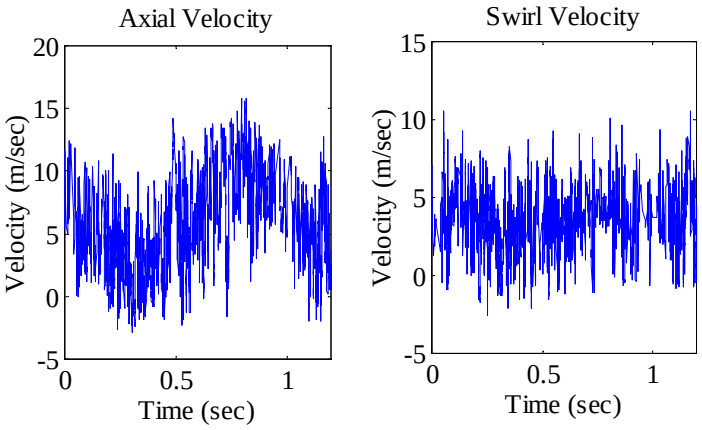

Figure 5.80: Intermittence at x/D_h=1.47, r/D_h=0.68, S=0.30, Q=100 SCFM

the flow moves radially inward because the mean velocity profile is flat in this region. As the flow moves radially outward however, the velocity decreases rapidly, causing a dip in the time history of axial velocity. The swirl velocity associated with the wake part of the flow is much more turbulent and hence the swirl velocity exhibits high amplitude fluctuations when the axial velocity has dipped down.

Also consistent with this picture is the fact that the sinusoidal velocity oscillations are observed in the wake portion of the jet movement cycle. The sinusoidal velocity fluctuations are associated with the inner shear layer instability and are especially visible in the wake. Away from the edge of the shear layer, the pattern becomes more sinusoidal as the mean velocity profile becomes more linear. The r/D_h=0.68 point is located in the middle of the outer shear layer and therefore exhibits nearly sinusoidal oscillations in axial velocity. The swirl velocity time history shows no clear evidence of jet movement since the mean velocity here is nearly flat. The point r/D_h=0.16 is located in the middle of the inner shear layer and therefore also exhibits nearly sinusoidal oscillation. At r/D_h=0.16, oscillation is also observed in the swirl velocity time history because the point is located in the middle of the vortex core of the mean swirl velocity profile.

Figure 5.79 shows the time histories of velocity for r/D_h=0.16, x/D_h=0.68 at 50 SCFM. The point is chosen near the edge of the inner shear layer, similar to location r/D_h=0.34 at x/D_h=1.48. Once more, intermittence can be observed in the flow field. However, the magnitude of the intermittence is much lower than observed further downstream. The lower magnitude of the intermittence is noteworthy especially in view of the fact that the velocity profiles are steeper at x/D_h=0.68 than x/D_h=1.48. For the same amount of movement, a larger intermittence would be expected at x/D_h=0.68. The fact that the intermittence is weaker at x/D_h=0.68 points to the fact that the jet movement decreases upstream. A likely anchor point for the jet movement is the dump location into the downstream section where the flow leaves the center–body.

Intermittence is also observed downstream of x/D_h=1.48, but the magnitude and coherence of the patterns decreases significantly. The motion of the jet is less notice-

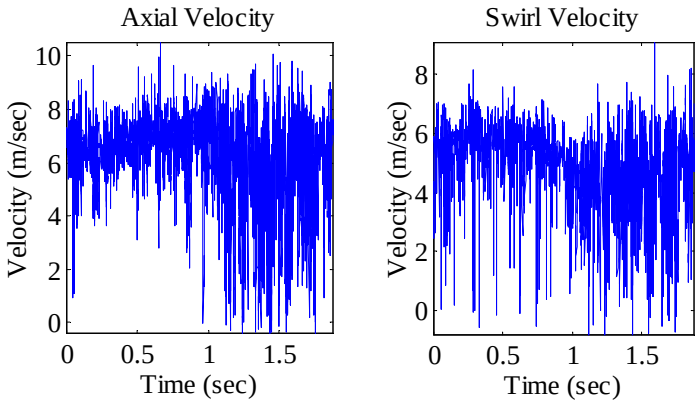

Figure 5.81: Intermittence at x/D_h=0.68, r/D_h=0.16, S=0.29, Q=50 SCFM

able downstream due to the decreased velocity gradients in the flow field. Clearly, the jet movement plays a pivotal role in the rapid mixing required to cause the velocity gradients to decrease so quickly. In Section 5.2.2 it was noted that the S=0.30 case flow field recovers more quickly than the S=0.60 velocity field. The cause of the accelerated flow development is the very efficient mixing executed by the movement of jet exiting into the dump. Jet movement is apparently more efficient at achieving large scale mixing than the large instability observed in the flow field at S=0.60.

Low frequency energy has also been noted under many other conditions flow conditions, but the large amplitude observed in the present flow field is unique to the intermediate swirl strength condition. Figure 5.82 shows the time histories of velocity in the inner shear layer at the same radial location as Figure 5.79 (r/D_h=0.16) but for the zero swirl condition. No trace of periodic intermittence can be observed, although the turbulent fluctuations are very high.

The cause of the movement described above is difficult to analyze. The role of swirl in the flow field cannot be understated however. In order to help point in the direction of the cause of the movement, Figure 5.83 shows the velocity profiles for four swirl levels at x/D_h=0.68, Q=50 SCFM. The dependence of the minimum mean axial velocity on the swirl level is of particular interest. Only the S=0.35 case exhibits clear flow reversal at the centerline. The next lowest velocity is obtained for S=0, the case without swirl. For this case the annular jet develops into an ordinary

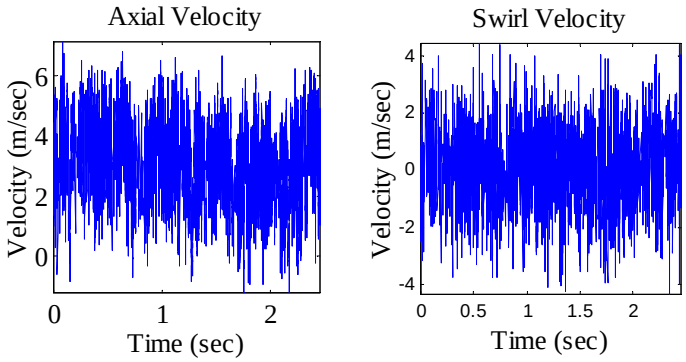

Figure 5.82: Lack of intermittence for x/D_h=0.68, r/D_h=0.16, S=0, Q=50 SCFM

jet at the last measurement location (x/D_h=4.79) as the wake profile in the center recovers quickly and axial momentum is lost slowly to the outside region of the flow. The next lowest mean axial velocity at the centerline is obtained from the S=0.30 case. Finally, the S=0.18 case only exhibits a very small wake at x/D_h=0.68. (The apparent asymmetry near the centerline is caused by the straight line connection between relatively coarsely spaced data points, not by actual asymmetry in the data)

The expected behavior would have been a smooth increase of the velocity at the centerline with decreasing swirl level. The fact that the wake appears to diminish in strength and then increase in strength as the swirl number decreases indicates that two competing elements are at work in shaping the flow development. The first element is the bluff body. The second element is swirl. Swirl is generally thought to expand the recirculation zone behind bluff bodies. However, this is a simplistic view. Swirl not only affects the pressure distribution in the flow but also is an excellent mixer through the turbulence produced by the shear that always exists in a flow with swirl.

The trend observed in Figure 5.83 can be explained in terms of the two influences of swirl on the flow field: turbulence production and pressure distribution. As swirl is increased from zero, the changes observed in the flow field are largely due to the increased turbulence production obtained through the addition of swirl. As swirl is increased further, turbulence production increases but the pressure distribution induced

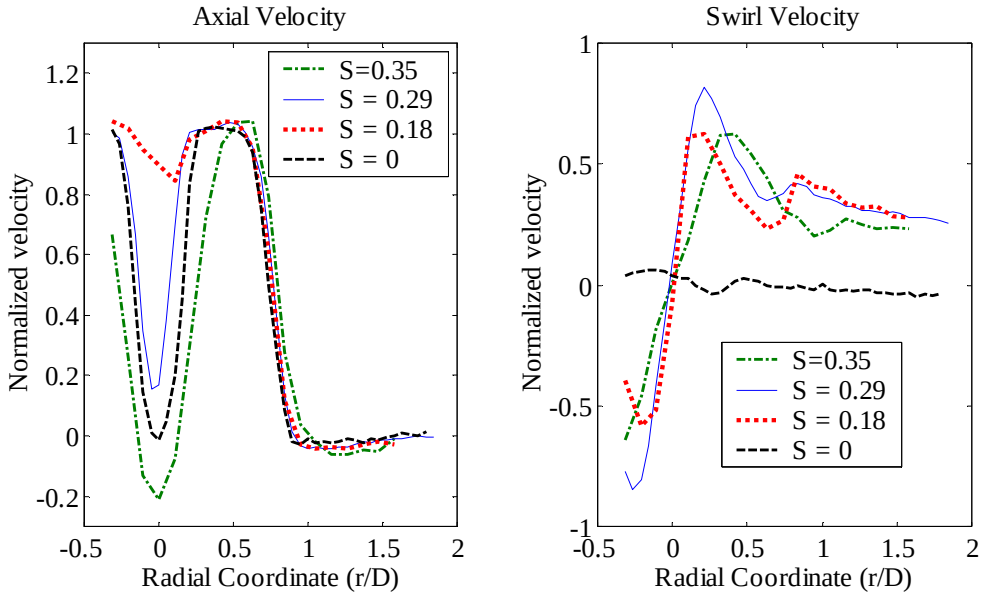

Figure 5.83: Mean velocity profiles at x/D_h=0.68 for low swirl numbers with flow rate of Q=50 SCFM

by swirl is not significant enough to affect the flow field. The radial distribution of pressure induced by swirl is negligible relative to axial pressure gradient experienced by the flow. As swirl is increased further, the radial pressure distribution induced by the swirling velocity field begins to affect the flow field and eventually dominates the effect on the flow field. The radial momentum equation under the assumption of zero radial velocity supports the initial insignificance of pressure effects and their eventual dominance. The radial momentum equation under the specified assumption reduces to a relationship that states that the local radial pressure gradient is proportional to the local swirl velocity squared. This non-linear relationship between swirl velocity and pressure gradient is consistent with the explanation of flow behavior as swirl is increased.

In terms of Figure 5.83, the bluff body wake is initially erased more quickly by the addition of swirl because the increased turbulence enhances mixing and therefore redistributes momentum more rapidly (S=0.18). As swirl is increased further, the radial pressure distribution begins to be important in flow development and the bluff body wake expands and extends further downstream. However, turbulence production

remains high because the vortex core remains relatively small with high shear and only expands slowly downstream. A further increase in swirl causes the flow field to be dominated by the effect of the radial pressure gradient induced by swirl and a wide central recirculation region develops. The flow diverges radially outward on entering the downstream section and is slow to recover as turbulence production has slowed significantly due to the large expansion of the vortex core and associated reduction in shear.

The movement of the jet seen for the S=0.29 case could thus be interpreted as the result of a flow field trying to react to two processes at the same time. A motion cycle could be described as follows. The flow enters with a tight vortex core and the efficient turbulence production causes rapid mixing of axial and azimuthal momentum. The dissipation of azimuthal momentum is rapid enough to generate a significant adverse pressure gradient on the centerline. The flow reverses on the centerline, expanding the vortex core upstream and deflecting the incoming jet radially outward. The now expanded vortex core does not produce enough turbulence to produce the mixing required to continue the rapid dissipation of azimuthal momentum. The adverse pressure gradient on the centerline is reduced and the flow field eventually reforms at its starting point, beginning a new cycle.

The process described in the above paragraph is at this point a very poorly supported argument but it is difficult to determine what specific types of experiments may lead to further clarification. It is clear that the data presented is very interesting from a flow control and mixing optimization point of view. For example, in the future, it may be possible to mechanically enhance the jet movement with little control effort and further increase mixing.

Finally, the mechanism for jet movement described is global to the flow field and linear stability analysis cannot be expected to help validate the mechanism.

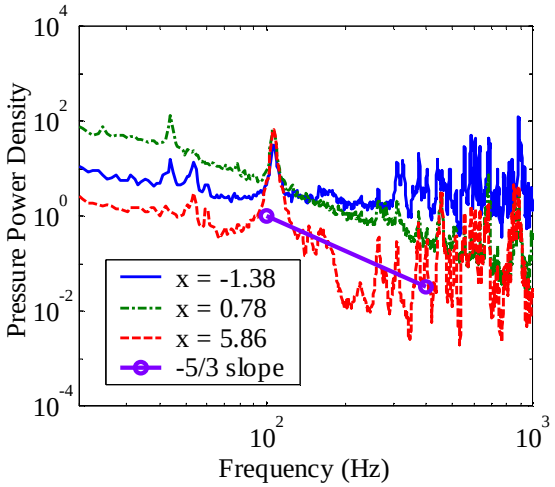

Figure 5.84: Noise spectra at various axial locations for S=0.6 and Q=50 SCFM

5.4 Acoustics and flow dynamics

The problem with discussing pressure measurements in a highly turbulent flow such as that studied here is the separation of propagating acoustic noise and local hydrodynamic noise. For the more complicated environment of an operating gas turbine combustor, Strahle et al. (1977) attempted to separate flow noise, entropy wave induced noise and direct combustion noise. Multiple point simultaneous measurements in the combustor near the flame, near the combustor exit and beyond the exit were able to shed some light on the relative importance of the contributions.

A more qualitative way to distinguish hydrodynamic noise from acoustic noise is in looking at the frequency content of the noise. Figure 5.84 shows the power spectra of pressures measured at various axial locations. The nozzle pressure spectrum lies significantly above that in the downstream section of the combustor. This is expected based on an approximate balance of acoustic energy between the nozzle and the combustor section. The area reduction causes the pressure levels inside the nozzle to be higher than those in the combustor. The microphone located relatively close to the sudden (x/D_n=0.25) expansion exhibits entirely different behavior. The spectrum strongly resembles that found in the velocity spectra outside the outer shear layer.

A -5/3 slope is indicated on the figure to help make the point that the noise measured in this area of the flow field is closely related to the velocity fluctuations. The seemingly unorganized oscillations in energy observed in the nozzle and the downstream location are due to the influence of acoustic modes which occur regularly with increasing frequency. The signature of these acoustic modes is much weaker for the location just beyond the dump. The weaker signature of the acoustic pressure at this location is surprising considering the measurement location is relatively near the area expansion which acoustically will look like a pressure antinode. One of the possible reasons the acoustic peaks are suppressed in this area may be the distortion of the acoustic field caused by the presence of a highly sheared flow.

The strongest peak in the spectrum is observed near the dominant acoustic mode of the downstream combustor section, around 106 Hz. The wavelength for this mode is 3.14 m. The combustor test section length is 0.8 m long, meaning that the mode can be associated with the quarter wavelength of the combustor test section. To support this claim, Figure 5.85 shows a plot of the operating deflection shapes at four frequencies in the combustor. The operating deflection shapes were generated by exciting the combustor with white noise output from a small speaker mounted in a threaded hole at the top of the combustor. The shape at 100 Hz clearly indicates a near quarter wavelength distribution. The reason the amplitude of this mode is lower here than for example the pressure at 200 Hz has to do with the location of driving which is suboptimal for the 100 Hz mode and near optimal for the 200 Hz mode.

The other feature seen in Figure 5.84 are the peaks located around 45 and 52 Hz. The 52 Hz peak is only observed in the nozzle and downstream section indicating that this energy is likely acoustic in nature. The 45 Hz peak is strongest at the location just beyond the sudden expansion. It is also visible in the nozzle section. The 45 Hz peak matches the frequency of the instability observed in this flow field exactly and therefore is likely due to hydrodynamic noise generated by the instability.

Section 5.3.2 hypothesized that because the swirl RMS velocity is non-zero at the centerline, the mode of instability must have a nonzero azimuthal wavenumber. Furthermore, higher azimuthal modes also require that oscillations go to zero at

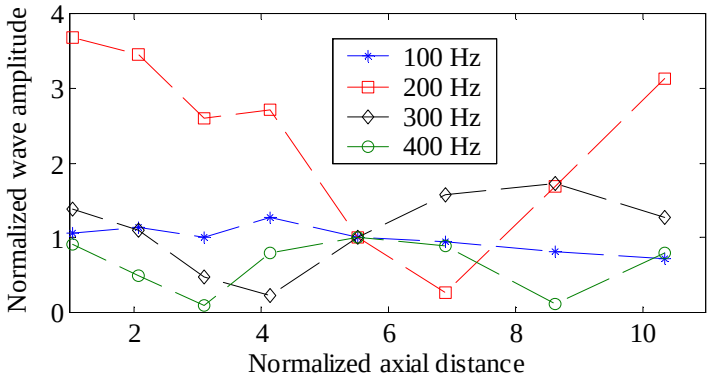

Figure 5.85: Operating deflection shapes of combustor pressures at four frequencies

the centerline (see Section 6.2). The only possibility is that the mode is associated with the first azimuthal mode. The problem that remains is to determine the sense of propagation of the instability with respect to the predominant swirl direction. Propagation in the opposite direction of swirl indicates an azimuthal wavenumber of -1. Propagation with the direction of swirl indicates an azimuthal wavenumber of 1.

Without simultaneous two point measurements, and without the ability to phase lock azimuthal instabilities to a form of excitation the direction of propagation is difficult to identify. However, the hydrodynamic noise generated by the instability can be used to help in the identification. Two of the eight microphones used in the limited acoustic measurements performed were located near the sudden expansion, spaced at 90 degrees around the perimeter. Figure 5.86 shows the coherence and transfer function phase between the two microphones. The coherence between the two microphones at the frequency of instability is 0.7, which is relatively high considering the energy at this peak is caused by velocity fluctuations. The phase between the two microphones is difficult to identify but at the instability frequency, the phase is clearly positive. The positive phase means that the velocity oscillation is moving with the direction of the mean swirl and thus indicates that the instability has azimuthal wavenumber 1. This finding is consistent with the study of Michalke (1999) which finds that ring jet type velocity profiles with reverse flow on the centerline are absolutely unstable with azimuthal wavenumber equal to +1. The absolute stabil-

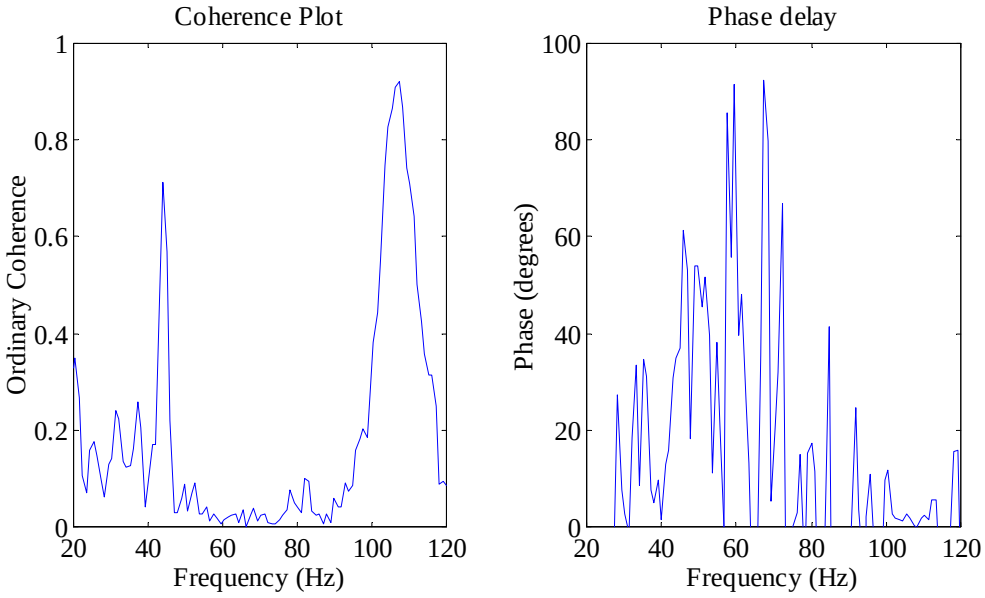

Figure 5.86: Coherence and phase between two circumferentially spaced microphones for S=0.6, Q=50 SCFM

ity characteristics of the flow fields measured here are examined in Section 6.7 of Chapter 6.

In order to investigate whether or not the instability is an acoustic source in the flow field, the power contained in the pressure fluctuations around 106 Hz($\pm$ 6 Hz) is plotted against flow rate. The resulting plot is shown in Figure 5.87. The plot shows that the pressure oscillation power is a rapidly increasing function of flow rate. At the last flow rate, the instability frequency overlaps with the quarter wave mode of the combustor. However, no increase in power is seen above that expected for the increase in flow rate. The inability of the instability to force the 106 Hz mode must not be attributed to the instability characteristics alone. Clearly the fact that the instability is azimuthal makes it a relatively inefficient driver. However, nearly as important is that the 106 Hz mode has a pressure antinode near the instability so that acoustic velocities are close to zero (at least in the outer parts of the flow field) and the acoustic mode is not able to be driven efficiently.

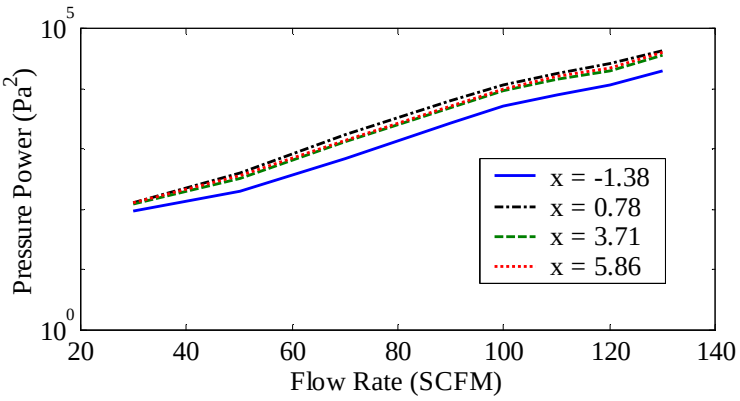

Figure 5.87: Pressure oscillation power around 100 Hz as a function of flow rate